UNIVERSITY OF CALIFORNIA

Los Angeles

Measurements of the Jet Cross Section and Spin Asymmetry A_{LL} using Polarized Proton Beams at RHIC

A dissertation submitted in partial satisfaction

of the requirements for the degree

Doctor of Philosophy in Physics

by

David Douglas Staszak

2010

UMI Number: 3501955

The dissertation of David Douglas Staszak is approved.
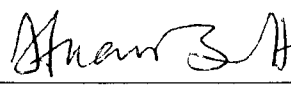
_____
Huan Huang
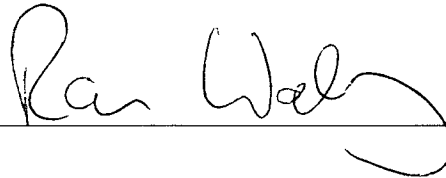
_____
Rainer Wallny
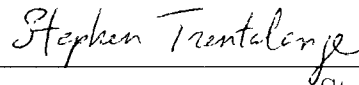
_____
Stephen Trentalange

_____
Gang Li
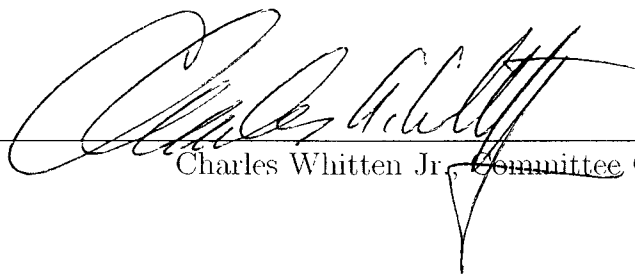
_____
Charles Whitten Jr., Committee Chair

University of California, Los Angeles

2010

TABLE OF CONTENTS

LIST OF FIGURES

LIST OF TABLES

Acknowledgments

There are many, many people who helped me along the way with this dissertation. First and foremost, I thank Kendall. In no uncertain words, it was her patience, sacrifice, and support that made this dissertation possible. We're going on that vacation now. I also thank Stephen Trentalange. Besides teaching me the ins and outs of experimental science, I can honestly say that some of the moments I've felt the most confident in my chosen path with physics and science were spent on his office couch discussing some phenomena in Nature. I also could not have asked for a better environment to conduct my research than the group Profs. Whitten and Huang provided. They supported me with open office doors and directed guidance that made my graduate career smooth and my research relevant. Working with Prof. Igo in the cold basement of Knudsen was a formative experience, and not because of the weird un-used dolphin cage built into the floor. This was my first true immersion into nuclear physics experimentation, and I am indebted to him for taking the time to work with me.

Outside of UCLA, I'd like to thank the Renee Fatemi. She was a selfless colleague, and, whether she knows it or not, I'm convinced she's the reason it didn't take me 2 years to first reconstruct jets. I also thank Ernst Sichtermann for supporting me from the Spin convener helm. Last, but certainly not least, I thank my parents. My dad for inspiring in me a sense of wonder about the world. I still vividly remember tinkering with an oscilloscope he brought home from work, trying to wrap my young head around *sin* waves and electricity. And my mom, for ingraining in me from the beginning that I could do anything I set my mind to. We would all be amazed by the depth and passion of the letter of recommendation she'd write for me.

VITA

1 June 1980	Born, Arlington Heights, Illinios, USA.
May 2003	BA, Physics, *Magna cum laude* University of Colorado, Boulder
2004	Development Technician UCSB High Energy Physics Group
2004 - 2005	Teaching Assistant UCLA Department of Physics and Astronomy
2004 - 2005	GAANN Fellowship UCLA Department of Physics and Astronomy
2005, 2006	Outstanding TA Award UCLA Department of Physics and Astronomy
Dec. 2005	MA, Physics University of California, Los Angeles
2005 - present	Graduate Research Assistant Intermediate Energy Physics and Relativistic Heavy Ion Group University of California, Los Angeles

PUBLICATIONS AND PRESENTATIONS

David Staszak. Measurements of Polarized Glue at STAR. *RHIC and AGS*

Users' Meeting, Brookhaven National Laboratory, June 2009

David Staszak, for the STAR Collaboration Recent Longitudinal Spin Asymmetry Measurements for Inclusive Jet Production at STAR *PANIC 2008 Proceedings, Nuclear Physics A special issue* 9-14, Nov 2008, Eilat, Israel

David Staszak, for the STAR Collaboration Inclusive Jet A_{LL} Measurements at STAR *Proceedings of Lake Louise Winter Institute* Alberta, Canada, 18-23, Feb 2008

David Staszak Double Longitudinal Spin Asymmetry Measurement for Inclusive Jet Production at STAR *APS Meeting* Jacksonville, Florida, April, 2007

M Dima, et al Mass Determination Method for Selectron+-(L,R) Above Production Threshold *Phys Rev* D65 071701, 2002

M Battaglia, et al Run Scenarios for the Linear Collider *Proceedings of the APS/PDF/PDB Summer Study on the Future of Particle Physics*, E3006 Snowmass, Colorado, 2001

ABSTRACT OF THE DISSERTATION

Measurements of the Jet Cross Section and Spin Asymmetry A_{LL} using Polarized Proton Beams at RHIC

by

David Douglas Staszak

Doctor of Philosophy in Physics

University of California, Los Angeles, 2010

Professor Charles Whitten Jr., Chair

The nature of the proton spin structure is a fundamental problem in nuclear physics. The proton, which possesses a spin quantum number $1/2\hbar$, is a complex bounded system containing valence quarks, gluons, and sea quarks. One can ask how the spin of the proton decomposes into partonic spin and orbital angular momentum degrees of freedom. The EMC collaboration performed the first detailed measurement of the proton spin structure in 1988. They found that quarks contribute only $14 \pm 10\%$ of the total spin, far below naive parton model predictions. No valid theoretical pictures could explain such a low fraction of spin carried by the quarks and the proton 'spin crisis' was born.

The deficit must arise from gluon spin and quark/gluon orbital angular momentum contributions. However, until the Relativistic Heavy Ion Collider (RHIC) these contributions were not directly accessible. RHIC currently provides collisions of polarized proton beams at center of mass energies of 62, 200, and 500 GeV. A primary objective of the RHIC physics program is the determination of the gluon spin contribution, ΔG. At leading order in proton-proton collisions, we

have access to quark/quark, quark/gluon, and gluon/gluon interactions. Utilizing proton collisions of different helicity states, ΔG is accessible through measurements of the double spin asymmetry A_{LL}, where A_{LL} is defined as the ratio of the polarized cross section divided by the unpolarized cross section. The polarized cross section is the difference in the measured cross sections with both proton helicity states aligned and with both anti-aligned. The unpolarized cross section is the sum of these.

The data presented in this dissertation were collected in 2006 at the STAR detector. It represents an integrated luminosity of 5.6 pb^{-1} with typical beam polarizations of $\sim 55\%$. We use a time projection chamber (TPC) and an electromagnetic calorimeter (BEMC) to reconstruct jets from the charged and neutral particles emitted from hard collisions. Before we measure the spin asymmetry, we confirm the applicability of NLO theoretical calculations at our experimental energies and kinematics by comparing our measured inclusive jet cross section to theory. The agreement between the measurement and theoretical calculations is good. We then compare our measurements of A_{LL} as a function of jet transverse momentum (p_T) with theoretical predictions based on various models of the underlying proton spin structure. The results are found to rule out large positive and negative gluon contributions within STAR's kinematic range ($x \approx 0.05 \leftrightarrow 0.2$). Small positive and negative gluon contributions are still allowed, as are models that predict a zero crossing.

CHAPTER 1

Introduction and Motivation for the

Measurement

In 1922 Otto Stern and Walther Gerlach directed a beam of neutral silver atoms through an inhomogeneous magnetic field The result was the first direct evidence of quantized particle spin A classical (pre-quantum mechanical) picture predicts an even spread of beam deflection about the beam axis Instead, they found that the beam was deflected up or down depending on the quantized spin state (up or down) of the outermost unpaired electron

Since its discovery, intrinsic particle spin has played a fundamental role within science On the one hand, spin is the most tangible of purely quantum mechanical phenomena in everyday life Electron spin behavior determines the chemical properties of atoms Nuclear Magnetic Resonance (NMR) imaging, which utilizes spin procession about a magnetic field, directly affects the health of millions At the same time, though, it is also one of the most non-intuitive and unexplainable phenomena All known particle species possess spin as a quantum number that is an integer or half-integer multiple of a single fundamental constant of Nature, Planck's constant ($\hbar$) It is a challenge to attach a proper physical picture to a particle such as a photon, which has no mass and fills no physical space yet still contains a measurable spin angular momentum Despite 80 years of the study of spin phenomena, the physical origin of spin remains a mystery

1

In classical mechanics an object spinning about a fixed external axis can possess two types of angular momentum: orbital angular momentum, from the revolution about the center of the system, and spin angular momentum, from rotations about the object's own center. The system's total angular momentum is the sum of the two. An analogous explanation fits in quantum mechanics (QM), with the caveat that both forms of angular momentum are now quantized.

For a particle that is not 'fundamental', such as an atom, the total angular momentum must then be the sum of the spin and orbital components of all the constituents (i.e. nuclei and electrons). The orbital angular momentum states of the constituents can take on many different (quantized) values arising from perturbations to the system. On the other hand, the spin angular momentum states of the constituents are set depending on only the particle species (fermions with half-integer spins - electrons, quarks, protons, or bosons with integer spins - photons, gluons). In this sense, composite particles are described as having a definitive spin state but not a definitive total angular momentum state. To avoid this confusion composite particles are often referred to as spin-X particles where X is the total angular momentum state (this is the case with the spin-1/2 proton as will be described later).

1.1   A Historical Picture of Proton Structure

By the late 1960s, experiments were built to provide particle collisions with enough energy to probe the proton's sub-structure. In these experiments the proton was probed using Deep Inelastic Scattering (DIS), in which a lepton (usually an electron or muon) is scattered off a proton. It was soon realized that protons were not fundamental particles and that the proton's sub-structure displayed 'scaling behavior'. The sub-structure interacted invariantly with respect

to the Q^2 of the collision, where Q^2 is defined as the four-vector momentum transfer of the collision, the momentum 'scale' of the collision. Higher energy (and therefore higher-Q^2) collisions probe smaller distance scales within the proton. At all energy scales the proton constituents interacted like a point-source.

The parton model was invented to explain this scaling behavior. This substructure was identified with point-like particles called partons and later associated with Gell-Mann's fractionally charged 'quarks'. The parton model pictures the proton as consisting of three valence quarks: two up quarks (u) with charge +2/3e (where e is the charge of the electron) and spin $1/2\hbar$, and one down quark (d) with charge -1/3e and spin $1/2\hbar$. In a relativistic proton the quarks are collinear and each carry a fraction of the total proton momentum x.

Leptons in DIS interact with quarks electromagnetically, exchanging a virtual photon. Experimentalists measure the initial and final momenta of the lepton to piece together the collision dynamics. The proton structure is summarized by two structure functions, which are related for spin-1/2 particles.

$$F_1(x, Q^2) = \frac{1}{2} \sum_j e_j^2 [q_j(x, Q^2) + \bar{q}_j(x, Q^2)] \tag{1.1}$$

$$F_2(x, Q^2) = 2x F_1(x, Q^2) \tag{1.2}$$

Here $q(x)$ and $\bar{q}(x)$ are the number densities (parton distribution functions or PDFs) of the constituent quarks and anti-quarks, e_j is the charge of the quark, and j indicates the quark flavor. Decades of DIS experiments have yielded precisely known structure functions $F_{1,2}$ over a wide x and Q^2 range (Fig. 1.1, left)[1].

We now know that the proton is more complicated than the simple parton
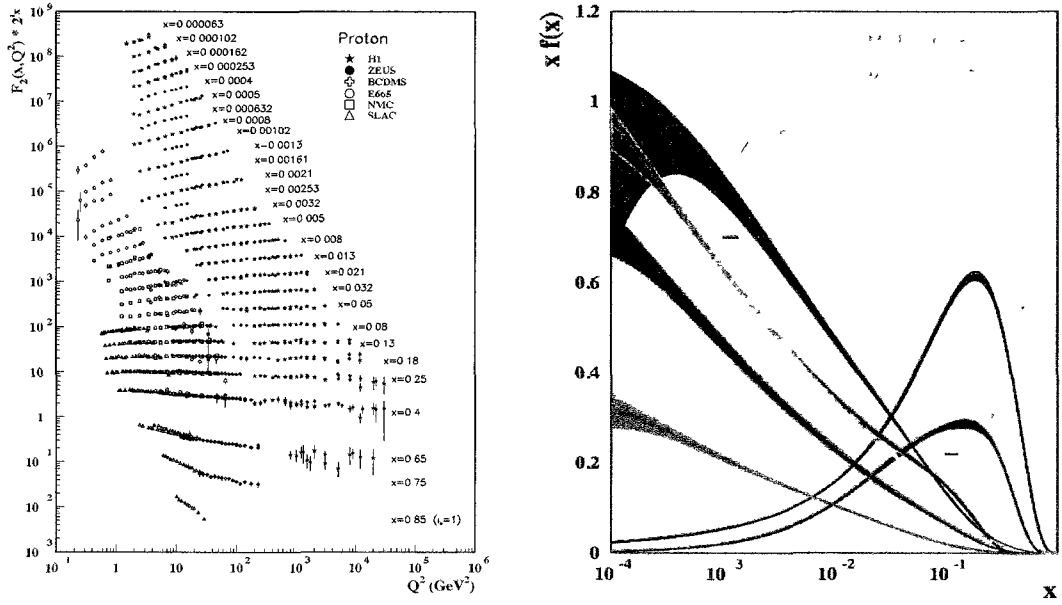
Figure 1.1: $F_2(x, Q^2)$ as a function of Q^2 for many x bins (left). For plot clarity $F_2(x, Q^2)$ is multiplied by a factor 2^{i_x}, where i_x is the number of the x bin. Quark and gluon PDFs as a function of x calculated by the MSTW2008 theory group(right). The PDFs are displayed for $Q^2 = \mu^2 = 10$ GeV^2. Note that $u_v(d_v)$ represents the up(down) valence quark PDF and that the gluon PDF has been divided by 10. Both figures represent the accumulated knowledge from decades of DIS and SIDIS experiments.

model posits. The parton model requires modifications that arise from a full Quantum Chromo Dynamics (QCD) description. QCD is the theory of strong interactions with gluon and quark fields as the fundamental fields. What emerges with the QCD-modified parton model is a proton that is a complex object, with valence quarks, gluons (no charge, spin $\hbar$), and quark/anti-quark sea quark pairs popping in and out of existence from the QCD vacuum. The naive parton model predicts $F_2(x, Q^2)$ in Fig. 1.1 to be invariant with Q^2. However, we see that

this invariance is only approximate. QCD interactions including gluons and sea quarks must be accounted for (see Fig. 1.2).
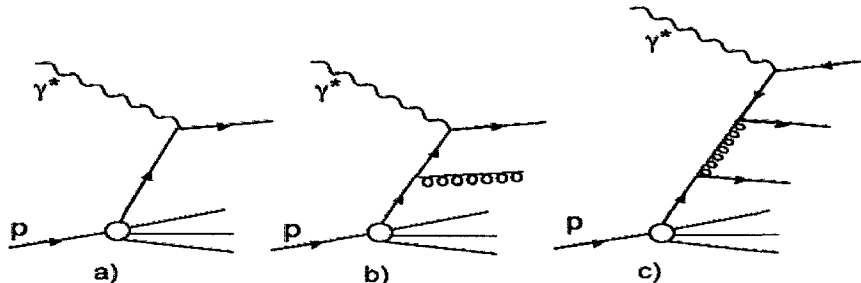
Figure 1.2: a) Interaction of a virtual photon with a quark in DIS. b,c) Two examples of higher order diagrams with quark-gluon interactions.

With gluon and sea quark interactions included, the evolution of the quark (flavor i) and gluon PDFs as a function of Q^2 (for a given x) can be found[2]:

$$\frac{dq^i(x, Q^2)}{dQ^2} = \frac{\alpha_s(Q^2)}{2\pi} \int_x^1 \frac{dy}{y} \left[q^i(y, Q^2) P_{qq}(x/y) + g(y, Q^2) P_{qg}(x/y) \right] \quad (1.3)$$

$$\frac{dg(x, Q^2)}{dQ^2} = \frac{\alpha_s(Q^2)}{2\pi} \int_x^1 \frac{dy}{y} \left[\sum_{i=1}^{flavor} q^i(y, Q^2) P_{gq}(x/y) + g(y, Q^2) P_{gg}(x/y) \right] \quad (1.4)$$

$P_{jk}(x/y)$ are the splitting functions and are calculable. $(\alpha_s(Q^2)/2\pi) \cdot P_{jk}(x/y)$ is interpreted as a probability density of measuring parton j (momentum x) after an interaction with parent parton k (momentum y). In this sense, Eq. 1.3 accounts for two changes to the number of quarks at a measured x: a quark may lose momentum by radiating a gluon or a gluon inside the proton may create a quark/anti-quark pair. Similarly, Eq. 1.4 accounts for the changes to the number of gluons at a measured x: a quark may radiate a gluon or a gluon may split into either a quark/anti-quark pair or two gluons.

Theorists can calculate the various splitting functions and perform fits to $F_{1,2}$ using Eqs. 1.3 and 1.4 in order to disentangle the PDFs. It is the indirect interaction with gluons that gives rise to the gentle logarithmic slopes in the $F_{1,2}$ distributions. Figure 1.1 (right) shows the modern unpolarized picture of the proton for a single snapshot in Q^2 (labeled μ^2 in the figure)[1]. Valence quarks are most likely to be found with higher momentum fraction x, while gluons and sea quarks become more important as lower x is probed.

1.2 The Proton Spin Puzzle

If the lepton beam is longitudinally polarized, we can probe the spin dependent structure functions using the analog of Eq. 1.1:

$$g_1(x, Q^2) = \frac{1}{2} \sum_j e_j^2 [\Delta q_j(x, Q^2) + \Delta \bar{q}_j(x, Q^2)] \qquad (1.5)$$

Here we are not probing the standard PDFs, but polarized PDFs:

$$\Delta q_j(x, Q^2) = q_j^+(x, Q^2) - q_j^-(x, Q^2) \qquad (1.6)$$

where $+(-)$ represent the parton helicity direction aligned(anti-aligned) with the proton helicity direction. In the non-relativistic case, the naive parton model predicts that the quarks carry all the proton spin. In the relativistic case, it predicts that the quarks carry $\sim 65\%$ of the the net proton spin and anticipates a large g_1. This structure function was first measured in 1988 by the EMC collaboration[3] using a polarized muon beam. They found that quarks(and anti-quarks) contribute only $14 \pm 3 \pm 10\%$ of the proton spin, which in the extreme case was consistent with zero. These results were significantly lower than the parton model predictions and in violation of the Ellis-Jaffe sum rule. This raised

questions about the origin of the the proton spin, and the spin 'crisis' of the parton model was born[4].
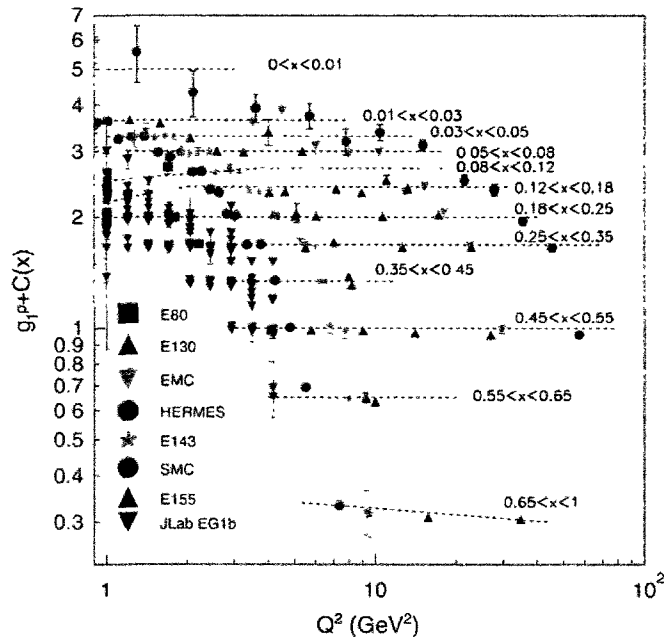
Figure 1.3: World data on $g_1(x, Q^2)$ as a function of Q^2 for several x intervals. A constant $C(x)$ is added to visually separate g_1 values for different x intervals.

As in the unpolarized case, theorists looked to a QCD description of the problem. In accounting for all interactions including a gluon, they found an additional Next-to-Leading Order (NLO) term that adds directly to g_1 (Eq. 1.5):

$$g_1^{gluon} \propto -\frac{\alpha_s(Q^2)}{2\pi} \Delta g(Q^2) \tag{1.7}$$

Here Δg is the polarized gluon PDF analogous to Δq above, and α_s is the strength of the coupling constant of the strong interaction (analogous to e in electromagnetic interactions). This term adds directly to Eq. 1.5 and implies that for a positive Δg, gluon and quark contributions cancel in the measurement of g_1.

There was no particular physical motivation for a large and positive Δg, but it seemed to elegantly explain the experimental findings. The previous estimate of a large quark spin contribution could be reconciled by a large gluon spin contribution. Putting these terms together (and simplifying g_1 to only the flavor singlet term), the first moment of g_1 now reads

$$g_1^{(1)} = \frac{1}{9} \int_0^1 dx (\Delta q(x) + \Delta \bar{q}(x)) - \frac{1}{3} \frac{\alpha_s(Q^2)}{2\pi} \int_0^1 dx \Delta g(x, Q^2) \qquad (1.8)$$

Figure 1.3 presents the current experimental state of g_1[5]. Since the first EMC results, g_1 and the quark contribution are both known much better. Recent analyses from HERMES[6] and COMPASS[7] find the first moment of g_1 to be $33.0 \pm 2.8\%$ and $33 \pm 5.8\%$, respectively. Global fits, using similar methods to those in the unpolarized case, have been performed with the polarized analogs of the evolution equations (Eqs. 1.3 and 1.4). Compared to the unpolarized case, however, the experimentally accessible x, Q^2 phase space is much smaller. As a result, the polarized PDFs are not as well constrained as the unpolarized case. Further, because gluons only contribute at NLO to Eq. 1.5, Δg is particularly unconstrained by DIS (Sec. 1.4 provides a full survey of polarized gluon models). Figure 1.4 presents polarized PDFs from the AAC collaboration using only DIS data[8] and compares to other models. There is general agreement between different fits on the shape and contributions from the up and down quark polarized PDFs. However, strange and gluon polarized PDFs are unconstrained.

In addition to the experimental challenge of decomposing the proton spin, there is a theoretical challenge. In the ideal case, a sum rule would exist for the proton spin that decomposes the total spin into gauge invariant (and experimentally measurable) contributions for each of the spin and angular momentum pieces. The nucleon angular momentum sum rule written in the infinite momen-
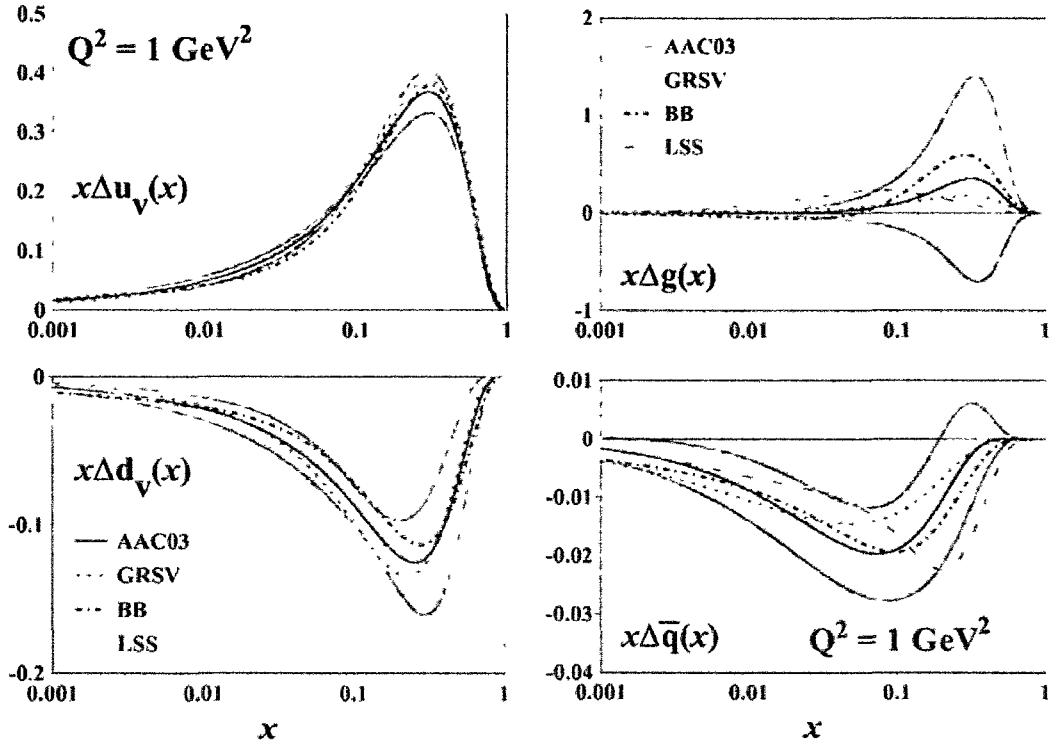
Figure 1.4: Polarized quark and gluon PDFs from the AAC collaboration evaluated at $Q^2 = 1.0$ GeV^2. Their predictions are compared to those from other theory groups at that time. Note the y-axis varies significantly between the figures. Green bands represent the uncertainty on model predictions in each figure.

tum frame (using $L_{q,g}$ to represent quark and gluon angular momentum terms) is:

$$\frac{1}{2} = \int_0^1 dx\{\frac{1}{2}\Delta q(x, Q^2) + \Delta g(x, Q^2) + L_q(x, Q^2) + L_g(x, Q^2)\} \qquad (1.9)$$

Here the quark and gluon spin terms are physical and represent measurable PDFs:

$$\Delta G(Q^2) = \int_0^1 \Delta g(x, Q^2) dx \ , \qquad \Delta \Sigma(Q^2) = \int_0^1 \Delta q(x, Q^2) dx \qquad (1.10)$$

Note there is an equivalent anti-quark term in the $\Delta \Sigma$ integral we have suppressed for simplicity. A problem arises with this decomposition as the orbital angular momentum terms both involve interactions with the gluon field[9]. This means these terms do not clearly represent a clean and independent physical description of the orbital angular momentum of quarks and gluons.

There is an additional decomposition that has been developed to separate out an experimentally measurable quark orbital angular momentum contribution[10].

$$\frac{1}{2} = \frac{1}{2} \Delta \Sigma + L_q + J_g \qquad (1.11)$$

Here J_g is a term that comprises the total gluon spin and orbital angular momentum and is not gauge invariant (and thus not physically meaningful). In this decomposition, only the quark spin term ($\Delta \Sigma$ from Eq. 1.10) is manifestly gauge invariant. In his paper, Ji[10] developed an experimental method to measure L_q via Deeply-Virtual Compton Scattering and a theoretical framework in which to predict L_q via lattice QCD. However, there is no connection between gluon spin measurements in Eq. 1.10 and quark orbital angular momentum measurements in Eq. 1.11. In fact the only physical connection between the two decompositions is the quark spin term, which is invariant in both.

1.3 RHIC: A Polarized QCD Environment

DIS experiments are fundamentally limited by the fact that the probe interacts electromagnetically with the proton. Such experiments are not directly sensi-

tive to the gluons because gluons possess no electric charge. The Relativistic Heavy Ion Collider (RHIC) is the next step in the evolution of polarized parton experiments[11]. For the first time *polarized* proton beams are brought into collision and gluon-gluon/quark-gluon interactions occur at leading order.

Theoretical calculations for RHIC proton-proton collisions are performed using a factorization scheme where the production cross section is written as a convolution of PDFs, fragmentation functions, and partonic sub-process cross sections. In this discussion we ignore the fragmentation functions because to first order jets are independent of fragmentation functions. The inclusive jet cross section (unpolarized) for $p + p \rightarrow jet + X$, where X is anything, is then written as:

$$\frac{d\sigma^{pp \rightarrow jet+X}}{d\mathcal{P}} = \sum_{f_1,f_2} \int dx_1 dx_2 f_1(x,\mu^2) f_2(x,\mu^2) \otimes \frac{d\hat{\sigma}^{f_1 f_2 \rightarrow f+X'}}{d\mathcal{P}}(x_1, p_1, x_2, p_2, \mu)$$

(1.12)

Here $p_{1,2}$ are the incoming proton momenta, $\mathcal{P}$ is used to represent the kinematic variables, $x_{1,2}$ are the momentum fractions carried by the interacting partons, and $f_{1,2}(x,\mu^2)$ are the respective PDFs of those partons. A factorization scale μ is introduced to remove infinities in the cross section calculations and is set at the nominal value $\mu^2 = Q^2$. The value of this scale is not physically motivated but is used simply to divide the cross section into a *short-timescale* portion, which is calculable (the partonic subprocess cross sections, $\hat{\sigma}$, above), and a *long-timescale* portion, which is not calculable (the PDFs). The predictive power of these calculations at RHIC rests on the universality of the PDFs. Proton PDFs (polarized or unpolarized) measured through any process (DIS, pp, etc...) are a universal characteristic of the proton. Information learned from DIS is transferrable to *pp* collisions and vice versa.

Inclusive jet cross section calculations have been performed for RHIC energies and kinematics to NLO precision[12]. Results from early data published by STAR[13] are shown in Fig. 1.5. The cross section is in agreement with NLO calculations within systematic uncertainty limits. One of the focuses of this thesis is to use our largest available proton-proton data set to re-examine with greater precision the comparison between our measured cross section and theory. Before spin measurements are made using jets, we must assure ourselves that the theoretical framework used to calculate spin observables is applicable in our kinematic range.

At leading order, proton-proton collisions give us access to a mixture of quark-quark, quark-gluon and gluon-gluon interactions. ΔG can be accessed through a double longitudinal asymmetry ratio, A_{LL}, which is formed from the ratio of the polarized cross section divided by the unpolarized cross section.

$$A_{LL} = \frac{\sum_{f_1, f_2} \Delta f_1 \times \Delta f_2 \times [d\hat{\sigma}^{f_1 f_2 \to fX'} \hat{a}_{LL}^{f_1 f_2 \to fX'}]}{\sum_{f_1 f_2} f_1 \times f_2 \times [d\hat{\sigma}^{f_1 f_2 \to fX'}]} \quad (1.13)$$

We have again used factorization to divide this ratio into incalculable universal functions ($f_{1,2}$, $\Delta f_{1,2}$) and a calculable partonic cross section ratio:

$$\hat{a}_{LL}^{f_1 f_2 \to fX'} = \frac{d\Delta\hat{\sigma}^{f_1 f_2 \to fX'}}{d\hat{\sigma}^{f_1 f_2 \to fX'}} \quad (1.14)$$

where $d\Delta\hat{\sigma}$ (the polarized partonic cross section) is defined through the difference of helicity-arranged partonic cross sections:

$$\frac{d\Delta\hat{\sigma}^{f_1 f_2 \to fX'}}{d\mathcal{P}} = \left\{ \frac{d\hat{\sigma}^{f_1^+ f_2^+ \to fX'}}{d\mathcal{P}} - \frac{d\hat{\sigma}^{f_1^+ f_2^- \to fX'}}{d\mathcal{P}} - \frac{d\hat{\sigma}^{f_1^- f_2^+ \to fX'}}{d\mathcal{P}} + \frac{d\hat{\sigma}^{f_1^- f_2^- \to fX'}}{d\mathcal{P}} \right\} \quad (1.15)$$
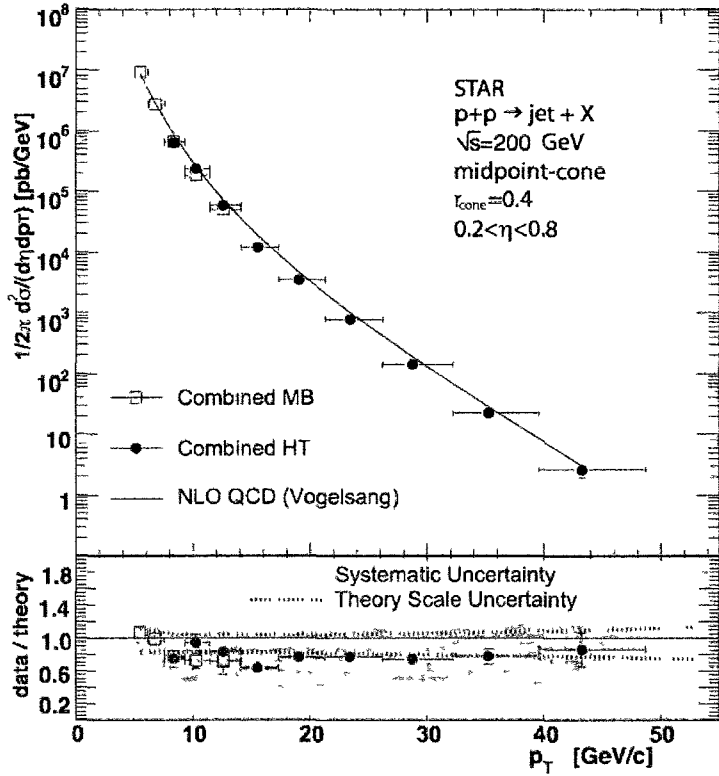
Figure 1.5: Top: Inclusive jet cross section as a function of jet p_T for 2003+2004 data using MB and HT triggers. Bottom: Data and theory comparison. The yellow band represents systematic uncertainty and the dotted lines represent theoretical uncertainties.

Fig. 1.6 (left) shows calculations of the partonic cross section ratio in Eq. 1.14 for various sub-processes[11]. In this figure θ is the center of mass scattering angle. The kinematically accessible window at STAR is centered at mid-rapidity (small $|\cos(\theta)|$), and here terms with both one and two gluons contribute. The right panel of Fig. 1.6 shows relative contributions of particular sub-processes divided by the total for both jets and pions. The results are the same if one scales the pion momentum (lower x-scale) by $\sim$1/2 of the jet momentum (upper
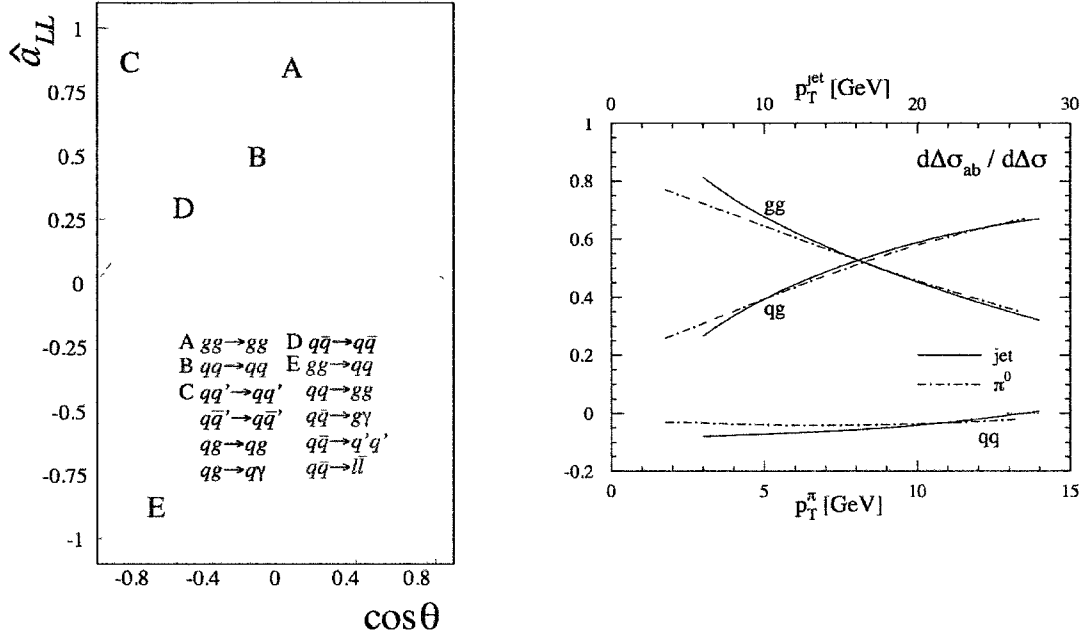
Figure 1.6: Left: Partonic subprocess as a function of center of mass angle $cos\Theta$ for the interactions of interest at RHIC. Right: Relative contributions of the various polarized subprocesses over the total polarized cross section as a function of jet p_T (top x-axis).

x-scale). At central rapidity, sub-processes involving an initial gluon predominate at jet momenta below ~ 30 GeV, which matches the experimentally accessible region of the STAR detectors.

1.4 Models of Polarized Gluon Structure

As discussed previously, $\Delta g(x, Q^2)$ is not well constrained by global DIS data. Δg is one area where RHIC, with polarized protons, is uniquely suited to contribute. Theoretical predictions of Δg vary wildly, and, in general the functional form and shape of Δg is not restricted by theory. Models of Δg are generated by assuming

14

some generalized parameterizations of the proton spin structure functions and fitting the available experimental results. Despite the fact that theory does not explicitly motivate a particular shape for Δg, a number of assumptions can be made. Assuming the parton PDFs are positive number densities, Eq. 1.6 implies a positivity constraint:

$$|\Delta g(x)| \leq g(x) \tag{1.16}$$

Further, as x approaches 0 or 1, physical intuition tells us that $\Delta g(x) \rightarrow 0$. There is little experimental insight into exactly how it approaches zero as $x \rightarrow 0$, but it has been argued[14] that $\Delta g(x)/g(x) \propto x^i$. The exponents are left as free parameters to be determined in the fit. At the other end of the spectrum, many groups assume that as $x \rightarrow 1$, $\Delta g(x) \propto (1-x)^j$. Again, exponents are left as free parameters. Previous experimental results do not constrain Δg enough to place a restriction on the sign or on the number of zero crossings. In fact, in the case of the LSS group[15], Δg with a positive, a negative, and a zero crossing yielded fits of equal quality.

In this study we consider many parameterizations of the polarized parton distributions. Fig. 1.7 (left) shows various models from the GRSV theory collaboration[16]. The models presented by GRSV arise from fits to available DIS data and show the breadth of proposed parameterizations. GRSV-MAX(MIN) are predictions based on the assumption that all the gluon helicities are aligned (anti-aligned) with the proton helicity at an initial scale $Q^2 = 4 \text{ GeV}^2/\text{c}^2$. GRSV-ZERO represents no net gluon polarization at the initial scale, and GRSV-STD is their best fit.

Fig. 1.7 (right) shows additional models from many theory groups. Most present parameterizations based solely on DIS data (including GS[17], LSS [15],
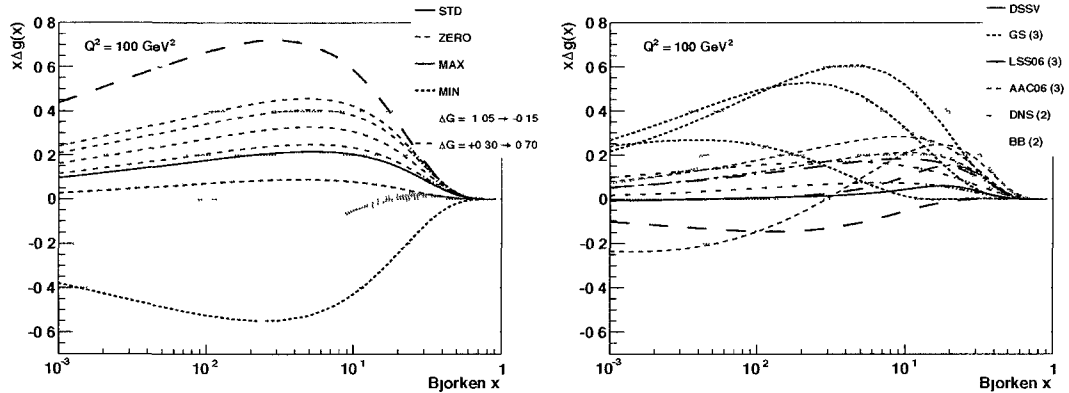
Figure 1.7: $x\Delta g(x)$ as a function of parton momentum fraction, x, is shown for the models considered in this study. Left: Various models presented by the GRSV collaboration, ranging from all the gluon helicities aligned with the proton helicity (MAX) to all the gluon helicities anti-aligned (MIN) at the initial scale $Q^2 = 4$ GeV^2/c^2. Right: Models proposed by other theory groups.

DNS[18], and BB[19]). Two more recent parameterizations consider information from first results at RHIC in addition to DIS data (DSSV[20] and AAC[21]). Including RHIC data in fits presents an added difficultly for theorists as compared to DIS data. We measure our observables as a function of transverse momentum (p_T), not simply x and Q^2. Mellin integral moments are needed to transform between p_T, which is an integral over both x and Q^2, and the evolution equations (Eqs. 1.3 and 1.4).

One parameterization we give particular attention to is the so-called Gehrmann-Stirling C model (GS-C). This model contains a zero crossing within our kinematically accessible range of x. In this situation, positive and negative gluon contributions to A_{LL} will cancel over our entire x-range. For this reason we are largely insensitive to models of this type. This can be clearly seen in Fig. 1.8. Here we show the functional form of two $\Delta g(x, Q^2)$ models over a wide range of

both x and Q^2. Overlaid is our experimental sensitivity for jets, where red represents a region of higher sensitivity and blue lower sensitivity. GS-C (right) has a significant polarization at lower x than we can experimentally measure. GSSV-STD (left), on the other hand, represents a model that contains a significant fraction of the total integral of the function within our window.
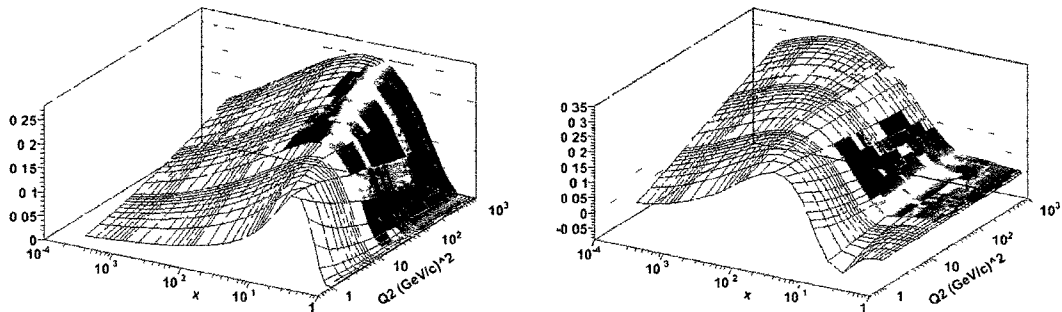
Figure 1.8: $\Delta g(x, Q^2)$ from two models, GRSV-STD (left) and GS-C (right), both presented as a function of x and Q^2. Overlaid is the sensitivity of inclusive jets within the STAR acceptance, with red regions indicating higher sensitivity and blue regions indicating lower sensitivity.

The work of GRSV is particularly important to this study because they developed an inclusive jet framework. This framework translates their polarized parton models into direct predictions of inclusive jet A_{LL}. They also publicly released their code, so we were able to use their inclusive jet predictions with the other polarized models as input. Fig. 1.9 shows A_{LL} predictions arising from the many polarized PDF predictions discussed above.
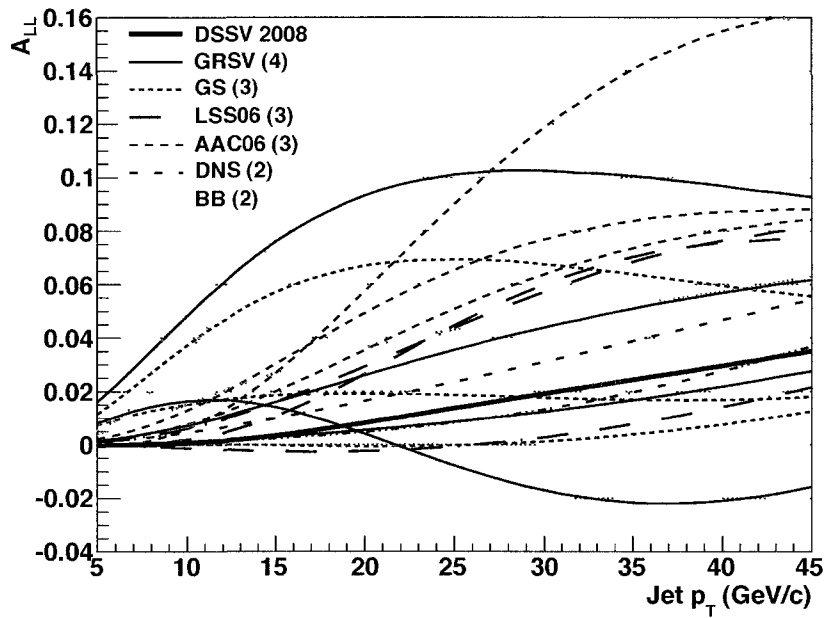
Figure 1 9   Inclusive jet A_{LL} as a function of p_T for the various polarized pa-
rameterizations considered in this thesis A family of curves arising from a single
theory collaboration is presented as a single color and line style

18

CHAPTER 2

RHIC and STAR Experimental Apparatus

The Relativistic Heavy Ion Collider (RHIC), located at Brookhaven National Laboratory (BNL), is unique among the world's particle physics laboratories as the first and only facility capable of colliding beams of *polarized* high energy protons. Beam physicists at BNL developed innovative technological advances in beam polarization control and in minimizing destructive depolarizing effects to make this possible. The studies presented within this volume are from data collected in 2006 during 6 months of RHIC running at $\sqrt{s} = 200$ GeV center of mass energy and $\sim 55\%$ beam polarization. The data were collected at the STAR experimental detector apparatus centered at one of several collision points around the RHIC ring.

2.1 RHIC Accelerator Complex

Many stages are required to transform ordinary Hydrogen atoms at room temperature and energy into highly energetic polarized proton beams circulating in RHIC near the speed of light[22]. Shown in Fig. 2.1 are the facilities at BNL used to create, transport, and accelerate the beams of protons.

An optically pumped polarized ion source (OPPIS) provides initial 300 μs pulses of up to 9 x 10^{11} polarized H^- ions with 80% polarization. Such high intensity and large polarization from the source are necessary because interme-
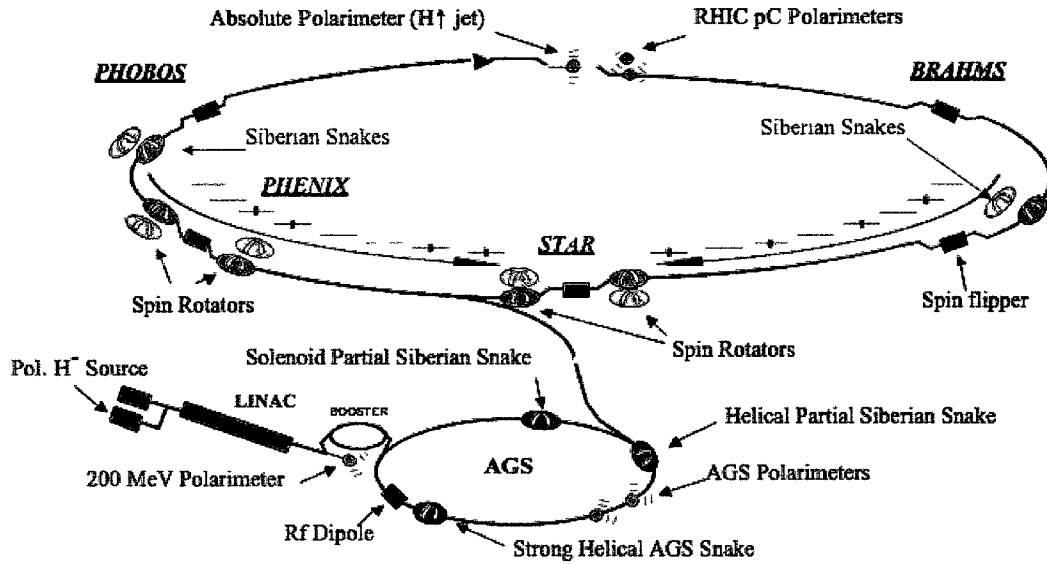
Figure 2.1: The RHIC accelerator complex is shown with a focus on components necessary for delivering and maintaining proton beam polarization.

diary stages before final collision energy in the RHIC ring cause losses to both. These H^- ions are focused and accelerated to 200 MeV using a radio frequency quadrupole magnet and a linear accelerator (LINAC). Before injection into the Booster synchrotron accelerator, the H^- ions are stripped of their electrons by passing the beam through a thin foil. The Booster collects each pulse of polarized protons into a single radio frequency (RF) time bucket and accelerates these collimated bunches to 1.5 GeV. The bunches are then transferred to the AGS and accelerated to 22.4 GeV, the energy at which they can be injected into the RHIC ring.

As of the 2009 RHIC run, proton-proton collisions with center of mass energies of 62, 200, and 500 GeV have been achieved in the ring. There are two counter circulating rings (labeled blue and yellow) and six collision points. STAR occupies the 6 o'clock position in an aerial view of the RHIC ring. At full capacity, each

RHIC ring can hold 120 proton bunches, each 2 ns in width with 106 ns spacing.

The stable spin direction for polarized protons circulating in RHIC and the AGS is aligned (or anti-aligned) with the vertical bending magnetic field. Many depolarization resonances are encountered during acceleration in the AGS and RHIC. Depolarization resonances occur when the spin procession frequency is in phase with a spin-perturbing magnetic field. Perturbing magnetic fields arise either from the intrinsic resonances of the magnet focusing fields or from imperfections in the magnets. To minimize these effects, Siberian snakes[23] are used. Two 180° snakes are employed at RHIC on opposing sides of the ring. Each Siberian snake is 2 m long and consists of a series of four superconducting helical dipole magnets capable of delivering a magnetic field of up to 4 Telsa. Siberian snakes utilize this field to control and rotate the spin direction of particles 180° about a horizontal axis. The pair of snakes then leaves the polarization direction of the beam unchanged for a complete circuit around the ring. However, the effect of perturbing fields on the beam has been changed and depolarizing effects cancel for a complete circuit. A slightly different setup is used in the AGS, where one weaker 9° snake is used in combination with a pulsed RF dipole.

Superconducting helical dipole magnets are also employed in RHIC as Spin Rotators. As shown in Fig. 2.1, these are placed on both the upstream and downstream sides of the major interaction regions for both beams. This allows rotation of vertical polarization to horizontal for collisions at STAR and PHENIX and then back to vertical after the interaction region. The bunches in the two rings are filled with different spin patterns, one with the double alternating spin directions and the other with single alternating spin directions. The combination of the bunch patterns and Spin Rotators allow us to take data for different longitudinal spin combinations every 106 ns. This virtually eliminates time dependent

biases in our spin measurements.

2.2 RHIC Polarimetry

Vertical polarization is measured through an asymmetry of scattered events left of vertical compared to right of vertical. P_{BEAM}, the polarization of the beam, is measured as:

$$P_{BEAM} = \frac{1}{A_P} \cdot \frac{N_L - N_R}{N_L + N_R} \tag{2.1}$$

where $N_{L,R}$ are production yields corresponding to left or right of vertical scattering, and A_P is the analyzing power of the scattering process. The polarization can only be measured in processes with a known analyzing power, which can come from either previous experimental results or theoretical calculations. RHIC has three devices dedicated to measuring the polarization of the proton beams.

Polarimeters at RHIC utilize both proton-proton and proton-Carbon elastic scattering in the Coulomb-Nuclear Interference (CNI) region[24][25]. One Hydrogen-jet target system sits at the the 12 o'clock interaction point and two proton-Carbon CNI polarimeters reside on the individual beams just up(down)stream of 12 o'clock. Theoretical calculations of the analyzing power in the relevant kinematic region for proton-proton and proton-Carbon processes have been made (see Fig. 2.2) and are found to be $\sim 3 - 5\%$. First measurements of these analyzing powers at RHIC[26][27] are now also published and agree with theory.

Relative beam polarization measurements are obtained multiple times during a fill using the pC CNI polarimeters. The pC CNI measurements can be made relatively fast and are the fill-by-fill polarization values used in our calculations. Hydrogen-jet measurements take much longer to measure but offer the
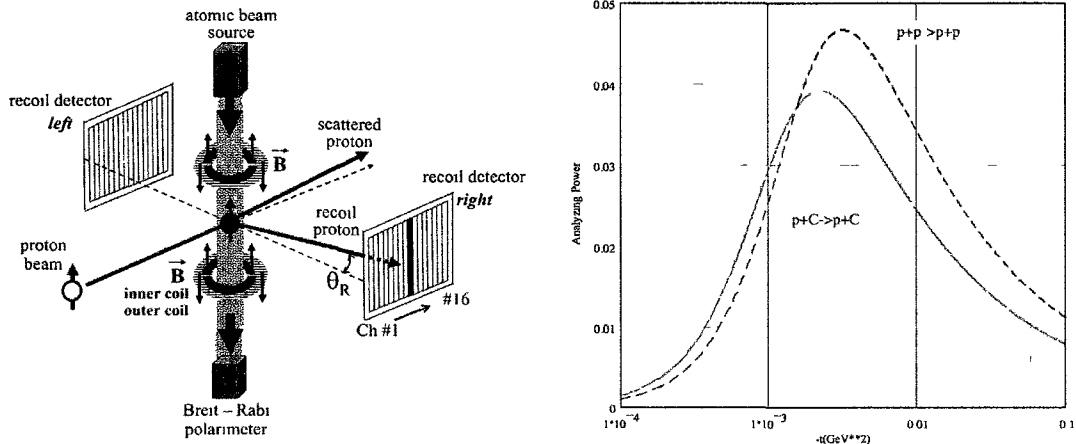
Figure 2.2: Left: Atomic hydrogen jet apparatus used for absolute beam polarization measurements. Right: Theoretically calculated analyzing power as a function of squared four momentum transfer for proton-proton and proton-Carbon scattering.

advantage of measuring asymmetries in two cases: 1) with a polarized target (at known polarization) and an unpolarized beam, and 2) with a polarized beam and an unpolarized target. This allows us to very reliably measure P_{BEAM} and when compared to proton-Carbon polarization measurements taken simultaneously normalizes the absolute scale of our fill-by-fill measurements.

The Hydrogen-jet target system (Fig. 2.2) consists of an atomic beam source, a scattering chamber, and a Breit-Rabi Polarimeter[28]. Highly polarized atomic hydrogen ($\sim 93\%$ polarized) collide with the beam and recoil protons are measured at $\sim 90^o$ to the left and right of the target using silicon detectors. Counts from these silicon detectors form the asymmetry in Eq. 2.1. The hydrogen jet is aligned to interact with one beam at a time. Due to limitations on the intensity of the atomic hydrogen beam, the statistical precision of the measurements for a single beam over the course of an entire fill was $\sim 8 - 20\%$. The Hydrogen-jet

23

statistics collected during 2006 allowed an overall proton-Carbon to hydrogen-jet normalization on the level of 1.5%[29].
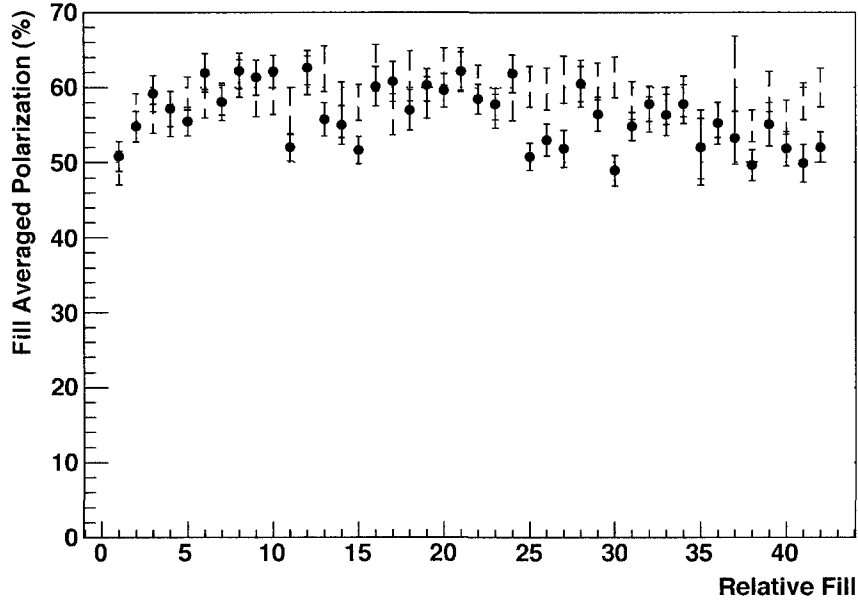
Figure 2.3: Fill averaged polarization values for both the yellow and blue beams from 2006 longitudinal data. We show only polarization values from fills used in this analysis.

To calculate the relative beam polarization, data taking at each of the experiments is stopped and an ultra-thin carbon ribbon target (3.5 $\mu g/cm^2$ thick[30]) is inserted into the proton beam for ~ 10 s at each of the pC CNI sites. Low energy recoil carbon nuclei are measured at $\sim 90^\circ$ to the left and right of the target using silicon detectors. These measurements are made at the beginning and end of every physics store in RHIC as well as approximately every 1.5 hours in between. Shown in Fig. 2.3 are the measured CNI polarizations (after normalization) for the blue and yellow beams during Run 6.

2.3 The STAR Detector

The STAR detector apparatus is one of four experiments housed around the RHIC ring. PHOBOS and BRAHMS, both smaller experimental facilities, have completed their physics programs and stopped taking data as of the 2007 RHIC Run. STAR and PHENIX are larger experiments that sit at the 6 and 8 o'clock positions of the RHIC ring. STAR is a large acceptance detector with the majority of its detector elements situated within a 0.5 Telsa solenoidal magnetic field. STAR contains high precision tracking and electromagnetic calorimetry covering the full 2π in azimuth. For these reasons, STAR is ideally designed for studies of jet production.
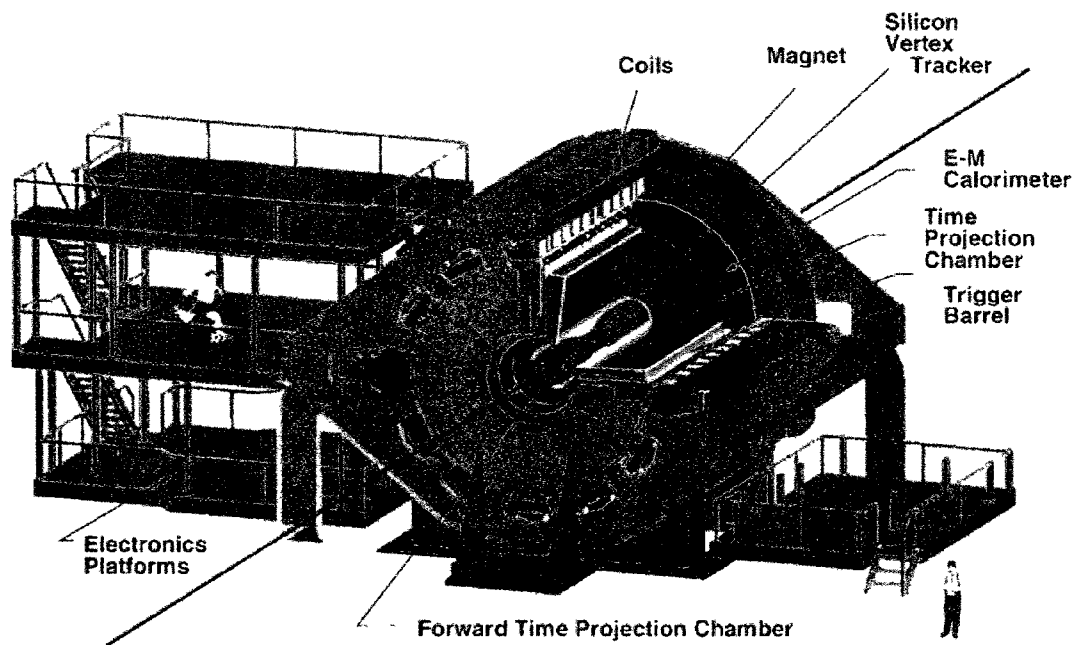
Figure 2.4: Schematic of the STAR detector apparatus. Shown here is a cutaway demonstrating how various layers of detector elements surround the interaction point.

2.3.1 Beam Beam Counters

STAR has two Beam-Beam Counters (BBCs)[31] sitting on the beamline 3.74 m to the east and the west of the nominal STAR IR. Each BBC consists of two arrays of 1 inch thick hexagonal scintillator tiles. As shown in Fig. 2.5, a large outer tile array spans a pseudorapidity range of $2.2 < |\eta| < 3.4$ and a small inner tile array spans a pseudorapidity range of $3.4 < |\eta| < 5.0$. High energy charged particles from a hard scattering traverse these plastic scintillator tiles losing energy from ionization processes. The plastic scintillator absorbs this energy and reemits it as a flash of scintillation light. These scintillation signals are then fed through four optical fibers embedded in each tile out to an individual photomultiplier tube residing outside of the magnet solenoid. Each BBC phototube measures a charge proportional to the energy deposited in the tile, and additionally, in the case of the smaller tiles, records a timing signal.

The small tiles provide the BBC functionality relevant to this study, including triggering, luminosity measurements, and polarimetry. Significant energy deposited in at least one small tile in both the east and west BBCs within a short timing window provides a baseline MinBias (MB) trigger at STAR. The rate of this coincidence trigger has been calibrated to monitor the overall beam luminosity and to measure the relative luminosity for different proton spin configurations. The BBC cross section[32] has been measured and found to be $\sigma_{BBC} = 26.1 \pm 0.2(stat.) \pm 1.8(syst.)$ mb. This is 53% of the total proton-proton cross section of $\sigma_{tot}^{pp} = 51$ mb and 87% of the inelastic, non-singly diffractive proton-proton cross section.

In addition to luminosity monitoring and triggering, the BBCs are also used at STAR as a local polarimeter[33]. For a vertically polarized beam the polarization is oriented either "up" ($\uparrow$) or "down" ($\downarrow$). To determine the polarization of one
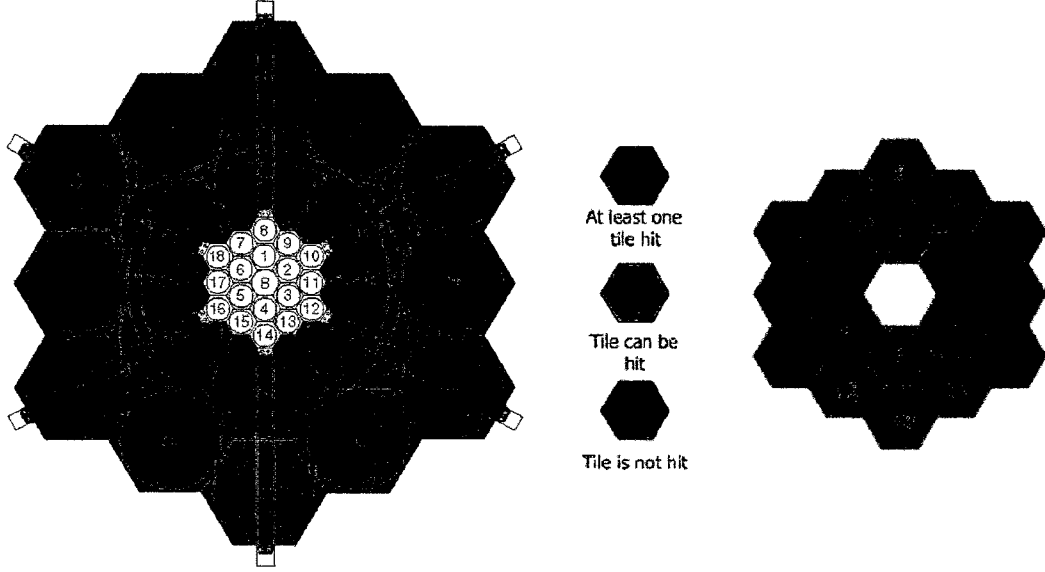
Figure 2.5: Shown left is the full construction of one of the two BBCs sitting 3.74 m east and west of the STAR IP. Shown right is a zoomed in figure of the small BBC tiles displaying definitions used to count a right scattering event. Red tiles must record a signal, dark green tiles must not record a signal, and no restrictions are made on light green tiles.

beam, we sum over the polarization states of the other beam, effectively making it an unpolarized target. The scattering of the first beam from the second will have a left-right asymmetry:

$$\epsilon_{BBC} = P_{BEAM}^{Vertical} \times A_N \simeq \frac{\sqrt{N_L^\uparrow N_R^\downarrow} - \sqrt{N_L^\downarrow N_R^\uparrow}}{\sqrt{N_L^\uparrow N_R^\downarrow} + \sqrt{N_L^\downarrow N_R^\uparrow}} \tag{2.2}$$

where $\uparrow$, $\downarrow$ refer to the beam bunch spin orientation and $N_{L,R}$ refers to left, right of vertical scattering measured. The algorithm used to define a right scattering count in the BBC is shown in Fig. 2.5. A right scattering event must record a signal in tiles 2 and/or 3, must record no signal in tiles 5, 6, 9, 10, 11, 14, 15, 16,

and has no requirements about whether a signal is recorded in 1, 7, 8, 4, 12, or 13. Other choices were considered but this algorithm was demonstrated to measure the largest asymmetry. Assuming beam polarizations of 60%, A_N is measured in 2006 data to be $\sim 8.1 \times 10^{-3}$[34]. The decrease of beam polarization was also measured and found to be quite small, $\leq 0.01 P_B$ per hour.

For a vertically polarized beam no up-down asymmetry should exist. Likewise, for a pure longitudinally polarized beam no left-right nor up-down asymmetry should be seen. Measuring up-down and left-right asymmetries can then give us a good indication of the true beam polarization direction. For longitudinal collisions this fact can be used to prove that the Spin Rotators are properly rotating the spin directions and to measure any non-longitudinal beam polarization vector component (see Sec. 8.2 for this calculation).

2.3.2 Scaler Boards

Access to raw BBC counts and beam spin orientations comes through the STAR scaler system[35]. The scaler system is a 24 bit VME memory module that stores data at the RHIC crossing rate of 10 MHz. As discussed in reference to Fig. 2.1, during proton-proton collisions one beam is cogged with single-alternating polarization orientation and the other is cogged with double-alternating polarization orientation. The desired effect is that over the course of an $\sim$ hour long data-taking run that the relative populations of events from beam bunches cogged 'up-up', 'up-down', 'down-up', and 'down-down' are nearly equalized. Fig 2.6 shows the raw collision event count for events satisfying the MB trigger condition versus bunch crossing ID. A separate scaler system integrates the bunch-sorted counts from individual BBC tiles. We calculate the relative luminosity and the non-longitudinal beam polarization vector component from these integrated counts
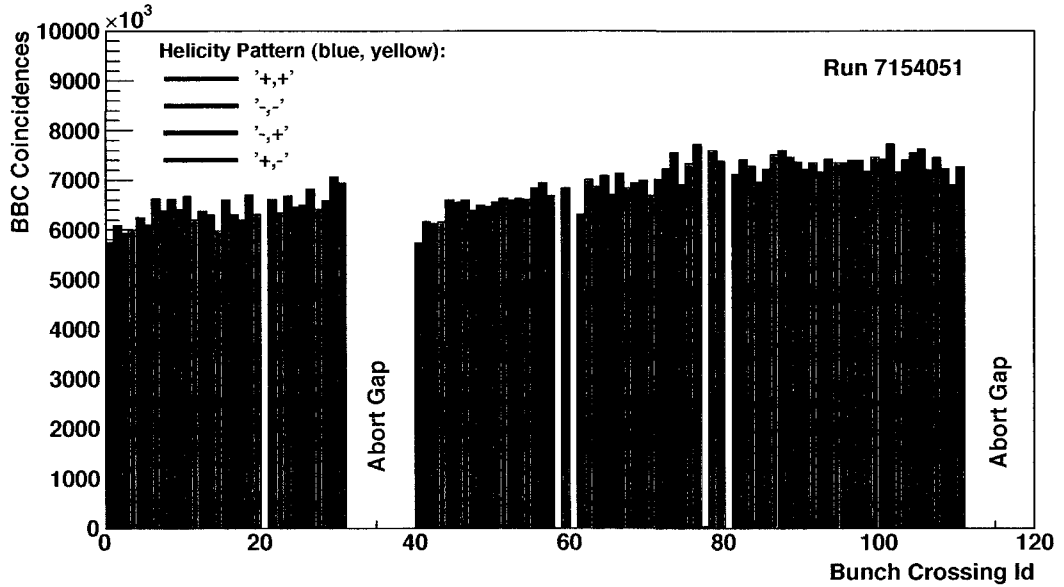
Figure 2.6: Number of BBC counts satisfying the MB trigger condition vs. bunch id for Run 7154051. The beam helicity pattern for each bunch is indicated as are those bunches used as abort gaps for the two beams.

(the latter is discussed in detail in Sec. 8.2).

2.3.3 Time Projection Chamber

The Time Projection Chamber (TPC)[36] at STAR is a gas filled drift chamber used to measure the momenta of tracks and reconstruct the primary vertex of hard collisions. The TPC, shown in Fig. 2.7, has a length of 4.2 m and a diameter of 4 m (subtending an active region of $|\eta| < 1.6$). It is filled with P10 gas (90% argon, 10% methane) and kept 2 mbar above standard atmospheric pressure. The TPC is housed within the 0.5 Tesla solenoidal magnetic field, and the -28 kV central membrane combined with concentric outer field-cage cylinders provide a uniform ~ 135 V/cm electric field within the volume.
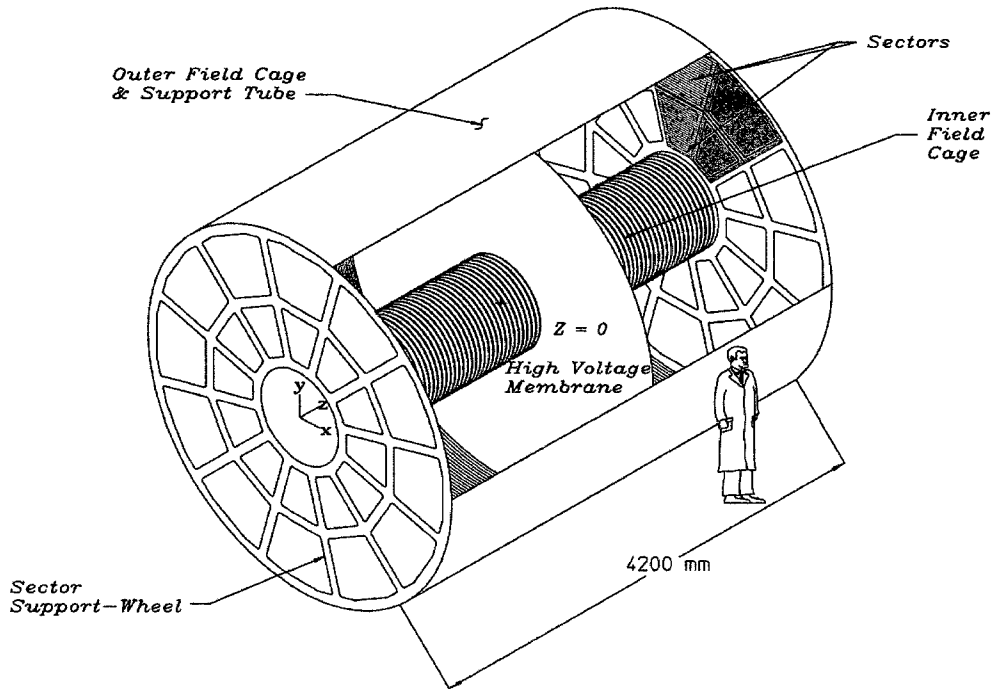
Figure 2.7: The STAR TPC.

The readout system consists of Multi-Wire Proportional Chambers with read-out pads located at both the east and west ends of the TPC. As charged particles travel through the gas volume, ionization electrons are released and drift at a constant velocity (v_{drift}) towards the ends. Avalanches are created as these electrons approach high voltage anode wires, with each avalanche producing an electron-ion plasma near the wire. Positive ions within this plasma temporarily induce an image charge on the readout pads. Two coordinates are measured from the location of this induced signal on the readout pads. The third coordinate is measured from the time the ionization electrons take to drift to the end. This drift time measurement is dependent on a reliable knowledge of v_{drift} during that run. Dedicated calibration runs are interspersed during data-taking using lasers with

30

well-defined paths to generate artificial tracks. v_{drift} is found to be 5.45 ± 0.01 cm/µs, with time dependent fluctuations on the order of 6%.

Charged particles traversing the TPC volume bend due to the magnetic field and follow helical trajectories. The trajectory of these tracks can be reconstructed very accurately due to the large number of readout pads, 136,608 in total. Momenta are measured from these reconstructed trajectories over the range of ~100 MeV/c to 30 GeV/c. The lower momenta cutoff results from the 0.5 m inner radius of the gas volume and the upper momenta cutoff represents the TPC's inability to resolve the curvature of particles above ~ 30 GeV/c.

Embedding simulated tracks with at least 10 pad hits into data events allows us to estimate the momentum resolution and tracking efficiency of the TPC. The momentum resolution is reproduced well with MC and depends slightly on particle species. $\Delta p_T/p_T$ for the $\pi^{\pm}$ (the most common charged particle found in jets) rises linearly as a function of p_T with a minimum at ~ 2% and 300 MeV/c. We can also embed these simulated tracks into events where we've already reconstructed a jet. From this we can count how many of the tracks fall within the jet fiducial volumes and how many are actually reconstructed in the jets. The tracking efficiency in jets is measured to be 87%, commensurate with the mean tracking efficiency for all tracks in the TPC. The main features of the tracking efficiency are found to match between data and MC, and a conservative estimate of the uncertainty on our values is ~ 5%.

2.3.4 Electro-Magnetic Calorimetry

Two subsystems provide electromagnetic calorimetry (EMC) coverage overlapping STAR's TPC tracking acceptance, the Barrel EMC (BEMC)[37] and the Endcap EMC (EEMC)[38]. The BEMC is located within the STAR magnet and

31
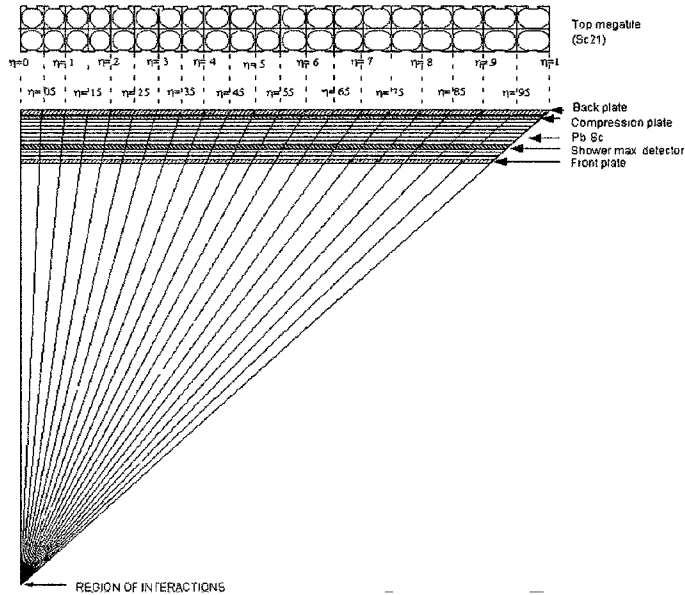
Figure 2.8: A cutaway of one half of the BEMC detector (a single module) is shown demonstrating the η tower segmentation. Each tower is projective by design to point back to the nominal interaction point at STAR.

covers 2π in azimuth and $|\eta| \leq 0.98$ in pseudorapidity. The EEMC is located at the western end of the STAR TPC, covers 2π in azimuth, and extends the psuedorapidity coverage in one direction to $1.08 \leq \eta \leq 2$.

The BEMC is segmented into 120 modules, each covering an acceptance range $0 < \eta < 0.98$ (or $-0.98 < \eta < 0$) and $\Delta\phi = 0.1$. Every module is further divided into 40 towers, giving 4800 in total. Towers are projective in design and point back to the nominal interaction point as shown in Fig. 2.8. Fig. 2.9 displays the construction of an individual module, giving a cross section of two adjacent towers. Every tower consists of a stack of alternating layers of lead and plastic scintillator and covers 0.05 in ϕ and η. The total depth of a tower at $\eta = 0$ is 20 electromagnetic radiation lengths $(20X_o)$. Positioned at approximately $5X_o$ are two layers of gas wire pad chambers constituting the

32
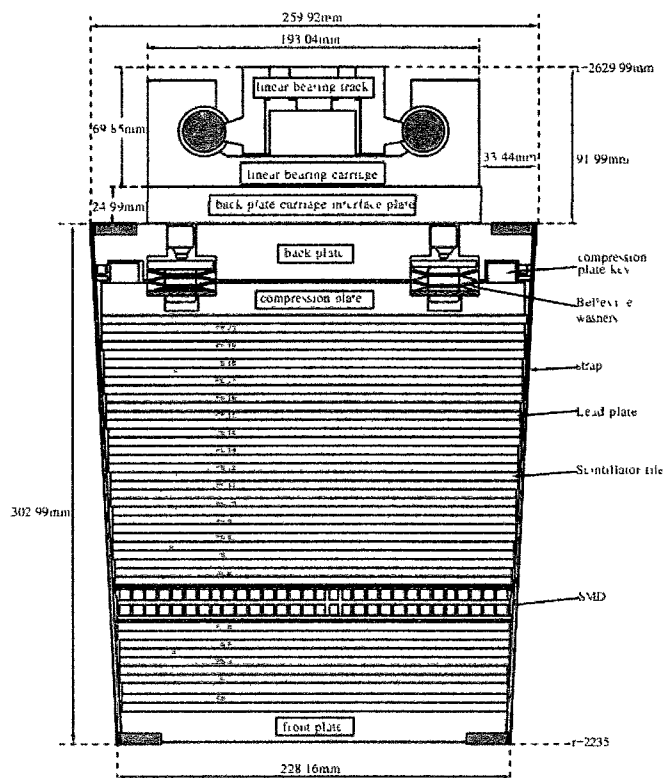
Figure 2.9: A cross section view of a single BEMC module consisting of alternating layers of Pb/plastic scintillator and support structure.

Shower Maximum Detector (SMD). The SMD is not used in this analysis, but provides higher spatial resolution than towers if necessary. The EEMC also uses a Pb/plastic scintillator tower construction with 720 towers segmented with varying coverage $(0.05 - 0.1) \times 0.1$ in η, ϕ. Both the BEMC and EEMC use optical fiber readout systems to transport scintillation signals to PMT tubes outside of the magnet solenoid for ADC digitization.

The PMT High Voltages are iteratively equalized as a function of η during the first week of any RHIC Run to allow a uniform ADC threshold for triggering (see Sec. 2.3.5). Calorimetry at STAR is designed to contain a 60 GeV elec-

tromagnetic shower, and the voltages are set accordingly After the data has been collected, a multiple step offline calibration of the gains is performed[39] We calculate calibration coefficients (C) for each tower in order to translate the measured ADC values into energy ($E = C \, (ADC - ped)$) First, preliminary tower-by-tower calibration factors are calculated using clean isolated MIP spectra (see Fig 2 10) Test beam data and simulations provide the conversion from MIP ADC peak location to energy[40] Next, the data is scanned and electron tracks are isolated from hadron tracks using tight dE/dx seperation cuts These reconstructed electron tracks are then required to spatially match with energy measured in a single tower Towers within the same η bin are combined and E_{tower}/p_{track} is calculated for that η range The deviation of the mean value from 1 0 in each of these bins, as demonstrated for a mid-rapidity bin in Fig 2 10, provides a final relative energy scale factor for all the towers within that bin The uncertainty on these final calibration coefficients is found to be 1 6%[39] The leading sources of bias arises within the electron sample due to the EMC trigger conditions (see the next section) and to timing calibration

2.3.5 Triggering

STAR s trigger[41] is a multi-leveled pipeline system that relies primarily on fast detectors for event selection ADC signals from the BBCs and BEMC are examined in level 0 (L0) at the RHIC crossing rate of 10 MHz An initial decision is made entirely from ADC thresholds, and if these thresholds are met the event is then sent for further examination to a level 2 (L2) CPU-farm In L2, information for all 4800 towers is available and ADC signals here are pedestal-subtracted and gain-corrected so that thresholds are expressed in E_T When an event is accepted by L2, the trigger system notifies the STAR Data Acquisition (DAQ)[42] to read
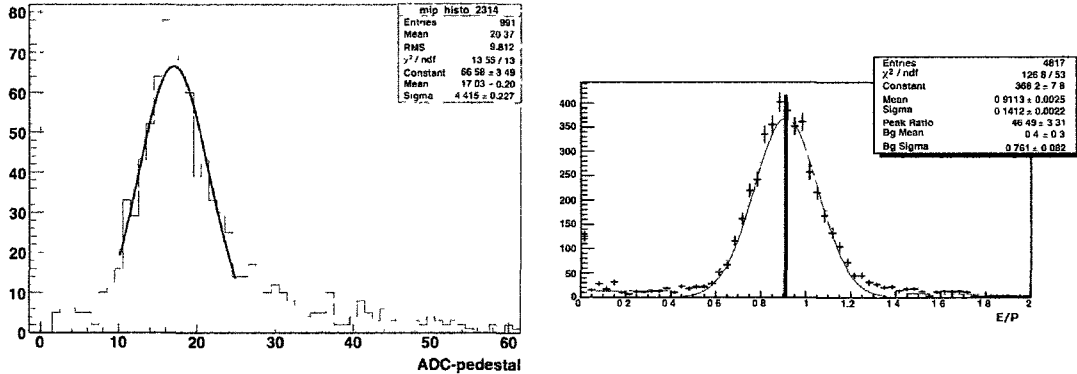
Figure 2.10: Left: A pedestal subtracted MIP peak for a single tower fit with a gaussian. Comparison of this peak location from tower-to-tower provides a first order calibration coefficient. Right: The electron E_{tower}/P_{track} spectra for all the towers within a single η ring. Deviation from 1.0 provides the final absolute energy scale correction for all the towers within this ring[39].

out all fast and slow detector information. In this analysis, four distinct triggering setups, each selecting on slightly different characteristics of the collisions, are analyzed.

The MB trigger is a baseline trigger requirement for all STAR physics triggers analyzed here. A MB-alone trigger provides a data sample with very little neutral energy bias and for this reason is a good crosscheck for a cross section measurement. However, the MB-alone trigger cannot provide sufficient statistics of highly energetic jets given a finite data collection period. We prescale the MB-only trigger and use additional electromagnetic conditions on top of a MB coincidence to increase the population of higher energy jets. HighTower (HT), JetPatch (JP), and HighTower+TriggerPatch (HTTP) conditions are added.

The HT trigger requires a single BEMC tower to record energy deposited greater than 5.4 GeV. In L0 this corresponds to an ADC signal greater than 24.

The JP trigger requires a BEMC jet patch region of η x ϕ = 1.0 x 1.0 to record energy greater than 7.8(58) in GeV(ADC). The HTTP trigger requires successive thresholds specified in L0 and L2. In L0 a tower must record 3.5(16) GeV(ADC) and a trigger patch (a predetermined 3 × 3 tower region in the BEMC) must record energy greater than 4.3(19) GeV(ADC). The event is then passed to L2 where the tower must record energy greater than 3.8 GeV. 3 × 3 trigger patch E_T sums are recalculated in L2 centered now on this particular high tower and a threshold of 5.2 GeV is applied.

By design there is a large overlap between these three BEMC triggers at high energy. The main source of jet statistics in the analyses presented in this dissertation come from the JP condition, which is the trigger specifically setup to find jet events. HT and HTTP triggers have other physics measurements as their primary focus but are nonetheless used to increase statistics in our lower energy bins.

In addition to these physics triggers, there are a number of diagnostic triggers. Zero-bias (ZB) events are taken interspersed during all physics runs. ZB events require a bunch crossing but no other detector conditions and so can be used to measure luminosity dependent effects like pile-up and beam background. Additionally, multiple times during fills, normal data collection is stopped and laser events are taken. Laser events are used mainly to calibrate the TPC drift velocity. These diagnostic triggers comprise a very small fraction of overall data taking.

CHAPTER 3

Jets at STAR

3.1 Jet Finding and Reconstruction

In the ideal case, the measurements presented in this thesis would be expressed in terms of final state parton momenta. This would give us a direct measure of the collision dynamics of interest and could be defined more precisely by theorists. However, individual partons have never been seen in the lab. Instead, what we measure at STAR are experimental signatures of the decay particles resulting from parton fragmentation. The job of jet algorithms is to group and construct these measurements into a jet with properties that relate to the parent parton. In this sense, a jet is our best approximation at "seeing" the bare parent parton.

The jet algorithm used in this study is the Midpoint Cone algorithm[43] (MCA) that was originally devised for the Tevatron. The MCA at STAR clusters all TPC tracks and BEMC/EEMC towers within a cone of radius

$$R_{CONE} = \sqrt{\eta^2 + \phi^2} \tag{3.1}$$

We use a cone radius of 0.7 from geometrical considerations and a desire to fully contain the parton fragmentation energy. A cone radius of 0.4 was used in our previous published inclusive jet cross section[13], where only half of the BEMC was instrumented. With full acceptance a larger cone radius is possible. Re-

constructed jet four momentum is defined by summing the constituent momenta as

$$P_{JET}^{\mu} = \sum_{i=0}^{n} P_i^{\mu} \qquad (3\ 2)$$

Tracks are assigned the mass of the pion in this sum. Conversely, towers are assumed to be photons and assigned zero mass as an approximation based on the most probable particle species

The algorithm begins by mapping all 'hits' (towers and tracks) with $E_T > 200$ MeV into an η, ϕ grid. Hits that lie in the same grid element are summed together according to Eq 3 2. Care is taken to account for double-counting, where a single particle's momentum and energy are both registered. Grid elements that contain tracks pointing directly to a tower with energy are corrected. For each track-tower pair, the most probable hadron EMC energy deposition (the MIP or "minimum ionizing particle" energy) is subtracted from the tower. This varies between 250 - 350 MeV depending on η (see Sec 4 8 for further discussion). If the corrected energy in the tower is less than zero the tower energy is set to zero

An E_T ordered list (high to low) is created from this grid. Grid elements with E_T above 0 5 GeV serve as "seeds" and are used as an initial thrust axis in jet finding. Hits within R_{CONE} of this seed are clustered and the centroid $(\overrightarrow{P_{JET}}/|P_{JET}|)$ of this candidate jet (proto-jet) is calculated. For the proto-jet to be considered stable, the original hit seed location and centroid must be aligned. This process is iterated until this condition is met. After all stable proto-jets are found, a midpoint test seed is generated for any 2 proto-jets with a separation distance $d_{seperation} < 2\ R_{CONE}$. This midpoint seed is also tested to see if it generates a new stable proto-jet. All stable proto-jets are also required to have energies greater than 5 GeV
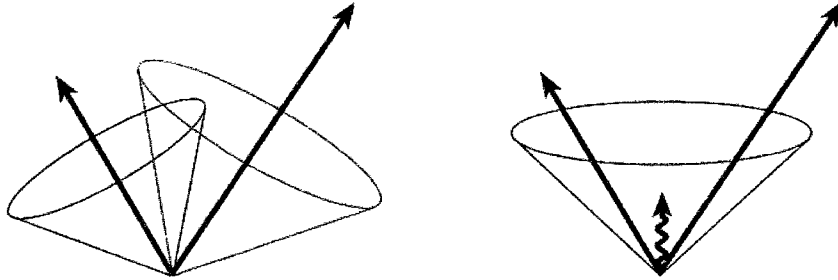
Figure 3.1: The effect of soft radiation on seed-based cone jet algorithms not using the midpoint method.

Finally, stable proto-jets are passed to a split/merge function designed to account and correct for proto-jet overlaps. Starting from the highest E_T proto-jet though to the lowest, the shared hit energy is calculated between neighbor proto-jets. If the shared energy is greater than 50% the 2 proto-jets are merged; otherwise, they are split and shared hits are associated by proximity to the 2 proto-jets. The remaining proto-jets are now 'found' jets and their final four momenta is calculated via Eq. 3.2.

The MCA solved one of the major theoretical challenges encountered in early cone algorithms: infrared safety. To be consistent and stable, jet algorithms must be fairly insensitive to soft radiation in an event. Cone algorithms that utilize seeds with set thresholds, however, can be very sensitive to this. Fig. 3.1 illustrates the problem. In the case of two high energy particles and no soft radiation, the cone algorithm will find two distinct jets (left). However, a soft particle in the event with $E_T > E_T^{SEED}$ will be seen by the algorithm as a seed and result in a single found jet (right). The MCA removes this dependence by

directly adding midpoint seeds between stable proto-jets into jet finding.

Recent advances in jet algorithms have produced for the first time a Seedless Infrared Safe Cone algorithm (SISCone[44]) with managable computation time. This is a welcome advance, since seed thresholds can introduce biases and have historically been used primarily to save computation time. Soyez and Salam[44] argue that infrared safety problems persist at the NNLO level in the MCA. The addition of the midpoint in jet-finding just pushed this problem from NLO to NNLO. They study the inclusive jet channel and find agreement between MCA and SISCone to NLO with modest changes at NNLO. Since the theoretical calculations of interest in this study are NLO, switching algorithms to SISCone is not necessary.

3.2   Simulation Methodology

Jet finding and reconstruction using the MCA as described above is performed on events from both experimental data and Monte Carlo (MC) simulation. MC simulation at STAR ulitizes PYTHIA[45] to generate the hard scattering event and GEANT[46] to characterize the detector response to that event. Jet finding is run both at the PYTHIA level (Particle jets) and at the PYTHIA+GEANT level (Detector jets) to quantify the effects of our detectors. Trigger decisions are also simulated for 2006 STAR working conditions by replicating the underlying ADC logic. A MC event can therefore be brought through the STAR detector simulation and tested to see if it would have fired our triggers. MC jets that reconstruct in our detector simulation and survive the trigger conditions are labeled Detector jets.

Simulations must account for time dependent trigger and detector conditions.

Chapter 4 discusses in detail the quality assurance procedures that were performed on all available 2006 data runs. Runs that pass this reduction analysis represent four main data-taking time periods with different trigger thresholds and prescales as listed in Table 3.1. To properly simulate this, the full MC sample was divided into four sub-samples, each corresponding to the fraction of the final data collected with that trigger setup. A snapshot of the STAR detector within each time window is then chosen to represent the performance during that time period. Snapshots are chosen based on the average 'live' BEMC tower fraction during the time period and on matching the data/simulation jet η and ϕ structure. The BEMC's primary role in both triggering and energy measurements make its' operating conditions vitally important. A more thorough discussion of the calorimeter status is found in Sec. 4.2. Each sub-sample is then thrown into our GEANT+TRIGGER simulator with the conditions relevant to that snapshot. Fig. 3.2 show data/simulation comparisons of jet η,ϕ after adding all the individual MC sub-samples back together. The agreement is very good.

Figure 3.3 shows the raw jet p_T spectrum and jet track multiplicity ($< nTracks >$ /jet) as a function of jet p_T for data and MC. Track multiplicity distributions match very well and indicate that contributions to the jet energy from the TPC are also properly simulated. The slight mismatch in the raw falling jet p_T spectrum between data/MC is accounted for in both the cross section and asymmetry analyses by MC re-weighting procedures (Sec. 5.3.3 for the cross section, Sec. 7.4.2 for A_{LL}).

Figure 3.4 shows a MC/data comparison of the jet p_T resolution. This figure is formed from a comparison of the two measured jet p_T values in di-jet events and represents our fundamental p_T resolution arising from the combination of calorimeter and tracking detector resolutions. This resolution is important in

	Runs 7131043-7132027	Runs 7132062-7133051	Runs 7133052-7135028	Runs 7135067-7156028
Dates	May 11-12	May 12-13	May 13-15	May 15-Jun 5
JP1	7.8	8.3	8.3	8.3
HT2	None	5.4	5.4	5.4
HTTP Level-0	3.5 (HT)	4.0 (HT)	3.5 (HT)	3.5 (HT)
	4.5 (TP)	4.5 (TP)	4.3 (TP)	4.3 (TP)
Level-2	3.0 (HT)	3.0 (HT)	3.80 (HT)	3.80 (HT)
	4.79 (TP)	4.79 (TP)	5.10 (TP)	5.20 (TP)
Prescale	None	HTTP: 56% ps=2 44% no ps	None	None
Fraction	1.5%	9.8%	10.9%	77.8%

Table 3.1: Trigger configurations during the second longitudinal running period in 2006 at RHIC. All thresholds are expressed in terms of GeV. Percentage numbers represent the fraction of data taken with the threshold for that column and the indicated prescale condition.

light of the steeply falling jet yield spectrum in Fig. 3.3 and motivates a series of jet p_T corrections in both the asymmetry and cross section analyses. The resolution is calculated in Fig. 3.4 from our full p_T range and shows a good agreement between MC/data with a width of $\sim 23\%$.

PYTHIA provides a simulation data sample that appropriately accounts for the hard scattering sub-process mixture (qq, qg, gg) found in $\sqrt{s} = 200$ GeV proton-proton data. However, PYTHIA cannot account for initial state parton polarization. For systematic uncertainty calculations we will want to have a polarized MC sample to test in our detectors. To accomplish this, each theory collaboration has provided grids in x and Q^2 of the polarized parton distribution function (PDFs) from each of their models (the grids are compiled and posted at [47]). A set of simulated events can then be "polarized" by weighting each event in the sample based on its flavor, x, and Q^2 values according to the PDFs for a given model. Due to the fact that there are many allowed theoretical models of polarized gluon, quark, and sea quark contributions, we cannot restrict the underlying polarization models in our analysis and must include as many as possible. Polarized MC models at both the Particle and Detector jet levels are shown and discussed in detail in estimating the systematic uncertainty on A_{LL} arising from the trigger and jet reconstruction bias (Sec. 8.1).
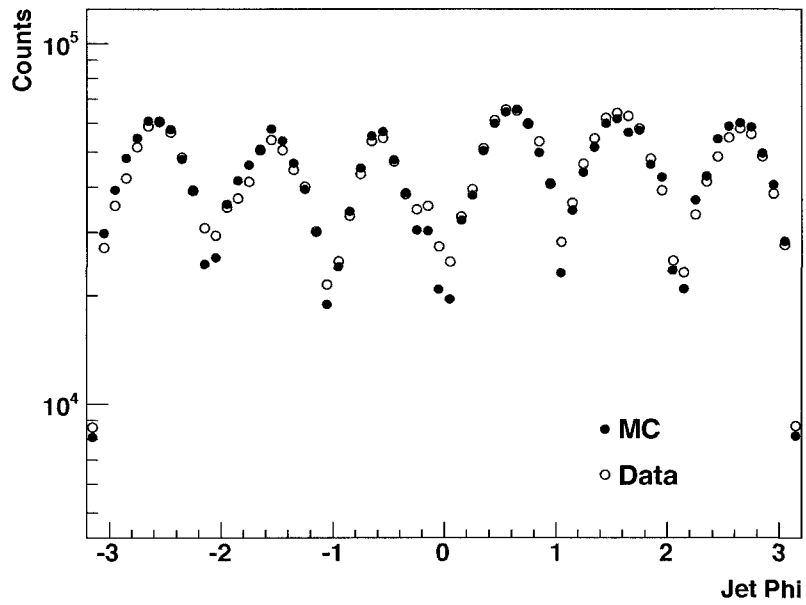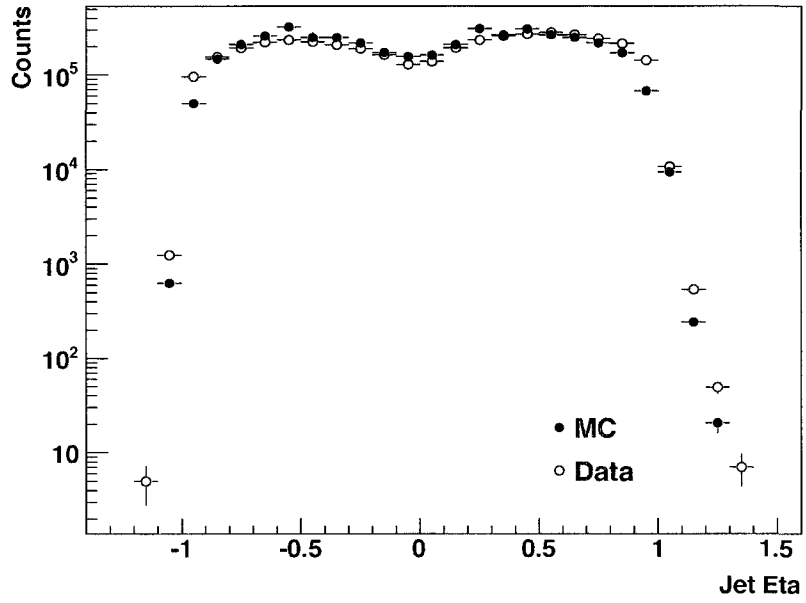
Figure 3.2: MC/data comparison figures of jet η (top) and ϕ (bottom) distibutions after recombination of separated MC sub-samples.
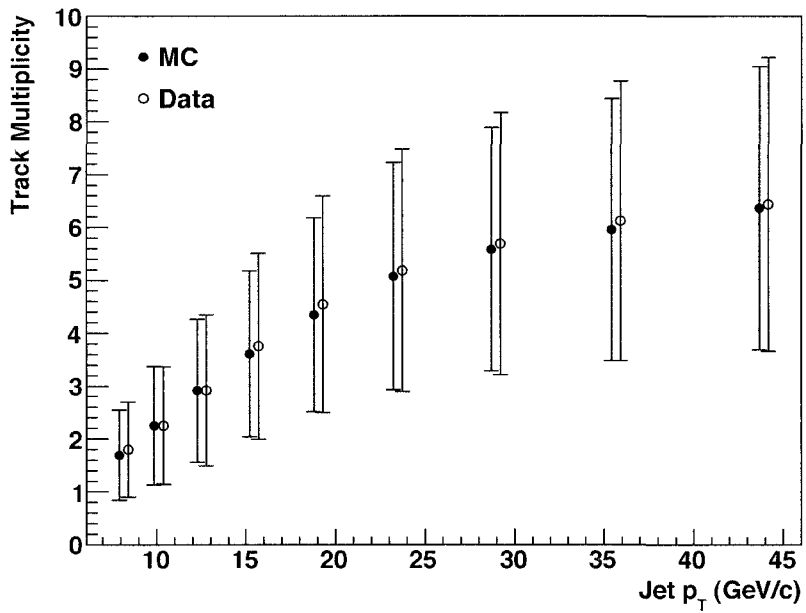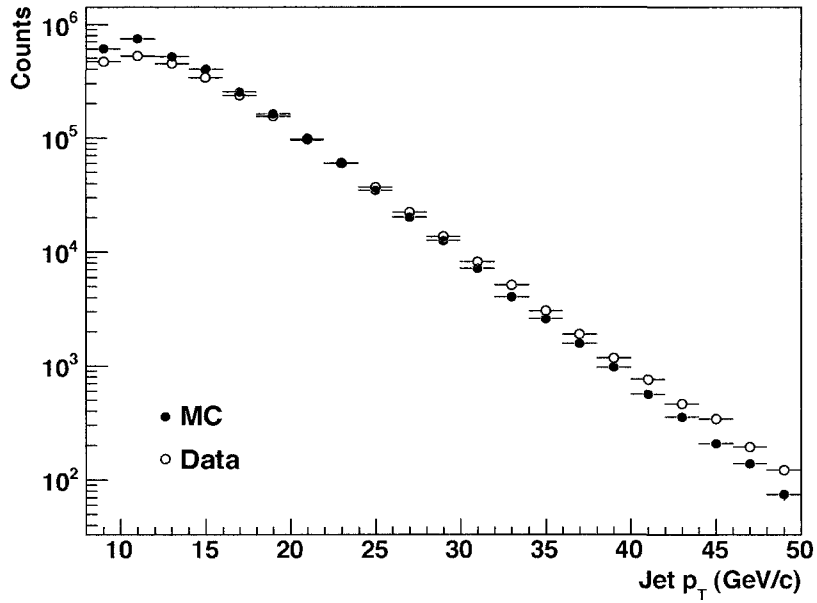
Figure 3.3: MC/data comparison figures of the raw jet p_T spectrum (top) and $< nTracks > /jet$ as a function of p_T (bottom).
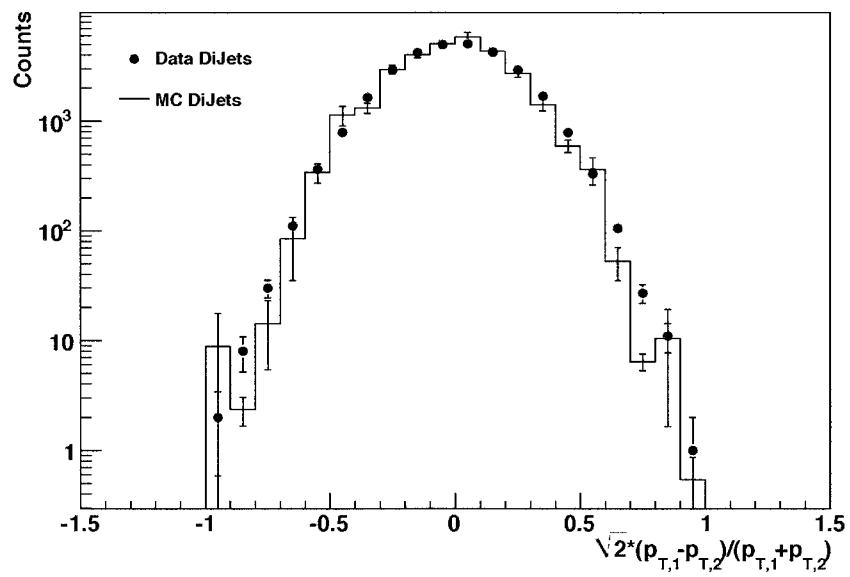
Figure 3.4: MC/data comparison of the jet p_T resolution for di-jet events.

CHAPTER 4

Data Reduction

4.1 Run Selection

Data collection at STAR is segmented into runs lasting on average about an hour. Runs used in this analysis contain a mixture of events selected by HT, JP, and HTTP triggers. Before inclusion in our analysis, all runs are examined for problems that occur during data taking that could affect our measurements. Jet and event characteristics directly related to hardware performance are studied for each run individually to find any time dependent hardware issues.

The list of jet and event characteristics studied run-by-run is extensive. Examples include: event vertex distributions, mean number of jets in events, mean jet and track ϕ and η, jet p_T distributions, track and tower p_T distributions, mean number of tracks and towers in jets, MB-normalized jet yields for each trigger, etc. Data from each trigger is examined independently. For the asymmetry measurements, runs must also contain the correct bunch-dependent spin information and several runs are excluded on this basis (see Sec. 7.1 for further discussion of this quality assurance). Asymmetry measurements also rely on valid measurements of the beam polarization and relative luminosities. Examples of issues discovered in the process of this quality assurance include runs with calorimeter and TPC high voltage trips, runs with calorimeter hot towers and pedestal shifts,

as well as runs taken during polarization measurements and van der meer scans.

Runs are discarded from analyses if severe hardware problems are discovered. A substantial effort is made, however, to save as much data as possible. For example, tower-by-tower or crate hardware issues with the BEMC are dealt with by excluding individual detector elements within the given run as opposed to removing the entire run (discussed in Sec 4.2). Shown also in Sec. 4.3 is an example of a TPC hardware problem discovered in our analysis. The data was able to be saved after a re-calibration for a problematic subset of runs.

4.2   BEMC Hardware Performance

The BEMC is the primary instrument for both triggering and energy measurement in this analysis. A close inspection of the BEMC performance is therefore required. After data is collected, we perform an offline analysis of all BEMC towers to identify hardware problems. The expected ADC output of tower PMTs from MB triggered data is a gaussian pedestal peak with an exponential tail (Fig. 4.1). We test these ADC distributions from each tower for a variety of problems, including high voltage problems, stuck bits, large-scale crate malfunctions, and dead channels. We also demand rather loose cuts on the pedestal peak location and width to keep the entire spectrum within a reasonable range. In the end, every tower is given a numerical value that we store in a 'status' bit. These status bits are accessed later in our analysis and indicate whether the tower passed our criteria ('good' status) or not ('bad' status) and which test(s) it failed.

The status for each of the 4800 towers is determined on an almost run-to-run basis. Single tower high voltage and ADC problems are the most common. A tower with a high voltage problem either is noisy or is unresponsive. For each
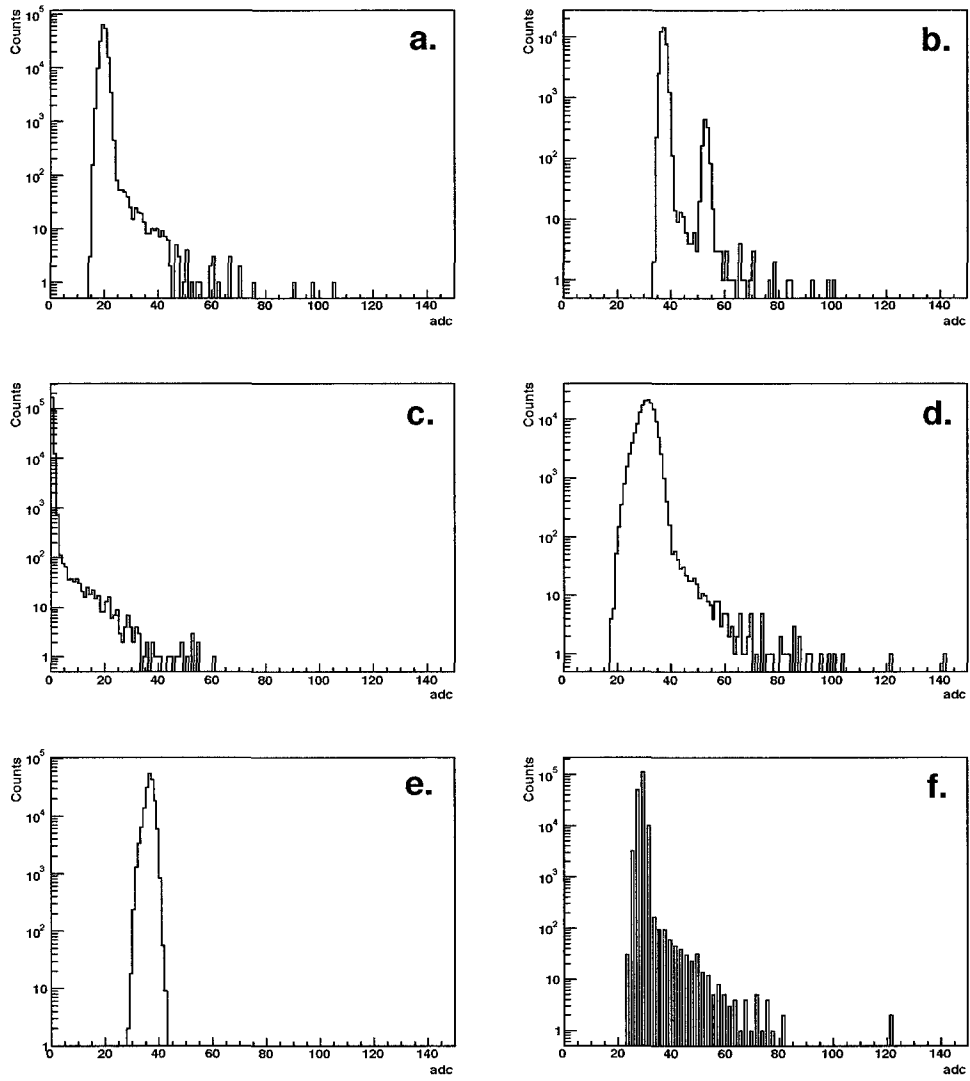
Figure 4.1: Example tower ADC distributions with different statuses: a.) good, b.) hot, c.) pedestal peak out of range, d.) wide pedestal peak, e.) cold, f.) stuck bit.

tower, we tally the number of 'signal' counts, which we define as an ADC hit above $10 * pedestal\ width + pedestal\ mean$. We can then calculate the mean number of signal counts over all the towers in a run and compare each individual tower to this mean. Towers with 10 times more counts than the mean are labelled 'hot'; towers with 1/40 less counts than the mean are labelled 'cold'. Care is taken to distinguish between the conflicting effects of noise and large tower gains, the latter of which is corrected for in the data with offline gain calibration coefficients(see Sec. 2.3.4). In the case of cold towers, we adjust our cuts to reflect whether the tower is unresponsive or is usable, albeit with a very low gain.

BEMC electronics crates, which house 80 towers, occasionally exhibit problems. Crate malfunctions are detected using two main signatures. First, if a significant fraction of a crate's towers have high voltage problems, either hot or cold, the entire crate is flagged as bad. Second, we test for identical ADC output distributions from neighboring towers within a crate.

Three additional tests significantly clean up our data sample. We test for dead towers that have no counts above a pedestal subtracted ADC of 0. We check for stuck bits, both on and off, in the ADC distribution. Finally, the pedestal peak must be located within the range $0 < ADC < 60$, and we ensure that the width of the pedestal is within reasonable limits. Figure 4.1 shows examples of many of these problems found in the data.

As a final check, we perform a time-dependent analysis of the BEMC towers. Towers are sometimes found to fluctuate between good and bad status over the course of a fill, a day, or the entire data-taking period. Fluctuations indicate either that some characteristic of the tower's ADC distribution is numerically close to one of our testing thresholds or that there are inherent hardware instabilities. These situations are dealt with on a case by case basis, but generally the status
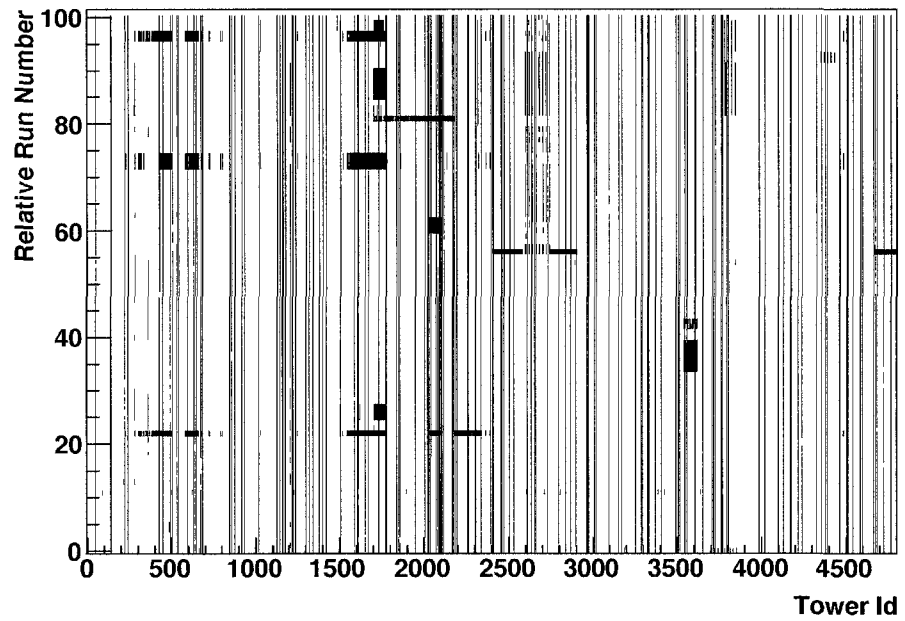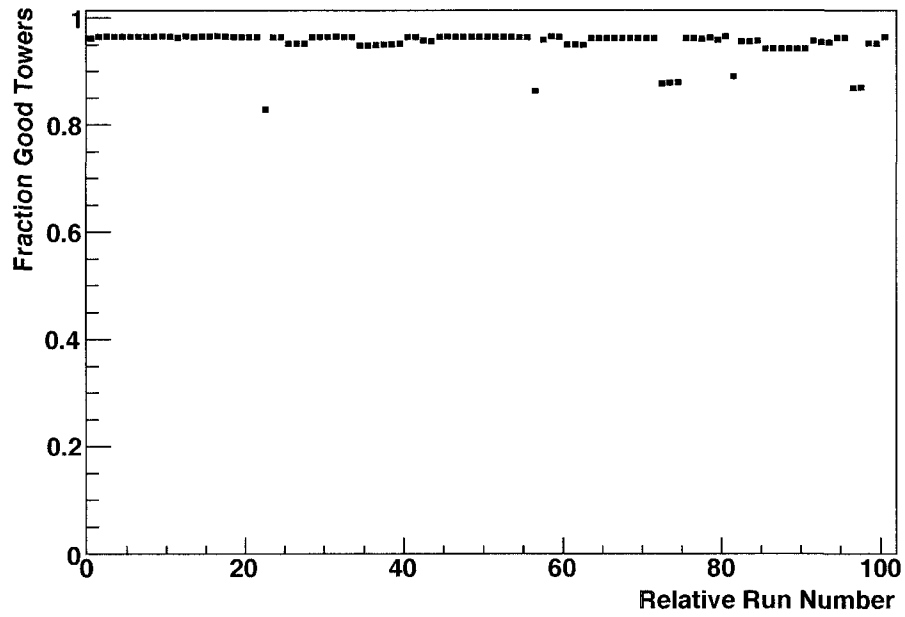
Figure 4.2: Top: Fraction of good towers as a function of relative run number over the entire data collection period. Bottom: Black represents towers which exhibited hardware problems and aren't included in the analysis.

is set constant throughout the time period to reflect the worst possible state of the tower

The 'live' fraction of the BEMC (towers with good status) as a function of relative run number is shown in Fig 4 2 The mean live fraction during 2006 longitudinal data taking was 95% with an RMS of 3%
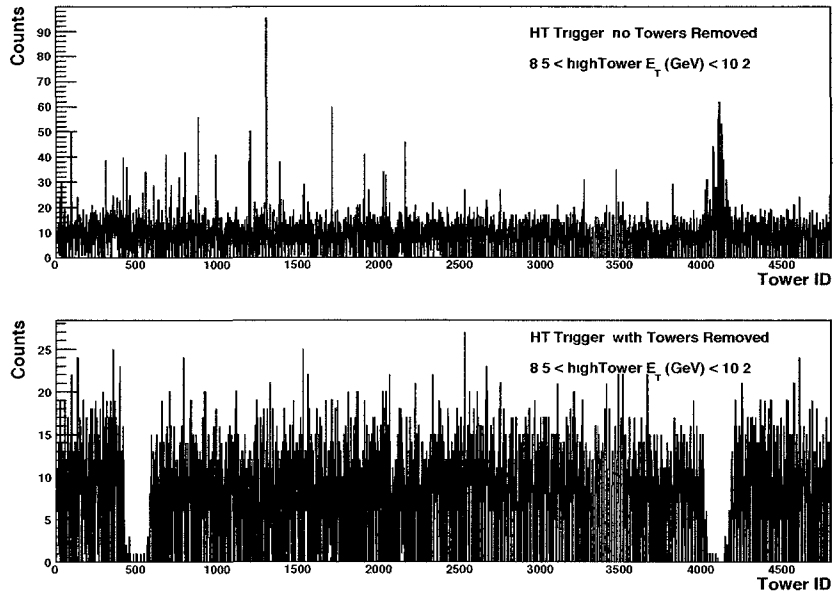
Figure 4 3 Tower frequency as a function of tower ID for HT triggered data This is shown for a single HighTower E_T bin before (top) and after (bottom) removing problematic towers and imposing a ϕ cut (discussed in Sec 4 7)

After jet reconstruction, we examine the frequency of each tower firing a jet We impose a strict uniformity in the cross section analysis and remove jets centered on towers that fire significantly more frequently than average A high frequency can indicate either a slight miscalibration or that the tower slipped by our tower status analysis for at least a portion of data-taking Fig 4 3 shows the tower frequency distribution for one E_T bin before (top) and after (bottom)

removing these towers. Towers in this figure are the highest E_T towers within jets that have passed all other data selection cuts. Shown is one E_T bin, but we examined spectra covering the entire range $0.0 < E_T(\text{GeV}) < 60.0$ to identify problems. The bump above ~ 4100 arises from background not associated with the hard scattering (this is discussed in detail in Sec. 4.7) and an additional ϕ cut to remove it has been placed. Following this investigation, we remove 320 additional towers from data and MC in the cross section analysis.

4.3 TPC Performance

The performance of the TPC for each run was studied to ensure uniformity of tracking over the entire data sample. Shown in Fig. 4.4 is a major drift velocity calibration problem that was discovered during our quality assurance analysis. Runs in red (open triangles) exhibited the problem and account for $\sim$20% of the final 2006 data sample. Events and jets within the problematic runs were reconstructed with fewer tracks on average. This is due to the fact that incorrect drift velocity values were used in offline track-finding algorithms resulting in lower track reconstruction efficiency for those runs.

This problem was caused by a power outage at the STAR detector platform on the evening of May 19, 2006. As a safety precaution, the TPC gas was diluted with Argon gas because the usual P10 mixture is flammable. Flow was resumed and a new gas mixture was introduced as soon as the power problems were re-solved. Instability in performance occurred for the next couple of days as the composition of the gas mixture stabilized. During this unstable period, a more finely-grained drift velocity calibration was required than the standard dedicated runs taken several times each fill. Experts in the STAR calibration group per-formed a run-by-run global re-calibration on the sub-sample and recovered the
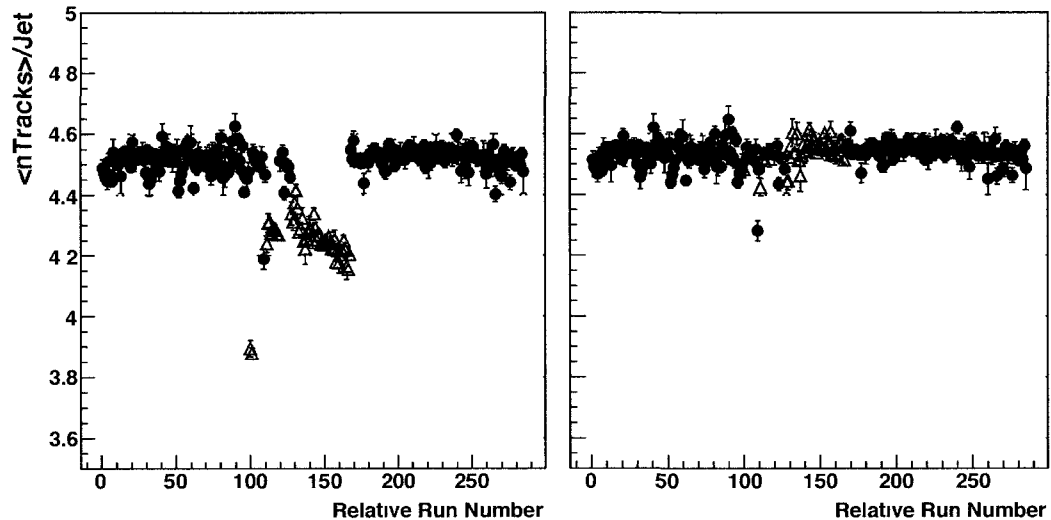
Figure 4 4 Track multiplicity as a function of relative run number for the data used in this analysis Runs in red (open triangles) exhibited a TPC calibration problem that was fixed in the final dataset Left before recalibration, right after

data

4.4   Vertex Selection

All jets included in this analysis come from events that contain a reconstructed primary vertex Primary vertices are calculated by projecting tracks in the event towards the geometric center of STAR using helical trajectories The vertex position is found iteratively by minimizing the summed distance of the vertex position from all these track projections Requiring that the event contains a primary vertex benefits us in two ways first, by requiring that all tracks within our jets originate from this vertex, we suppress background processes not associated with the hard scattering of interest, and second, by providing a long lever arm on

track-fitting (tracks are refit after a primary vertex is found) the primary vertex increases the track momentum resolution[48].
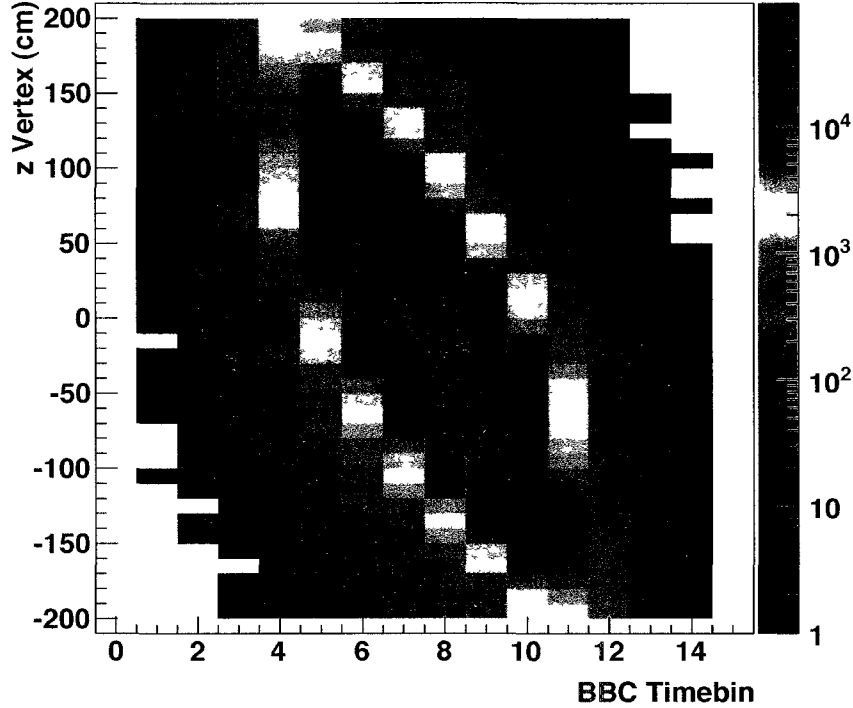
Figure 4.5: Reconstructed z vertex position (cm) versus the measured BBC time-bin for events containing at least one jet falling within our jet thrust axis cut.

Figure 4.5 shows the reconstructed z vertex location (+z direction is defined as west along the beam with 0 at the TPC center) versus the measured BBC timebin. Events in this plot contain at least one jet within the jet thrust axis cut discussed in Sec. 4.6. BBC timebins are measured as the time difference (in ns) between significant signals hitting both BBCs. Time buckets are not assigned linearly with time but are defined explicitly by an upper limit on time differences. Listed for each bin from 0 to 15 this upper limit in ns is (50, 125, 150, 175, 195, 215, 235, 255, 275, 295, 315, 335, 365, 390, 470, 512). The central bins are defined

with shorter time windows to allow finer granularity Despite the fact that the timebins are not linear with respect to time nor vertex (cm), there is a strong correlation between the reconstructed z location and the measured timebin, as seen in Fig 4 5

For the asymmetry analysis, the relative luminosity is measured by the BBCs (see Eq 7 4) A cut is placed on the BBC timebin (5 < BBC TB < 10) matching the cut in the relative luminosity calculation This keeps events within uniform TPC tracking and efficiency and is also imposed on the data in the cross section analysis Additionally, a second more strict cut of $|vertex(Z)| < 60\ 0$ cm is used in the cross section analysis to fully constain the event to well within our detectors

4.5 Software Trigger

In addition to the hardware thresholds used to select events, jets included in these measurements must pass several cuts designed to assure that each particular jet could have and should have fired the trigger Trigger simulation software at STAR takes the raw BEMC ADC values measured and simulates all the trigger logic and decisions, including the masking of problematic sections of the calorimeters Using this trigger simulation, we can tell whether or not the event should have fired any of our three main triggers and, if so, which HTs and JPs were responsible

A jet coming from a HT or HTTP-triggered event must contain a HT which the simulator determined should have fired the event Similarly, a jet coming from a JP-triggered event must have a thrust axis within 6° in ϕ and 0 1 in η of the edge of a JP that should have fired the event In the asymmetry analysis, the

OR-sum of the three main triggers is used in the final result. A jet that passes any one of the three above software trigger requirements is accepted. Conversely, in the cross section analysis, these conditions are applied individually to the HT and JP samples. Further, an additional and more conservative requirement is placed on the neutral energy in the jet to require that the jet is well above the trigger thresholds. In the HT trigger we require the energy of the highest tower in the jet to be above 6.0 GeV; in the JP trigger we require the sum of the tower energies within the jet patch that fired the event to be above 8.0 GeV.

4.6 Jet Pseudorapidity

A cone radius in η, ϕ of 0.7 is used in this study. Calorimeter and tracking coverage at STAR are $-0.98 < \eta < 2.0$ and $-1.3 < \eta < 1.3$, respectively. In order to contain jets within our active η region, we require the jet psuedorapidity to be within $-0.7 < \eta < 0.9$. This cut is asymmetric due to our asymmetric calorimeter coverage. As seen in Fig 3.2, the η spectrum is relatively flat within this cut window. The exception is at $\eta \sim 0$, where there is a dip due to the jet patch locations.

Two pseudorapidity definitions for each jet are useful in this analysis. The first, η_{jet}, is the pseudorapidity as measured through the reconstructed jet thrust axis (Eq. 3.2). The second, η_{Det}, is the pseudorapidity value where the jet actually hits the BEMC. From the jet pseudorapidity, $\eta_{jet} = -ln(tan(\theta_{jet}/2))$, η_{Det} is found by re-centering θ_{jet} to the BEMC coordinate system. We correct θ_{jet} with the measured z_{vertex} and BEMC radius of 231.0 cm (via $\theta = atan(r/z)$), and recalculate η. The cut listed above is made to η_{Det}. For the cross section analysis, cuts on η_{jet} and η_{Det} are both made ($|\eta_{Det}|, |\eta_{jet}| \leq 0.80$) to be conservative.

4.7 Neutral Energy Fraction Cut

Particles not associated with a hard scattering but moving with the beams can interact with our detectors and reconstruct in jets. These particles originate from either the beam halo or from deflections at the focusing magnets upstream of STAR and can traverse our detectors in time with MB events registered by the BBC. Figure 4.6 (left panel) diagrams how these particles strike our detectors. The right panel gives the number of jets vs. η and ϕ for mono-jet HT events. Lead shielding was installed between the 2005 and 2006 RHIC runs on both sides of STAR in an attempt to eliminate these background particles. The number of reconstructed background jets was reduced but not eliminated. A hole in this shielding near $\phi \sim 0$ on the positive η side persisted in the 2006 data.
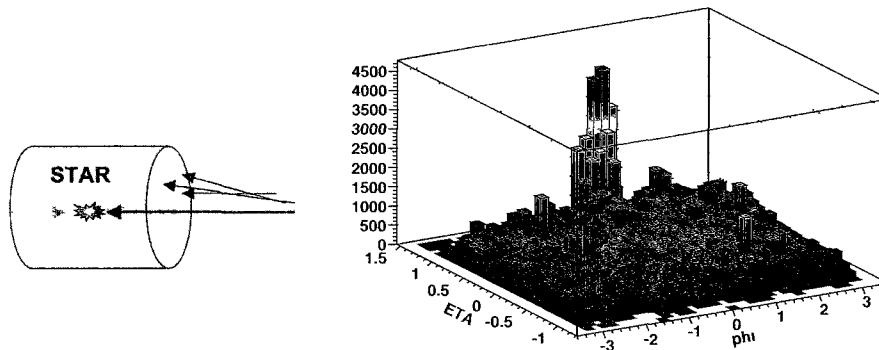
Figure 4.6: Left: A toy model showing a spray of background particles. Right: The number of jets are shown vs. η and ϕ for single-jet HT-triggered events. Note that no vertex reconstruction requirement is imposed in this figure to more effectively show the background area.

Due to STAR's calorimeter-based trigger, background events caused by particles traversing the calorimeters may be preferentially selected by the large amount

of neutral energy measured in the event. In jet reconstruction this translates into jets with a large fraction of their total jet energy derived from the calorimeters and little from tracking. Since these jets are not associated with a hard scattering, they are also more likely to be found in mono-jet events as opposed to multi-jet events. Fig. 4.7 shows the mono-jet and di-jet distributions as a function of jet neutral energy fraction (R_T, with R_T = EMC energy/total jet energy) for a single jet p_T bin. MC and data agree well for the di-jet distribution. However, due to contamination from these background jets, an excess in the mono-jet data sample over MC at high neutral energy fraction is visible.

On the right side of Fig. 4.7 is the ratio of the data mono- and di-jet distributions for that same p_T-bin. The ratio is fit with an exponential plus linear model. Here the signal is modeled as a linear contribution in the high R_T region and the background as an exponential contribution. This fit is performed on each p_T bin individually and the exponential decay constant α is extracted. We then determine a fixed value for α by fitting the spectrum of these extracted values plotted as α/P_T vs. jet p_T with a constant. The ratio distributions for each p_T bin are refit using this fixed α in the background model to determine the relative background fraction as a function of R_T.

Since there is both signal and background in the spectra at all values of R_T, care must be taken to determine the optimum cut. We approach this cut differently in the asymmetry and cross section analyses. For the cross section, we conservatively restrict our data to jets with $R_T \leq 0.8$ to remove as much of the background contamination as possible. We additionally remove all jets centered on towers within $\pm 12^o$ (four EMC tower rows) of $\phi = 0$. Conversely, in the asymmetry analysis we scan all cut values greater than 0.7 in an effort to minimize the sum in quadrature of the resultant statistical and systematic uncertainties.
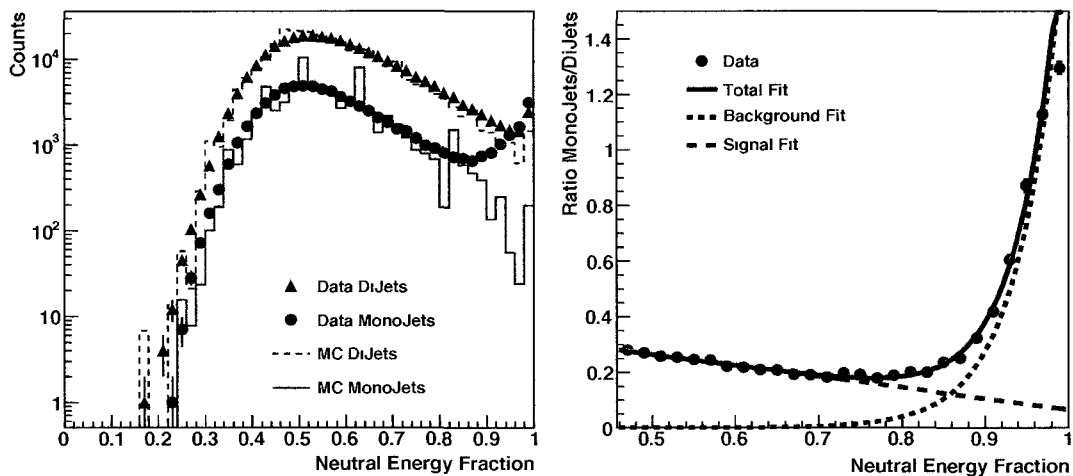
Figure 4.7: Left: Data and MC mono- and di-jet distributions as a function of jet neutral energy fraction. Right: The ratio of the data mono-jet/di-jet distributions shown left fit with an exponential plus linear model. Both plots are shown for the OR-sum trigger condition in a single jet p_T bin: 14.08 GeV/c $< p_T < 17.31$ GeV/c.

At each cut value and p_T bin, the systematic uncertainty from the remaining background contamination fraction is calculated and added in quadrature to the resultant statistical uncertainty from the surviving jets. This is discussed in more detail in Sec. 8.3, but a universal value of $R_T \leq 0.92$ is found to be the best choice for all p_T bins.

4.8 Jets with Double Counted Energy

As discussed in Sec. 3.1, when both the charged track momentum and electromagnetic energy of a particle are measured, we subtract a single MIP energy from the particle's four-momentum. If that particle is an electron, subtracting a
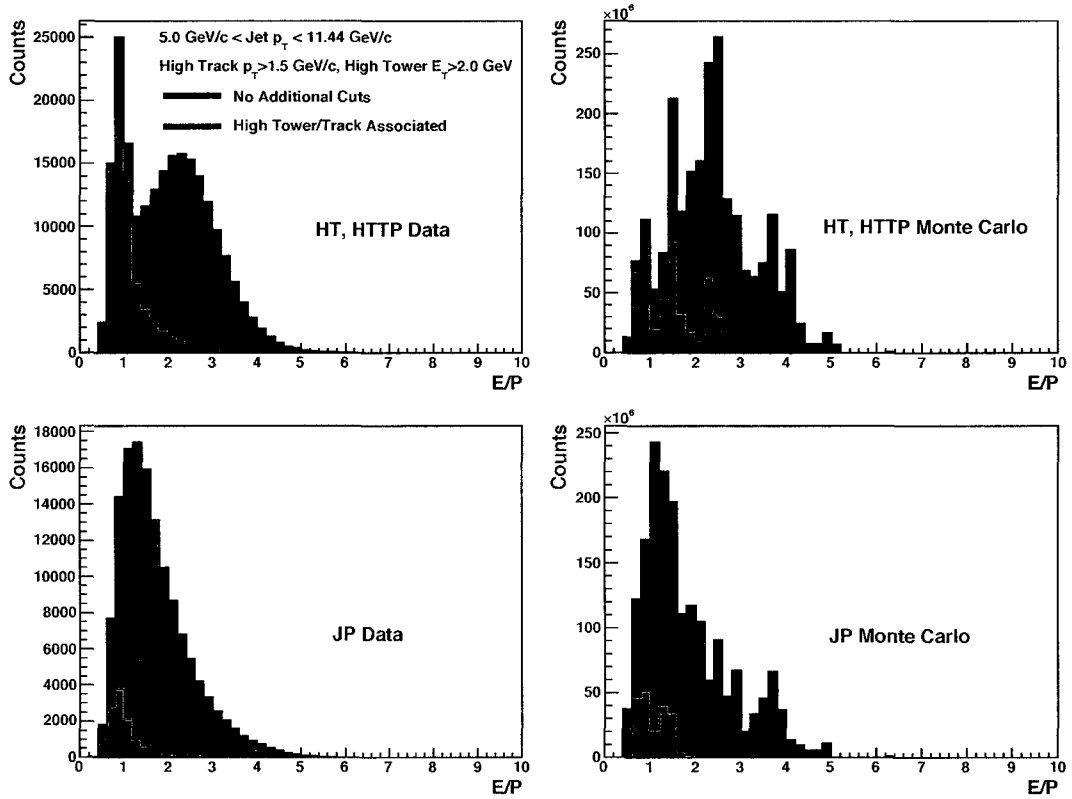
Figure 4.8: Energy/momentum distributions for the highest tower and track in jets with $p_T > 5.0$, < 11.44 GeV/c (blue). Overlaid in red is energy/momentum for spatially associated towers and tracks. Upper plots come from HT-triggered data and lower plots from JP-triggered data. Left column plots come from data and right column plots from MC.

MIP energy can still lead to a substantial overestimate of the jet energy. Charged particle tracking fully measures the electron energy and the electron additionally deposits all of it's energy into the calorimeters. If the electron is the leading particle in the jet, the jet's energy can be wrong by nearly a factor of two.

A discrepancy between MC and data for jets that exhibit this biased energy signature was discovered for a subset of the data. Figure 4.8 shows the E/P (high
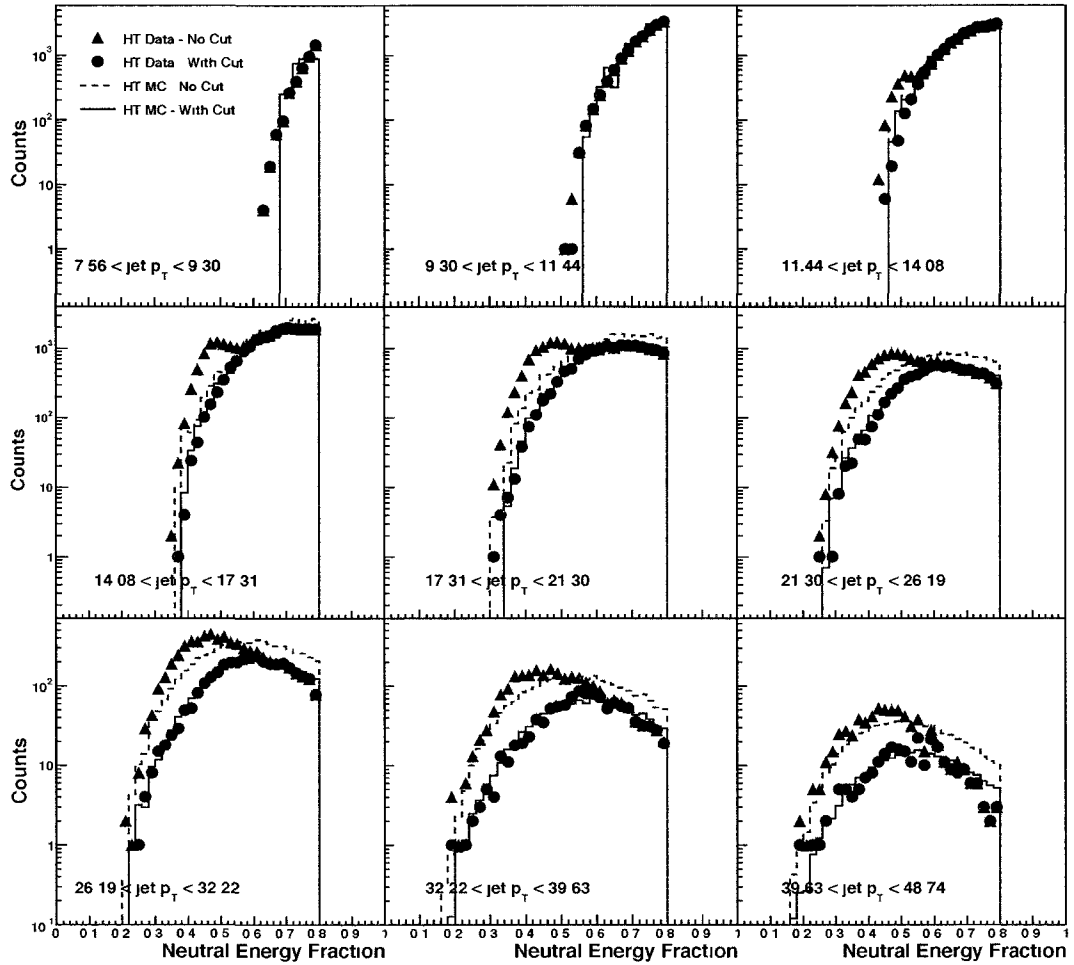
Figure 4.9: Neutral energy fraction distributions for HT data and MC with and without the energy double-counting cut. The comparison is shown for the cross section set of cuts (including a tight R_T cut) and for 9 separate p_T bins.

tower energy/high track momentum) spectrum for jets containing a track with $p_T > 1.5$ GeV/c and a tower with $E_T > 2.0$ GeV. The upper two plots display data (left) and MC (right) spectra for HT-triggered events (HT or HTTP trigger), and the lower two plots display data and MC spectra for JP-triggered events. A fairly restrictive cut of 5.0 GeV/c $<$ *Jet* $p_T <$ 11.44 GeV/c is additionally imposed on
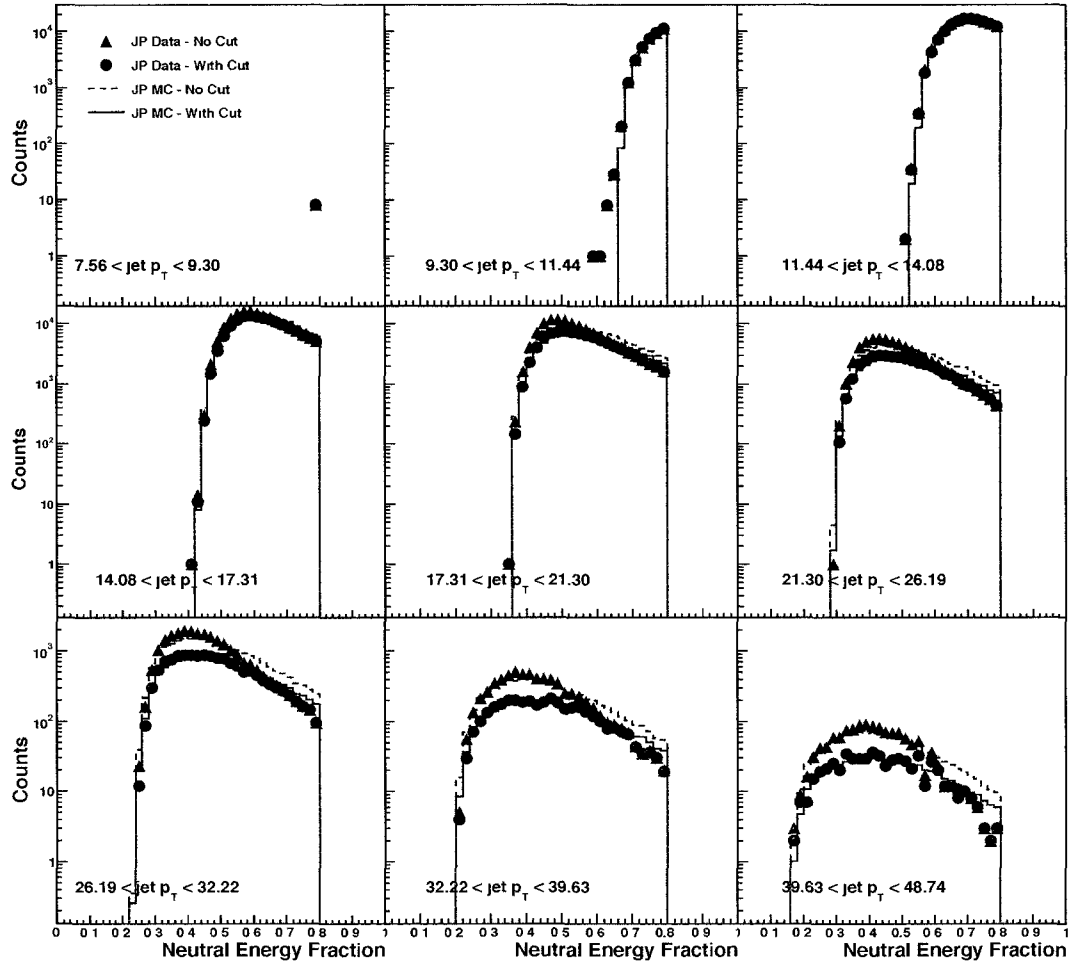
Figure 4.10: Neutral energy fraction distributions for JP data and MC with and without the energy double-counting cut. The comparison is shown for the cross section set of cuts (including a tight R_T cut) and for 9 separate p_T bins.

jets in these figures. A significant peak at $E/P \sim 1.0$ is seen in HT data that is not present in the MC. This problem is not found to be as prevalent in JP data nor for higher p_T jets regardless of the trigger.

In each of these spectra, we identify jets with a spatially associated tower and

track (shown in red) within the total distribution. To associate them we require that $|\eta_{Track} - \eta_{Tower}| < 0.03$ and that $|\phi_{Track} - \phi_{Tower}| < 0.027$ radians. By comparison, individual towers in the BEMC subtend 0.05×0.05 in $\eta \times \phi$. In our association η_{Track} is the η location of the track extrapolated to a radius within the BEMC that corresponds to the position of shower maximum.

We see a clear peak in HT data that arises from associated tower/track pairs. Because these jets are not simulated properly, we cut HT/HTTP jets in the A_{LL} analysis with an associated track/tower pair, track $p_T > 1.5$ GeV/c, tower $E_T > 2.0$ GeV, and $E/P < 1.2$. Some of the cut HT/HTTP jets nonetheless pass JP-trigger requirements and so still make it into the data and MC samples. However, the overall data/MC agreement is much better. After all other cuts are made, applying this cut on 'electron-like' events removes an additional 2% of the total OR-sum jets sample (see Table 4.1).

We conservatively remove these 'electron-like' jets from both the HT and JP samples in the cross section analysis. Fig. 4.9(4.10) shows MC/data comparisons of the HT(JP) neutral energy fraction distributions for 9 p_T bins with and without cutting these jets. We use the tighter cross section cuts in these figures, including the neutral energy fraction cut $0.05 < R_T < 0.80$, and we normalize each p_T-bin MC sample to the number of data counts in that bin. HT data shows a large peak just below $R_T \sim 0.5$ that is not present in HT MC. This peak arises from these double-counting jets, and is not as common nor as likely in JP data. However, in examining Fig. 4.10, it is clear that a slight peak just below $R_T \sim 0.5$ causes an overall discrepancy between data/MC, and the MC replicates the data better when these jets are removed.

4.9 Pile-up Contamination

At STAR there is a beam crossing every ~ 106 ns. Ionization electrons in the TPC, by comparison, can take up to ~ 39 μs to drift to the readouts. Therefore, tracks originating from hard proton-proton scatterings of nearby bunch crossings can contaminate the event of interest and can contribute to reconstructed jets. Additionally, multiple beam interactions per bunch crossing can also deposit energy in the calorimeters within the jet cone radii. We estimate the contamination of this pile-up energy in jets by remeasuring the jet energy after embedding reconstructed jets into zero-bias (ZB) triggered data.

The ZB trigger condition requires none of the normal BBC or BEMC selection criteria. ZB-triggered data is interspersed with triggered events during each normal run. We measure the mean number and energy of tracks and towers that land within the embedded jet's cone. Tracks and towers in the ZB event must pass the same criteria we require in normal jet-finding to be considered. On average 34.6 MeV from tracks and 12.4(2.5) MeV from BEMC(EEMC) towers fall within the cone. We correct the jets in our data sample by 50 MeV, the sum of all these contributions.

4.10 Number of Jets

Table 4.1 lists the number of jets surviving each cut for both analyses and each trigger scenario. An additional cut not discussed above restricts the active jet p_T window to 5.0 GeV/c $< p_T <$ 48.74 GeV/c in the A_{LL} analysis and 9.03 GeV/c $< p_T <$ 59.96 GeV/c in the cross section analysis.

Cut	Asymmetry	Cross Section	
	JP || HT || HTTP	JP	HT
No Cuts	9.48 M (100%)	4.46 M (100%)	1.06 M (100%)
Vertex Found	9.03 M (95%)	4.31 M (97%)	1.01 M (96%)
$|zVertex| \leq 60.0$	—	2.80 M (63%)	689 k (65%)
$6 \leq BBC \leq 9$	7.43 M (78%)	2.63 M (59%)	649 k (61%)
Spin Pattern	7.42 M (78%)	—	—
Software Trigger	4.33 M (46%)	1.14 M (26%)	329 k (31%)
$-0.7 \leq \eta \leq 0.9$	3.68 M (39%)	—	—
$-0.8 \leq \eta \leq 0.8$	—	959 k (22%)	255 k (24%)
$R_T \leq 0.92$	2.93 M (31%)	—	—
$R_T \leq 0.80, \geq 0.05$	—	643 k (14%)	129 k (12%)
electron-like Jets	2.74 M (29%)	534 k (12%)	101 k (10%)

Table 4.1: The number of jets passing each cut (with the fraction of the initial jet sample in parentheses) in both analyses presented here. A line in the box indicates that cut is not applied in that analysis.

CHAPTER 5

Cross Section Measurement

5.1 Theoretical Predictions

Inclusive jet calculations at STAR energy and kinematics have been performed
analytically within a NLO QCD framework[12]. These calculations use the most
recent set of unpolarized parton distributions, CTEQ6M[49], and include LO
and NLO contributions up to $\mathcal{O}_\alpha(3)$. Jets are defined as the sum of the four-
momentum of all partons that fall within a geometrical cone centered on the
jet axis. A 'Small Cone Approximation,' which assumes a narrow jet cone, is
used in these calculations. This approximation was previously compared with
inclusive jet data from other hadron colliders and was found to agree well[50].
An acceptance cut of $|\eta| < 0.8$ is applied in these calculations to agree with cuts
we make at the Particle and Detector levels.

The theoretical jet energy scale in these calculations differs from our exper-
imentally measured jet scale. A series of energy corrections discussed in the
subsequent sections are designed to correct our experimental jets to be as close
to theoretical jets as possible. This includes corrections to remove the resolution
and efficiency effects introduced by our detectors as well as effects arising from
the accelerated beams. Additionally, the theoretical predictions do not include
models of hadronization nor fragmentation, they are simply partons within a

cone. This discrepancy will be discussed and estimated in Sec. 5.3.5.

Renormalization and factorization scales are free parameters within the theoretical framework and are assigned the value of the jet p_T, $\mu_R = \mu_F = p_T$. As an estimate of the uncertainty in these assumptions (and in the predictions in general), we follow uncertainty limits outlined in [12] and vary both of these scales up and down by a factor of 2. This yields a variation in the cross section predictions and is included as a theoretical uncertainty in our final comparisons.

5.2   Luminosity Determination

The inclusive jet cross section can be written generically as the ratio of the number of jets divided by the beam luminosity, $\sigma = N_{jets}/\mathcal{L}$. The number of jets is measured in data using STAR's calorimetry and tracking detectors and corrected with a series of MC-derived corrections that will be discussed in subsequent sections. The beam luminosity, on the other hand, is measured by the BBC and MB trigger:

$$\mathcal{L} = \frac{N_{MB}}{\sigma_{BBC}} \tag{5.1}$$

where σ_{BBC} has been previously measured[32] at STAR and N_{MB} is the number of MB events registered during the runs and events used in this analysis.

In relatively high-luminosity running conditions, like those of RHIC during 2006, there are two corrections to the measured N_{MB} that must be considered. Each BBC detector operates by counting hits within a finite TAC window. There is the possibility that multiple coincidences occur within a single time window resulting in MB trigger depletion. On the other hand, as the luminosity increases there is a greater probability of accidental coincidences being counted as true

MB trigger events and, thus, interpreted as true hard scatterings. Both effects pull the overall luminosity in opposite directions and are estimated following a prescription devised first at the Tevatron[51]. A small multiplicative correction to N_{MB}, measured to be 0.99857 over all data included in the analysis, demonstrates that our MB trigger slightly over-counts hard scattering events. This is a small effect but is included for completeness and will be a much larger correction as luminosity increases in future RHIC runs.

5.3 Methodology

In practice, the inclusive jet differential cross section is defined as

$$
\frac{d^3\sigma}{d\phi d\eta dp_T} = \frac{1}{2\pi\,\Delta\eta\,\Delta p_T}\frac{\sigma_{BBC}}{N_{MB}}\frac{N_{jets}(p_T)}{c_{factor}(p_T)}
\tag{5.2}
$$

where we have already assumed full 2π-azimuthal coverage. The ratio σ_{BBC}/N_{MB} forms the luminosity term as described in Sec. 5.2, $\Delta\eta = 1.6$ using the psuedorapidity range $|\eta| < 0.8$, and Δp_T is bin dependent. Correction factors, $c_{factor}(p_T)$, are formed for each p_T bin from the ratio of Detector and Particle jet yields (see Sec. 5.3.4). The yields, $N_{jets}(p_T)$, and correction factors in Eq. 5.2 are calculated separately for the HT and JP triggers, leading to two final measurements of the cross section.

As mentioned in Sec. 5.1, we make a series of corrections to our measured jets to account for the difference between our jet momentum scale and the theoretical jet momentum scale. We first correct each jet for pile-up energy that enters the jet cone from additional proton scatterings. Next, we correct each jet for energy lost due to detector inefficiencies. The average energy lost for each measured jet p_T is estimated using MC. We then calculate the correction factors. These

factors account for bin-to-bin jet migrations that arise from resolution effects and also correct the jet p_T scale to Particle-level, one step closer to theory. Finally, we account for energy spilling into and out of our cone via hadronization and underlying event effects. These effects are included in our MC but not in the theoretical calculations. Each of these listed corrections is discussed in detail in a separate section below.

5.3.1 Pile-up Correction

Collecting data in a high-luminosity environment causes pile-up energy not associated with the hard scattering of interest to fall within our reconstructed jets. Our method of estimating this contamination is discussed in detail in Sec. 4.9. We embed reconstructed jets into ZB-triggered events, which require a bunch crossing but no other trigger conditions, and recalculate the jet energy to account for tracks and towers that fall in the jet cone. Despite the relatively high luminosities during 2006, this effect was measured to be relatively small, an average of ~ 50 MeV/c per jet. We subtract a flat 50 MeV/c from every jet's p_T to account for this.

5.3.2 Missing Energy Correction

Corrections are applied on a jet-by-jet basis to both data jets and Geant MC jets in order to correct for energy not measured at STAR[52]. This missing energy can arise from particles not measured in the TPC or EMCs, like neutrons and K_L^0s, as well as from detector inefficiencies, like cracks between calorimeter elements. In Fig. 5.1, Particle jets are binned as a function of Detector jets (see Sec. 3.2, Particle jets are PYTHIA-level jets while Detector jets include GEANT and trigger simulation). To enter this figure, a jet must be reconstructed at both the

Particle and Detector jet levels Further, these jets must be spatially associated using the jet thrust axis measured at both levels

$$\Delta R = \sqrt{(\phi_{Det} - \phi_{Part})^2 + (\eta_{Det} - \eta_{Part})^2} \leq 0\ 3 \qquad (5\ 3)$$

The mean Detector jet p_T is calculated for each Particle jet p_T bin, and a 4th order polynomial is fit to those means No physical basis motivates the use of a 4 dimension fit, it is simply found to characterize the distributions best We individually calculate this correction for the HT and JP triggers to account for the different biases of each trigger setup Figure 5 1 shows the raw distributions with the final fits overlaid The functional form used to correct jet-by-jet the HT and JP p_T for missing energy is

$$p_T^{ME\ HT} = -4\ 65 + 1\ 508\ \ p_T - 0\ 01984\ \ (p_T)^2$$
$$+ 0\ 0003575\ \ (p_T)^3 - 2\ 024E^{-06}\ \ (p_T)^4 \qquad (5\ 4)$$

$$p_T^{ME\ JP} = -13\ 11 + 2\ 504\ \ p_T - 0\ 06051\ \ (p_T)^2$$
$$- 0\ 00113\ \ (p_T)^3 - 7\ 467E^{-06}\ \ (p_T)^4 \qquad (5\ 5)$$

5.3.3 MC Event Reweighting

After the missing energy corrections are applied to the Detector and Data jets as described above, MC events are reweighted so that the Detector and Data p_T slopes match We reweight MC events as a function of the hard partonic p_T of the scattering so that the full event is weighted This reweights both the Particle and Detector distributions and not just the Detector jet distribution A single simple two parameter exponential weighting is found to work well for both HT
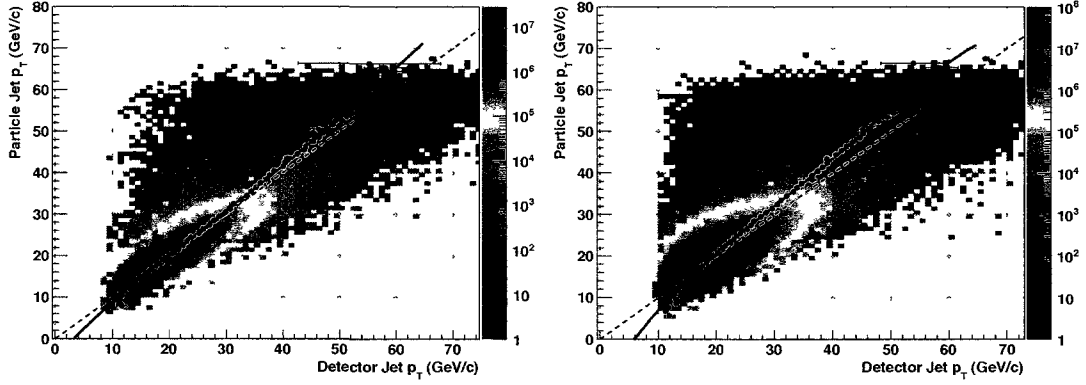
Figure 5.1: Spatially associated Particle and Detector jets for both the HT trigger (left) and the JP trigger (right). Mean Detector jet p_T is calculated for each Particle jet bin and fit with a 4th-order polynomial. Overlaid is a dashed line with slope of unity to guide the eye.

and JP comparisons, as seen in Fig. 5.2. Several iterations are required to go from left to right in the figure. The final values are shown in Eq. 5.6. After the application of this weighting, the resultant data/Detector MC ratio is found to agree well with 1.0.

In order for our unfolding correction factors (Sec. 5.3.4) to correctly account for the vertex cuts we apply, the data and MC vertex distributions must match. This requires another reweighting of the MC events, this time as a function of z-vertex. Eq. 5.7 shows the final parameter values that leads to a data/MC ratio of 1.0.

$$w_{(MC,P_T)} = w_{(MC)} \cdot \left(e^{0.0139 * p_T^{Partonic}} \right) \tag{5.6}$$

$$w_{(MC,z)} = w_{(MC)} \cdot \left(1.06 - 2.61E^{-04} \cdot z_{MC}^{Vertex} - 6.29E^{-05} \cdot \left(z_{MC}^{Vertex} \right)^2 \right) \tag{5.7}$$

In Eqs. 5.6 and 5.7, the MC events have already been weighted by the initial weighting factor w_{MC}. The full MC data is generated via 11 partonic p_T sub-samples to save computing time, and this factor is used to weight the sub-samples to one another for a smooth jet distribution. All three of these weighting factors $w_{(MC)}$, $w_{(MC,z)}$ and $w_{(MC,P_T)}$, are applied simultaneously and multiplicitively to each MC event.
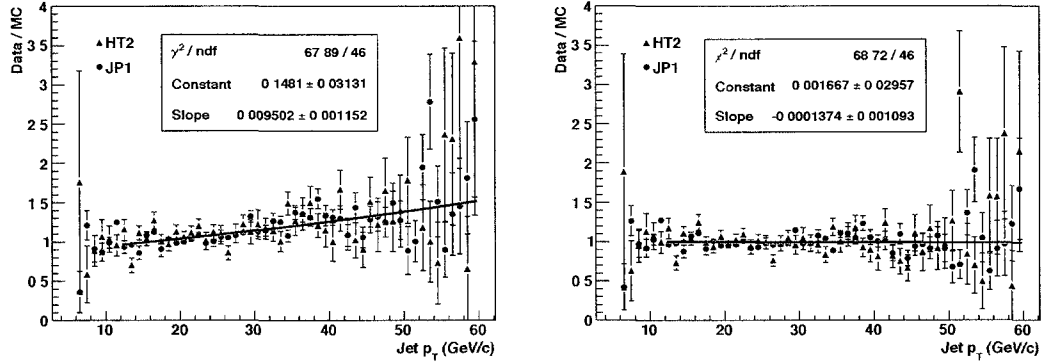
Figure 5.2: Data/Geant HT and JP p_T distribution ratios before re-weighting (left) and after (right).
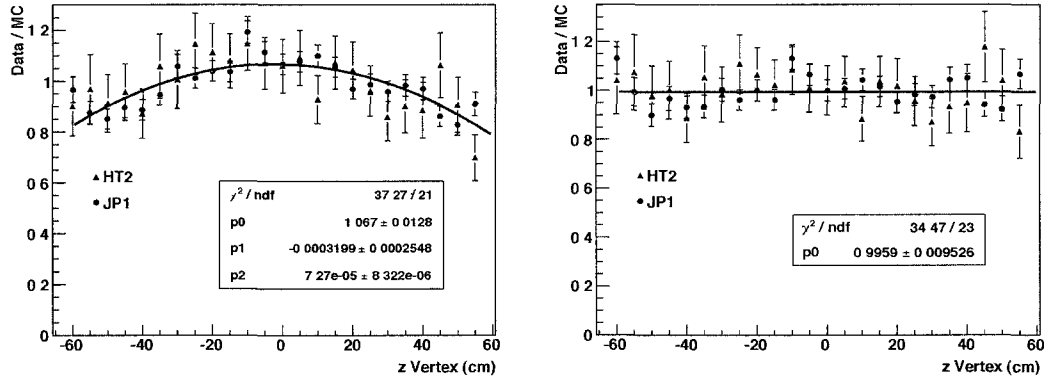
Figure 5.3: Data/Geant HT and JP z distribution ratios before re-weighting (left) and after (right).

5.3.4 Bin-by-Bin Correction Factors

To account for the difference between Detector and Particle level jets, we calculate correction factors $c_{factors}(p_T)$ for each p_T bin and trigger type. These correction factors are formed from the ratio of the Detector and Particle jet yields found in each p_T bin i:

$$c_{factor}(p_{T,i}) = \frac{N_{jets}^{DET}(p_{T,i})}{N_{jets}^{PART}(p_{T,i})} \tag{5.8}$$

These correction factors account for bin-by-bin jet migrations arising from detector resolutions in the EMC and TPC. As Particle jets propagate through STAR detectors, these resolutions smear the jet p_T. Our MC estimates, on average, which Particle jets land in which Detector jet bins, and our corrections factors account for this overall shift.

We apply identical acceptance and vertex cuts to the Detector and data jets. Assuming that the underlying data and MC distributions match, the efficiencies of these cuts are properly accounted for in the $c_{factors}$. Figure 5.3 shows a comparison of the MC and data vertex distributions after weighting, and Fig. 3.2 shows the η and ϕ distributions for MC and data. In all cases the agreement is very good. A slight discrepancy between data and MC vertex finding efficiencies can create an overall shift in the correction factors. In both data and MC a vertex is required for all events in this analysis. The vertex finding efficiency was studied in both HT and JP triggers, and no data/MC discrepancy was found. An acceptance cut of $|\eta| < 0.8$ is additionally applied to Particle jets, which matches the acceptance cut applied to NLO jets.

Figure 5.4 shows the measured correction factors for HT and JP triggers. At low p_T in our momentum range, a combination of a low trigger efficiency with

strict neutral energy cuts decreases the Detector to Particle ratio. At higher p_T in the figure, the correction factors rise as our trigger condition is more likely to be met. Strict cuts are imposed on Detector and data jets in this analysis to improve MC/data comparisons (see Chap. 4), and these cuts keep our correction factors mostly below 1.0.
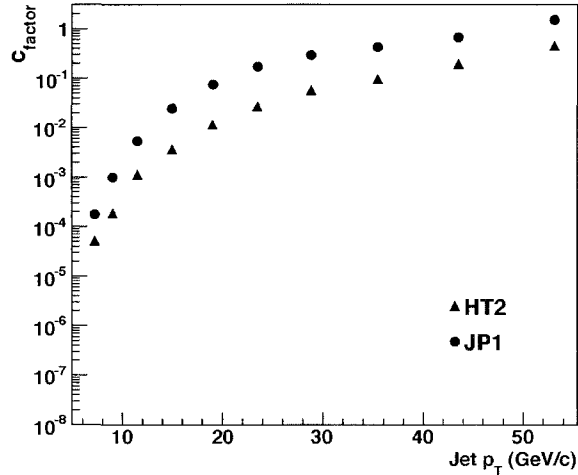
Figure 5.4: Bin-by-bin HT and JP correction factors as a function of p_T. Uncertainty bars are smaller than the symbols in this figure.

5.3.5 Hadron Fragmentation and Underlying Event Corrections

The jets presented in NLO theoretical calculations are partons scattered within a predefined cone and do not account for experimental conditions. Previous sections have presented corrections to our measured jet p_T that account for detector effects and the beam luminosity effects. Two main differences remain between these corrected experimental jets, Particle jets, and NLO jets. First, theoretical calculations do not propagate the parton decay through models of hadronization and fragmentation. Second, theoretical calculations do not account for energy

arising from underlying event interactions. These hadronization and underlying event effects must be considered for a valid data/theory comparison.

Hadronization effects remove energy from jets. Partons hadronize in Nature and the decay particles associated with a given parton can fragment out of the jet cone. On the other hand, underlying event effects add energy to the jet. Multiple parton interactions and beam remnant interactions that are not part of the hard scattering can cause energy to spill into the jet cone.

We calculate hadronization and underlying event corrections using Pythia[45]. The Pythia MC event sample used in this study is generated with the 'Tune A' parameters set[53]. Tune A specifies a series of parameters that have been adjusted to match the energy from multiple-parton interactions (MPI) measured at the Tevatron. In Pythia these MPIs can be turned or or off, as can parton hadronization and fragmentation. Further, additional beam remnant interactions can be removed from jet reconstruction by placing cuts on particle parent ID in the Pythia event record. We can then reconstruct jets from Pythia events with and without all three of these effects included and compare the spectra. Fig. 5.5 shows the the difference between the jet distribution with and without these effects as a function of Particle jet p_T. Jet spectra were fit as a function of p_T and subtracted to form this figure. At high p_T we find that more energy leaves our jet cone than spills in (hadronization effects dominate), while at low p_T the opposite is true (UE effects dominate).

Lafferty-Wyatt[54] points are calculated for each of our p_T bins. Points are then shifted to account for these hadronization and underlying event effects. Shift values are evaluated according to Fig. 5.5. The largest shifts are found for bins below ~ 18 GeV/c. Pythia is not an NLO event generator and is not the ideal tool to calculate this correction. Therefore, the final results are listed with and
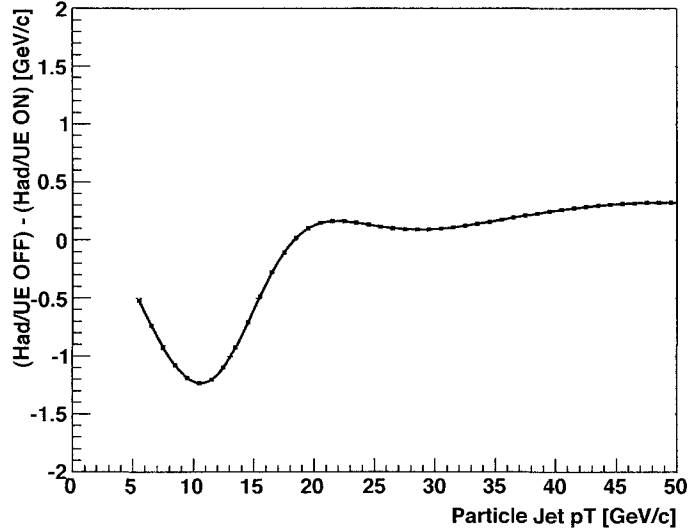
Figure 5.5: Shift values (in GeV/c) as a function of Particle jet p_T between reconstructed jet distributions with hadronization and underlying event effects and without.

without this correction should more computational advanced methods become available in the future.

5.3.6 Statistical Uncertainty

Bin widths in this analysis are chosen based on both the available statistics and the jet energy resolution. The statistical uncertainty is reported with the error bars in Fig. 5.6 and accounts for uncertainties arising from three independent measurements:

$$(\delta\sigma)^2 = (\frac{d\sigma}{dN_{jets}})^2(\delta N_{jets})^2 + (\frac{d\sigma}{dN_{MB}})^2(\delta N_{MB})^2 + (\frac{d\sigma}{dc_{factor}})^2(\delta c_{factor})^2 \quad (5.9)$$

δN_{jets} and δN_{MB} are the counting uncertainties on the jet yields and the number

of MB triggered events (respectively) in the data sample δc_{factor} is the uncertainty on the ratio of Detector and Particle jets and is included to account for our finite MC sample

5.4 Results

Cross section results for HT and JP triggers are shown in Fig 5 6 and listed in Tab 5 1 The series of corrections and cuts discussed above have been applied, and a comparison to theoretical predictions is shown Statistical uncertainties are estimated as outlined in Eq 5 9 and are represented by the error bars Systematic uncertainties, discussed in length in the next chapter, are estimated separately for JP and HT triggers but displayed in this figure as one large green band Data points are plotted at the shifted p_T values discussed in Sec 5 3 5 to account for the Hadronization and Underlying event effects not included in the theoretical predictions Good agreement is found internally between HT and JP measurements, and agreement with theoretical predictions is at the $< 10\%$ level

p_T bin (GeV/c)	LW point (GeV/c)	Shifted point (GeV/c)	$\sigma_{HT} \pm$ stat $+$ syst $-$ syst (pb)	$\sigma_{JP} \pm$ stat $+$ syst $-$ syst (pb)
11 44 - 14 08	12 60	11 52	$1\ 33 \pm 0\ 11 + 0\ 17 - 0\ 09 \times 10^{+5}$	$1\ 59 \pm 0\ 06 + 0\ 25 - 0\ 15 \times 10^{+5}$
14 08 - 17 31	15 49	15 01	$3\ 05 \pm 0\ 14 + 0\ 32 - 0\ 32 \times 10^{+4}$	$2\ 87 \pm 0\ 14 + 0\ 37 - 0\ 29 \times 10^{+4}$
17 31 - 21 30	19 04	19 11	$5\ 81 \pm 0\ 23 + 0\ 67 - 0\ 60 \times 10^{+3}$	$5\ 84 \pm 0\ 13 + 0\ 85 - 0\ 66 \times 10^{+3}$
21 30 - 26 19	23 39	23 54	$1\ 16 \pm 0\ 04 + 0\ 13 - 0\ 12 \times 10^{+3}$	$1\ 17 \pm 0\ 03 + 0\ 19 - 0\ 16 \times 10^{+3}$
26 19 - 32 22	28 73	28 82	$2\ 00 \pm 0\ 09 + 0\ 38 - 0\ 32 \times 10^{+2}$	$2\ 23 \pm 0\ 05 + 0\ 41 - 0\ 35 \times 10^{+2}$
32 22 - 39 63	35 29	35 46	$3\ 34 \pm 0\ 16 + 0\ 58 - 0\ 51 \times 10^{+1}$	$3\ 65 \pm 0\ 10 + 0\ 76 - 0\ 67 \times 10^{+1}$
39 63 - 48 74	43 26	43 56	$3\ 28 \pm 0\ 26 + 0\ 74 - 0\ 53$	$3\ 83 \pm 0\ 15 + 0\ 88 - 0\ 84$
48 74 - 59 96	52 86	53 18	$2\ 92 \pm 0\ 36 + 0\ 70 - 0\ 58 \times 10^{-1}$	$2\ 53 \pm 0\ 22 + 0\ 72 - 0\ 65 \times 10^{-1}$

Table 5 1 Lafferty-Wyatt p_T point, shifted p_T point, and final cross section results listed for each bin

79
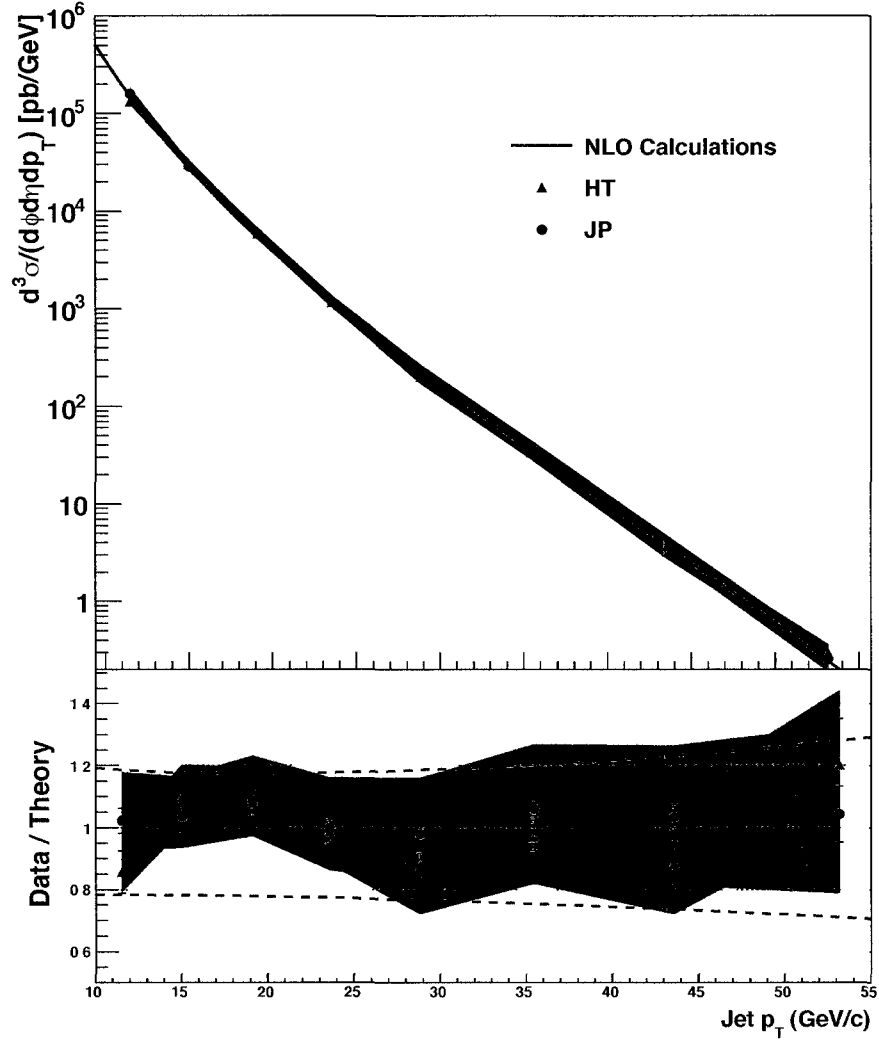
Figure 5.6: Cross Section results for both HT and JP triggers as a function of p_T. Error bars represent statistical uncertainty only. The green uncertainty band is the combined systematic uncertainty on the HT and JP points. The dashed lines represent the theoretical uncertainty from varying the renormalization and fragmentation scales up and down by a factor of 2.0.

CHAPTER 6

Cross Section Systematic Uncertainty

6.1   Jet Energy Scale Uncertainty

In the previous chapter, we describe methods used to correct each jet for detector resolution and efficiency effects. If these effects in the data are well described by MC, they do not create a systematic uncertainty. What isn't accounted for are the underlying discrepancies that exist between MC and data, as well as situations where there is a physical detector uncertainty. Uncertainties on the EMC gain calibration, on the EMC efficiency, on the measured TPC track momentum, on the track finding efficiency, and on the hadronic response of the BEMC all fall into this category and are lumped together in this section under the heading of the jet energy scale uncertainty. Each of these pieces contributes to an overall uncertainty on the p_T value we measure for each jet. Due to the steeply falling jet p_T spectrum, a small change in the measured jet p_T can create a sizable change in the yields and cross section.

Section 2.3.4 discusses the method used to calibrate individual EMC towers. Each tower is given a gain calibration coefficient, which is then used in physics measurements to translate the measured ADC values into energy. The overall uncertainties on these values was studied and found to be 1.6%. To be conservative, we round up and use 2%. Considerable effort was also made to match the

'live' fraction of the BEMC in MC and data (see Sec. 3.2). We divide up the MC sample into 4 sub-samples and each is analyzed with the mean live fraction of a matching proportion of actual data runs. While the mean live fractions match between data/MC, there could be some fluctuations in data not accounted for in MC. A conservative 2% uncertainty is included in the final systematic uncertainty to account for this.

The TPC momentum resolution uncertainty at STAR has been shown to be very small. In the case of kaons, which produce both a positive and a negative daughter track, the uncertainty was measured to be a fraction of a percent. $\pi^{\pm}$ are the most common charged particle in jets. If we take them in their most probable momentum range, $\Delta p/p$ is on the order of 2%[36]. Assuming that we are equally likely to see a π^+ as a π^- in jets, an overall systematic shift in momentum one direction is very unlikely. To be conservative, we assume the momentum resolution uncertainty is 1%, half of the $\Delta p/p$.

To evaluate how these detector uncertainties propagate through our reconstruction algorithms to form uncertainties on our measured jet distributions, we perform the same jet finding and reconstruction on tower and track objects with varied energy and momentum. In one case track momenta are varied $\pm 1.0\%$ while keeping tower hit energies constant and jets are found and reconstructed. Separately, tower energies are varied $\pm 2.0\%$ while track momenta are kept constant and jets are again found and reconstructed. In the final case, tracks are randomly removed from triggered events based on the TPC track finding efficiency uncertainty, and jets are found and reconstructed on the altered events. The uncertainty on the track finding efficiency we use is 5% (Sec. 2.3.3). Note that we cannot properly add tracks to events without introducing a potentially un-physical bias, so the effect of this efficiency on our distributions can only be

explored as a negative effect. However, the effect is assumed to be symmetrical in our final calculation.

These steps are performed on both data and MC for each of the scenarios listed above. The effect on the cross section, $(\sigma \pm \delta\sigma)/\sigma$, for each different detector uncertainty is shown in Figures 6.1 and 6.2. In Fig. 6.1 the correction factors in Eq. 5.2 are kept constant and the number of jets measured in data are varied as prescribed above. On the other hand, in Fig. 6.2 the correction factors in Eq. 5.2 are varied as prescribed above and the number of jets measured in data are kept constant. Changes to the cross section from varying data yields versus MC correction factors are similar except at low p_T in the scenario of EMC energy variation. This is due to the fact that the EMC is the triggering detector in this analysis and energy shifts can push an event above or below a trigger threshold. Trigger decisions have already been made in the data and cannot be re-evaluated as they can in MC. For this reason, we use the MC variation numbers in the final systematic uncertainties. The consistency between the two methods, namely, between varying the correction factors versus varying the data yields, gives us confidence in our final estimate.

The uncertainty in the BEMC response to charged hadrons must also be accounted for in our JES uncertainty. In a previously published STAR paper[55], it was demonstrated that there is an uncertainty on the order of $\sim 10\%$ in the data/MC comparison of the amount of neutral energy deposited by hadrons in the BEMC. 10% is a conservative estimate accounting for the typical content of our jets. It is based on their findings of a required 20% MC normalization factor for hadrons with $p < 0.5$ GeV/c and a 5% normalization factor for hadrons with $p > 0.5$ GeV/c. Additionally, the results demonstrate that charged hadrons deposit on average 20% of their momentum as neutral energy in the BEMC. After
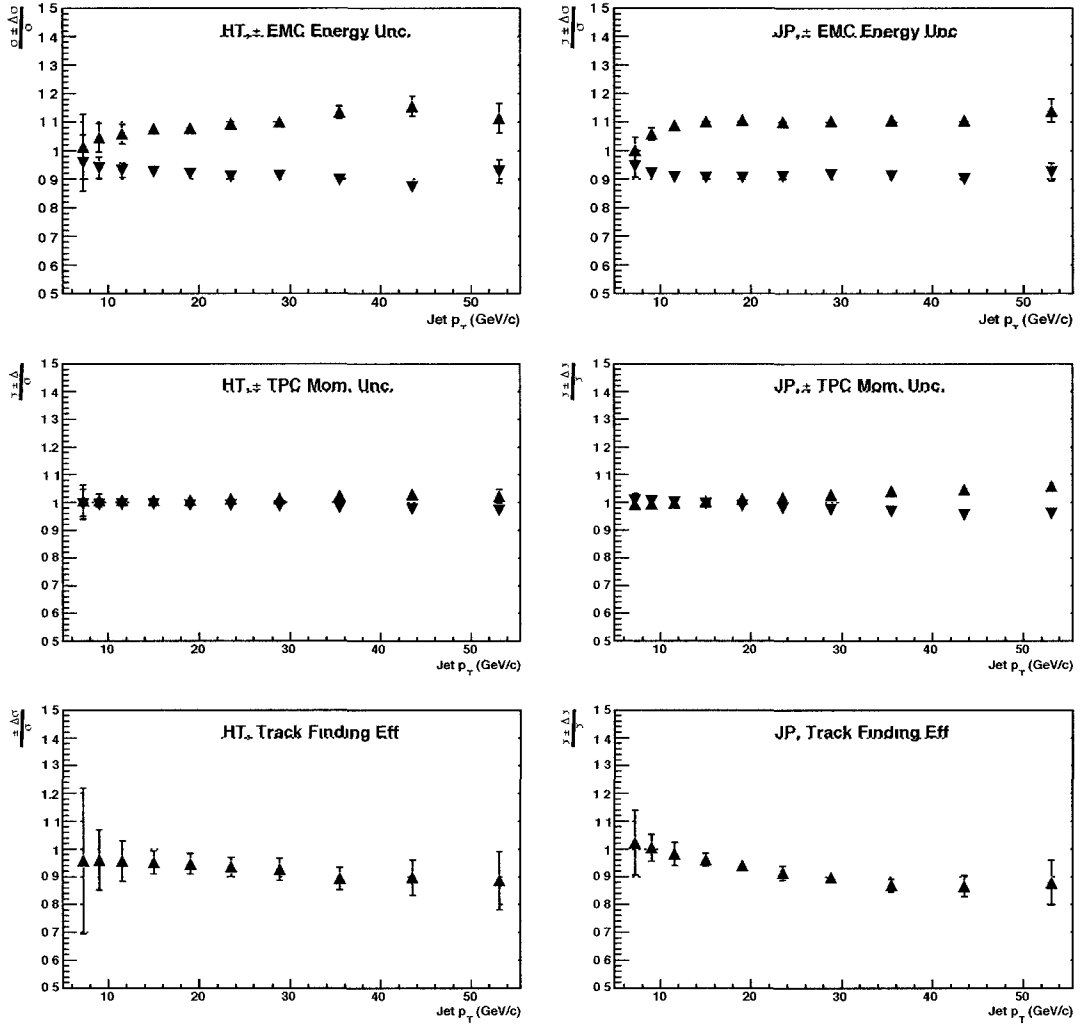
Figure 6 1   Fractional change in the cross section after varying (in data) the electromagnetic energy of tower hits ± 2 0%(top row), the momentum of tracks ± 1%(middle row), and applying a 95% tracking efficiency to the data(bottom row)   The left column is HT and the right is JP
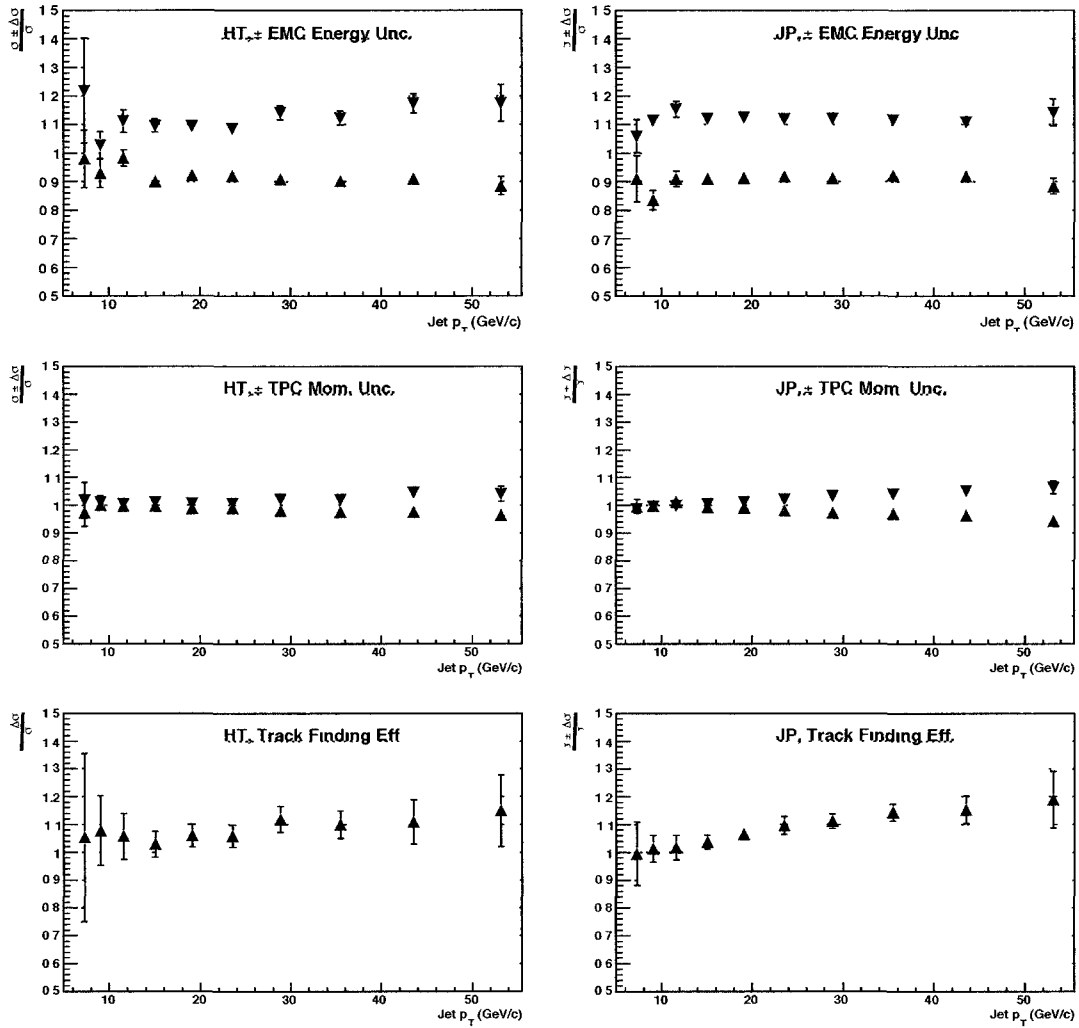
Figure 6 2 Fractional change in the cross section after varying (in MC) the electromagnetic energy of tower hits ±2 0% (top row), the momentum of tracks ±1% (middle row), and applying a 95% tracking efficiency to the Monte Carlo(bottom row) The left column is HT and the right is JP
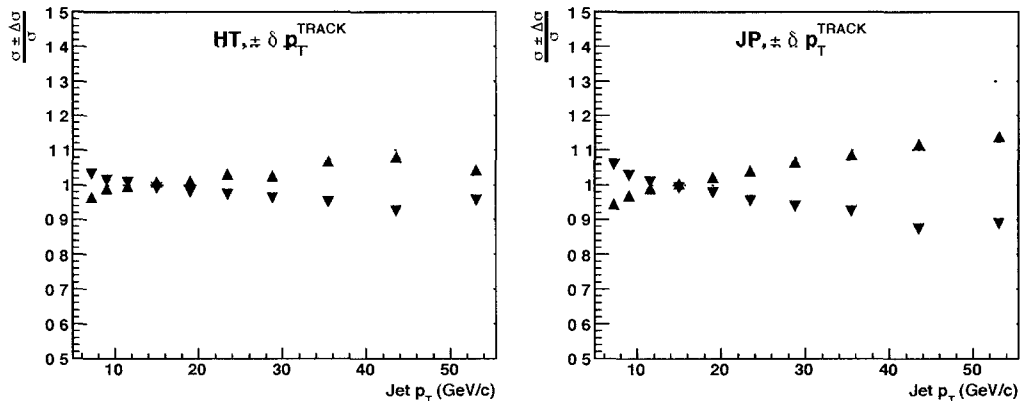
Figure 6.3: Fractional change in the cross section due to the uncertainty in BEMC response to hadrons.

including the average TPC tracking efficiency of 87%, we combine these numbers to estimate the uncertainty as $0.1 * (0.2/0.87) = 0\ 023$, or 2.3%, on the neutral energy measured in the EMC from charged hadrons. By including the 1/0.87 factor, we are accounting for the energy potentially originating from tracks not reconstructed by the TPC (and so not contributing any momentum to our jets).

This additional piece of the energy scale uncertainty is then estimated by varying the tracking momentum by ±2.3% and recalculating the jet p_T These shifted jets are then propagated through the same cross section calculations and the results are shown in Fig. 6.3.

6.2 Luminosity Uncertainty

The MB cross section is used in the luminosity determination and enters into the numerator of Eq. 5.2. σ_{BBC} has been measured previously[32] and found to be $\sigma_{BBC} = 26.1 \pm 0.2(stat.) \pm 1.8(syst)$ mb. The combined statistical and

systematic uncertainty on this value propagates to a relatively small and constant systematic uncertainty on our cross section values as shown in Fig. 6.4.
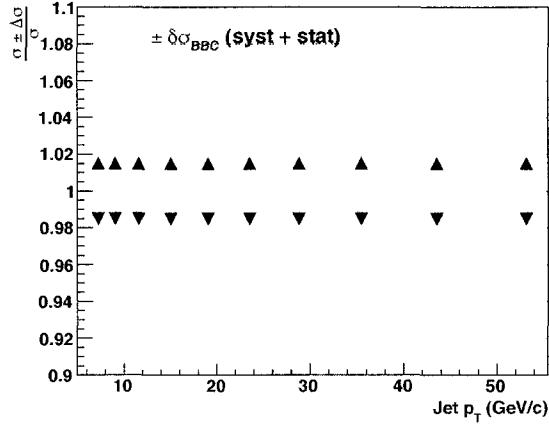
Figure 6.4: The effect of propagating the systematic and statistical uncertainty on σ_{BBC} through the HT and JP inclusive jet cross section.

6.3 Re-weighting Uncertainty

The p_T-dependent weighting used to match MC and data p_T distributions (discussed in Sec. 5.3.3) is determined by iteratively fitting the data/MC ratio with a simple two parameter exponential. In order to estimate the uncertainty introduced by this procedure, we float the final exponential weighting values up and down by the uncertainty measured on the final slope. The fit to the final data/MC distribution is found to yield a slope of -0.0001374 ± 0.001093. Correction factors are then recalculated after varying the weighting in Eq. 5.6 by ± 0.001 and the cross sections are re-evaluated. The results are shown in Fig. 6.5.

p_T bin	EMC Cal.	EMC Eff.	TPC Mom.	Track Eff.	Hadron Resp.	Reweight	Lumin.	Total
11.44 - 14.08	+11 14(-1 72)%	±2%	+0.35(-0.37)%	±5.76%	+0.70(-0.36)%	+0.32(-0.32)%	±1.5%	+12.81(-6.53)%
14.08 - 17.31	+9.55(-9.90)%	±2%	+1.12(-0.28)%	±2.96%	+0.86(-0.77)%	+0.26(-0.26)%	±1.5%	+10.40(-10.66)%
17.31 - 21.30	+9.33(-7.70)%	±2%	+0.60(-1.23)%	±6.06%	+1.14(-1.99)%	+0.11(-0.11)%	±1.5%	+11.47(-10.38)%
21.30 - 26.19	+8.47(-7.91)%	±2%	+0.56(-1.03)%	±5.87%	+3.09(-2.62)%	+0.02(-0.01)%	±1 5%	+11.06(-10.54)%
26.19 - 32 22	+14.18(-9.12)%	±2%	+2 18(-1.96)%	±11.89%	+2.56(-3 63)%	+0 24(-0.24)%	±1.5%	+18 98(-15.75)%
32.22 - 39.63	+12.22(-9.74)%	±2%	+2.00(-2.37)%	±9.93%	+6.83(-4.88)%	+0.33(-0.33)%	±1.5%	+17.46(-15.14)%
39.63 - 48.74	+17.42(-9.02)%	±2%	+4.57(-2.42)%	±10.84%	+8.06(-7.33)%	+0.68(-0.68)%	±1.5%	+22.66(-16.28)%
48.74 - 59.96	+17.46(-11.49)%	±2%	+4.07(-3.66)%	±14.95%	+4.29(-4.29)%	+1.03(-1.02)%	±1.5%	+23.88(-19.86)%

Table 6.1: Systematic uncertainties on the HT cross section measurement for each p_T bin and each effect discussed above. Uncertainties are listed in percentage ± off the measured cross section values. The final total uncertainty for each bin is the sum in quadrature.

p_T bin	EMC Cal.	EMC Eff.	TPC Mom.	Track Eff.	Hadron Resp.	Reweight	Lumin.	Total
11.44 - 14.08	+15.35(-8.92)%	±2%	+1 30(-0 08)%	±1.73%	+1.01(-0.90)%	+0.40(-0.39)	±1.5%	+15.74(-9.48)%
14.08 - 17.31	+12.04(-8.91)%	±2%	+0.40(-0.72)%	±3.72%	+0.39(-0.69)%	+0.16(-0.16)	±1.5%	+12.86(-10.02)%
17 31 - 21.30	+12.56(-8.62)%	±2%	+1 18(-0.89)%	±6.59%	+2.20(-2.07)%	+0.01(-0.01)	±1.5%	+14.62(-11.36)%
21.30 - 26.19	+11.82(-8.04)%	±2%	+2.06(-1.83)%	±9.66%	+4.10(-4.48)%	+0.21(-0.21)	±1.5%	+16.13(-13.70)%
26 19 - 32 22	+12.03(-8.82)%	±2%	+3 30(-2.66)%	±11.17%	+6.66(-6.03)%	+0.36(-0.36)	±1.5%	+18.19(-15.89)%
32.22 - 39.63	+11.57(-7.83)%	±2%	+3.93(-3 08)%	±14.42%	+8.61(-7.54)%	+0.50(-0.49)	±1.5%	+20.92(-18.49)%
39.63 - 48.74	+10.94(-8.19)%	±2%	+5 26(-3.64)%	±15 41%	+11 79(-12.59)%	+0.75(-0.74)	±1.5%	+23.04(-21.98)%
48.74 - 59.96	+14.23(-11.56)%	±2%	+6 44(-5.74)%	±19.02%	+13.95(-11.05)%	+1.24(-1.23)	±1.5%	+28.42(-25.65)%

Table 6.2: Systematic uncertainties on the JP cross section measurement for each p_T bin and each effect discussed above. Uncertainties are listed in percentage ± off the measured cross section values. The final total uncertainty for each bin is the sum in quadrature.
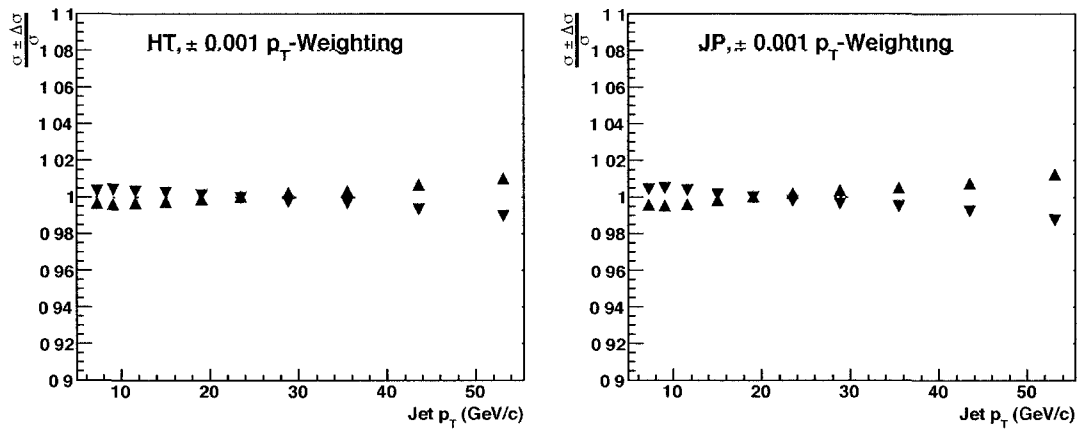
Figure 6 5   Changes to the measured cross section arising from variation in the p_T-weighting

CHAPTER 7

A_{LL} Measurement

A_{LL} is formed from the ratio of helicity dependent jet cross sections. For longitudinally polarized collisions, it is the difference between the measured cross sections from like and unlike beam-helicity states divided by the sum of the two. Experimentally, it is written in the most general form:

$$
A_{LL} = \frac{1}{P_B P_Y} \cdot \frac{(\frac{N^{++}}{L_{++}} + \frac{N^{--}}{L_{--}}) - (\frac{N^{+-}}{L_{+-}} + \frac{N^{-+}}{L_{-+}})}{(\frac{N^{++}}{L_{++}} + \frac{N^{--}}{L_{--}}) + (\frac{N^{+-}}{L_{+-}} + \frac{N^{-+}}{L_{-+}})}
\tag{7.1}
$$

This requires three concurrent measurements: the number of jets, N^{ii}, originating from each proton helicity configuration; the beam luminosities, L^{ii}, from each proton helicity configuration; and the full characterization of the proton beam polarization vectors, P_B and P_Y, including magnitude and direction. The discussion of the measurement of each of these quantities is the main objective of this thesis. Details of luminosity measurement are found in the next section. Details of the polarization vector and magnitude measurement are found in both Sec. 2.2 and 8.2, and details of the measurement of jet yields are discussed in Chap. 3.

We can simplify the calculation of Eq. 7.1 and its' associated statistical uncertainty using the following assumption:

$$\frac{N^{++}}{L_{++}} + \frac{N^{--}}{L_{--}} \approx 2 \cdot \frac{N^{++} + N^{--}}{L^{++} + L^{--}} \tag{7.2}$$

This assumption holds if the luminosity normalized yields for N^{++}/L^{++} and N^{--}/L^{--} are equal. Analogously, the unlike relations, including instead +- and -+ in Eq. 7.2, must also be equal. The proof that the luminosity normalized yields are equal is explicitly shown using data in Sec. 7.3. There we form like-sign and unlike-sign asymmetries that are evaluated to be consistent with zero within the expected statistical variation (see Eq. 7.14 and Fig. 7.3). Following these assumptions, Eq. 7.1 can be rewritten:

$$A_{LL} = \frac{1}{P_B P_Y} \cdot \frac{(N^{++} + N^{--}) - R_{LL}(N^{+-} + N^{-+})}{(N^{++} + N^{--}) + R_{LL}(N^{+-} + N^{-+})} \tag{7.3}$$

with the relative luminosity ratio R_{LL} defined as:

$$R_{LL} = \frac{L^{++} + L^{--}}{L^{+-} + L^{-+}} \tag{7.4}$$

In combining the necessary independent measurements together to form A_{LL} in Eq. 7.3, we have to account for luminosities and jet yields measured run-by-run and beam polarizations measured fill-by-fill. To properly weight each jet in the numerator and denominator of Eq. 7.3 according to the luminosity of that run and the polarization of that fill, we calculate A_{LL} explicitly as a ratio of two sums:

$$A_{LL} = \frac{\sum\limits_{nJets} P_B P_Y \cdot \left[(N^{++} + N^{--}) - R_{LL}(N^{+-} + N^{-+})\right]}{\sum\limits_{nJets} (P_B P_Y)^2 \cdot \left[(N^{++} + N^{--}) + R_{LL}(N^{+-} + N^{-+})\right]} \tag{7.5}$$

7.1 Relative Luminosity

Beam luminosity is recorded at STAR for each run and bunch crossing. Luminosity is recorded by scaler boards (see Sec. 2.3.2) that register BBC single and coincidence counts. Figure 2.6 showed the BBC coincidence counts as a function of bunch crossing for a typical run. The bunches are setup such that every run contains $\sim 25\%$ of its bunch crossings in each of the four helicity configurations. By measuring the summed luminosities for each helicity configuration in a run, we can form the various relative luminosity ratios necessary to calculate the single and double asymmetries.

To measure these asymmetries, we will need the luminosity ratio in Eq. 7.4 to measure A_{LL}, the luminosity ratios

$$R_B = \frac{L^{++} + L^{-+}}{L^{+-} + L^{--}} , \qquad R_Y = \frac{L^{++} + L^{+-}}{L^{-+} + L^{--}} \tag{7.6}$$

to measure the blue and yellow beam single spin asymmetries, respectively, and the luminosity ratios

$$R_{LS} = \frac{L^{++}}{L^{--}} , \qquad R_{US} = \frac{L^{+-}}{L^{-+}} \tag{7.7}$$

to measure the like-sign and unlike-sign double spin asymmetries. A more detailed discussion of the utility of Eqs. 7.6 and 7.7 is found in Sec. 7.3. Figure 7.1 shows these five luminosity ratios as measured for each run throughout the longitudinal data sample. Ratios fall within $\sim 10\%$ of unity. Measured values vary little run to run within a single fill, but there is some variation between fills.

We have several tools available to assess the reliability of our measured relative luminosities. We use two scaler boards to simultaneously measure and read out the BBC counts, each employing slightly different timing integrations ($\Delta t =$
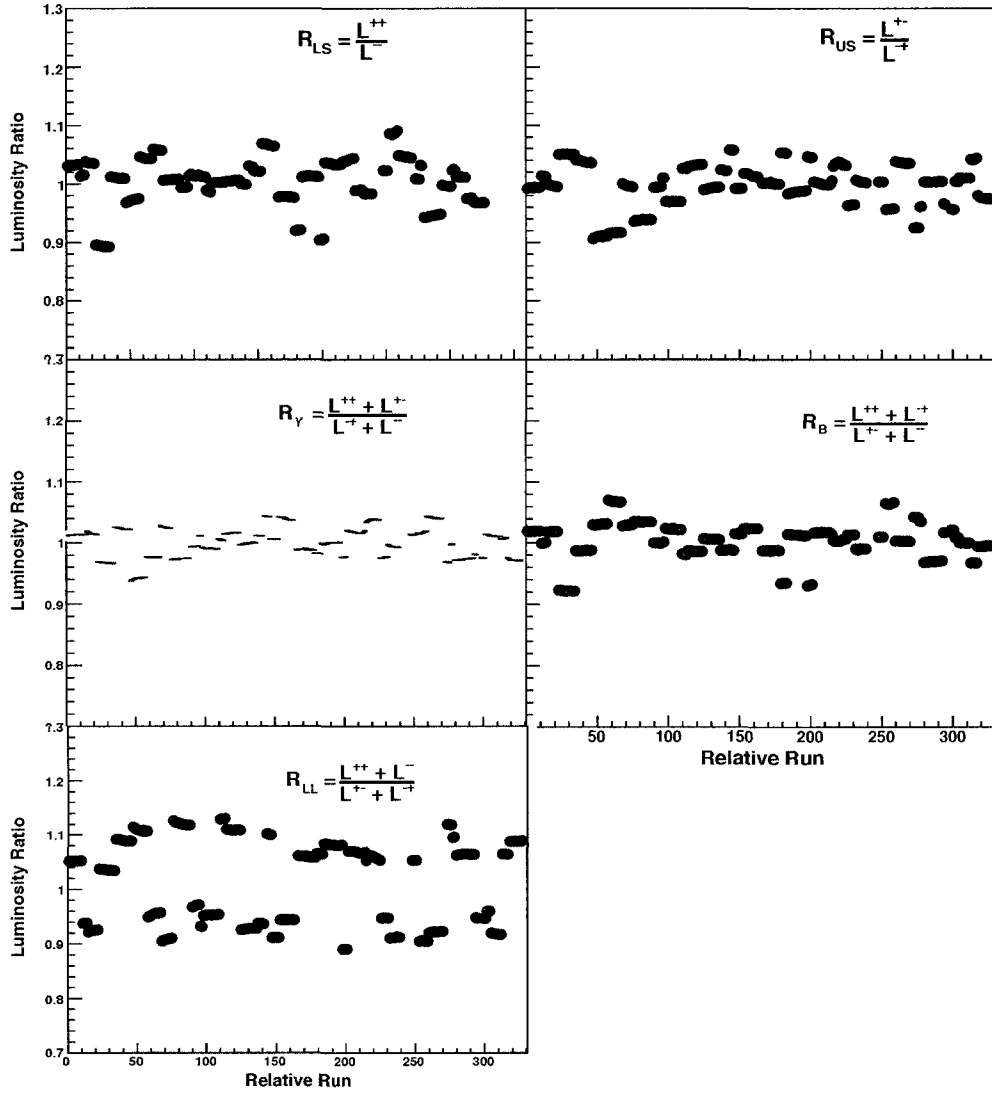
Figure 7.1: Luminosity ratios used to calculate the five asymmetries discussed in this analysis. Values presented here are plotted for individual runs.

2 min. vs. entire run). Further, the ZDC can be used as an independent luminosity measurement. Differences between separate scaler board measurements and between the BBC and ZDC counting rates are used to remove problematic fills, runs, and bunches, as well as to assign a residual systematic uncertainty (a

discussion of assigning a systematic uncertainty is presented in Sec. 8.4).

A number of quality checks are performed to remove problematic fills, runs, and bunch crossings. Each fill is first checked to ensure that spin pattern information (obtained from C-AD and CDEV) matches with the BBC coincidence data collected. The BBC coincidence count pattern for each bunch crossing can confirm that we have the correct spin pattern and abort gap information; fills that were found to be suspect were investigated and a couple were removed. After the pattern is confirmed, all events that fall within bunch crossings in the beam abort gaps for both beams are removed. Additionally, the luminosity for each bunch should follow a monotonic trend from run to run within a fill (following a similar decreasing trend as the overall luminosity). Runs that are found to deviate significantly with abnormally large or small numbers of counts are removed. These data are removed from all calculations, including relative luminosity, asymmetry, and cross section calculations.

7.2 Statistical Uncertainty

The total statistical uncertainty on A_{LL} is found from the propagation of uncertainty:

$$(\delta A_{LL})^2 = \left(\frac{\partial A_{LL}}{\partial N_T}\delta N_T\right)^2 + \left(\frac{\partial A_{LL}}{\partial P_B}\delta P_B\right)^2 + \left(\frac{\partial A_{LL}}{\partial P_Y}\delta P_Y\right)^2 \quad (7.8)$$

In arriving at 7.8 we assume that $N^{++} \approx N^{+-} \approx N^{-+} \approx N^{--}$. Therefore, the statistical uncertainty is a function of N_T, the total number of jets, regardless of beam helicity state. This approximation is accurate considering the $\sim 1\%$ asymmetry results we measure and because false asymmetries sensitive to variations in yields are statistically consistent with zero (see Sec. 7.3). The beam polariza-

tion uncertainties we use in 7.8 are calculated fill-by-fill by the CNI Polarimeter group[29].

As mentioned in the context of other discussions, we divide our data sample up into bins in p_T for our final analysis. The bin widths are chosen to balance the statistical precision of our data across the p_T range as well as to reflect the uncertainty in jet resolution ($\sim 23\%$ wide, see Fig 3.4). Statistical uncertainties are correlated among bins. For instance, a di-jet event may contain one jet that falls into one bin and a second jet that falls into another bin. Our calculation of the statistical uncertainty needs to consider this correlation. In the most general sense, for a single p_T bin q, we can decompose the total number of jets J in that bin in terms of the number of events of a given type, i.e., the number of events with i number of jets, N_i.

$$J_q = \sum_i i N_i \tag{7.9}$$

$$\delta J_q = \sum_i i \delta N_i \tag{7.10}$$

After all our cuts and data reduction, we find 2.34×10^6 mono-jet events, 8.1×10^4 di-jet events, and 294 multi-jet events (multi- refers generally to > 2) in our entire data sample. We can now expand Eqs. 7.9 and 7.10 using $i = 1, 2$, ignoring the relatively few multi-jet events.

$$J_q = N_q + 2N_{qq} + \sum_{p \neq q} N_{pq} \tag{7.11}$$

$$(\delta J_q)^2 = N_q + 4N_{qq} + \sum_{p \neq q} N_{pq} \tag{7.12}$$

96

Here, the summation runs over di-jet events containing one jet each in bin q (the bin of interest) and bin p (all other bins). We assume Poisson statistics and central limit conditions, where the variance $\sigma_{N_i}^2 = N_i$ and the covariances $\sigma_{N_i N_{ij}}^2 = 0$. Fig. 7.2 (left) shows the di-jet and mono-jet p_T distribution for all p_T bins, and gives a feel for the amount of correlation in the data. The top two p_T-ranked jets in multi-jet events have been included in this figure. Fig 7.2 (right) shows the effect of using Eq. 7.12 for the uncertainty calculation versus using uncorrelated $\sqrt{N}$ statistical uncertainty. The difference is small and only slightly increases our uncertainty in the higher p_T bins.
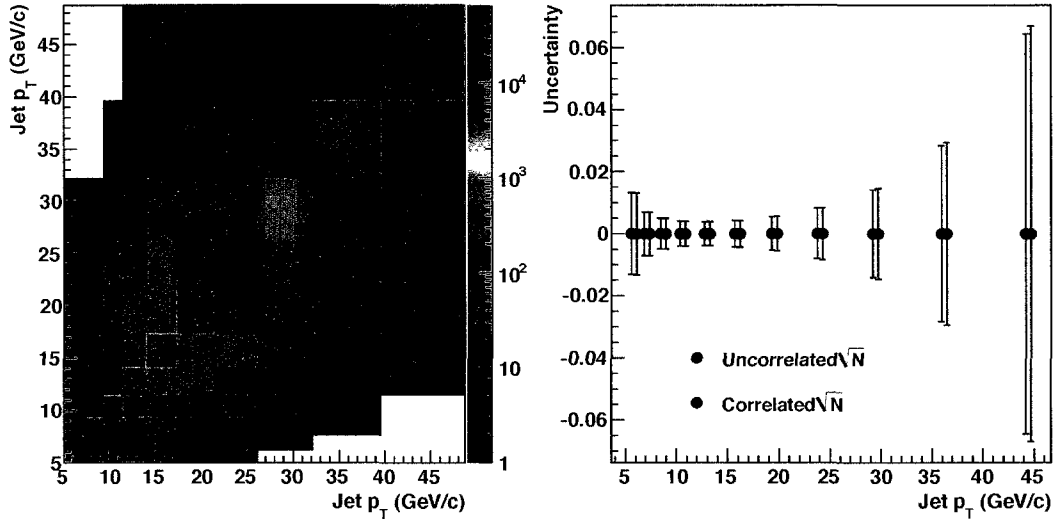
Figure 7.2: Left: Jet p_T spread for di-jet and mono-jet events. The top two p_T-ranked jets in multi-jet events are also included. Right: The uncertainty with and without the inclusion of bin-to-bin di-jet correlations.

7.3 False Asymmetries

False asymmetries in the jet data can be caused by residual detector asymmetries. These asymmetries don't arise from the hard scattering and, if found to be non-zero, have the potential to influence our measured A_{LL}. Single spin asymmetries (SSAs) in proton-proton collisions, where one longitudinal beam is polarized and the other un-polarized, violate parity and should be zero. In principle, parity violating effects could arise from the weak gauge bosons $W^{\pm}$ and Z^o, however, our collision energy of 200 GeV is too low for significant production of these particles. The SSAs for the blue and yellow beams are calculated as

$$A_L^B = \frac{1}{P_B} \cdot \frac{(N^{++} + N^{-+}) - R_B(N^{+-} + N^{--})}{(N^{++} + N^{-+}) + R_B(N^{+-} + N^{--})}$$

$$\qquad\qquad\qquad\qquad\qquad\qquad\qquad (7.13)$$

$$A_L^Y = \frac{1}{P_Y} \cdot \frac{(N^{++} + N^{+-}) - R_Y(N^{-+} + N^{--})}{(N^{++} + N^{+-}) + R_Y(N^{-+} + N^{--})}$$

In these equations we have used a convention for the jet yields that specifies the helicity ± 1 state of each beam ($N^{(Yellow,Blue)}$). As demonstrated in Eq. 7.13, we average over the polarization states of the other beam to form these SSAs for a single beam. The relative luminosities R_B and R_Y are calculated from raw BBC East-West coincidences (L^{ii}) and defined as in Eq. 7.6.

Figure 7.3 shows the SSA for both beams and each run. As a further check, it is useful to examine 'like sign' (LS) and 'un-like sign' (US) asymmetries which are also expected to be zero:

χ^2/ndf = 314 2/300
$p_0 = -0\,0008 \pm 0\,0010$

A_L^Y

χ^2/ndf = 333 0/300
$p_0 = -0\,0005 \pm 0\,001$

A_L^B

χ^2/ndf = 330 2/300
$p_0 = -0\,0005 \pm 0\,003$

A_{LL}^{LS}

χ^2/ndf = 315 1/300
$p_0 = -0\,002 \pm 0\,003$

A_{LL}^{US}

Relative Measurement
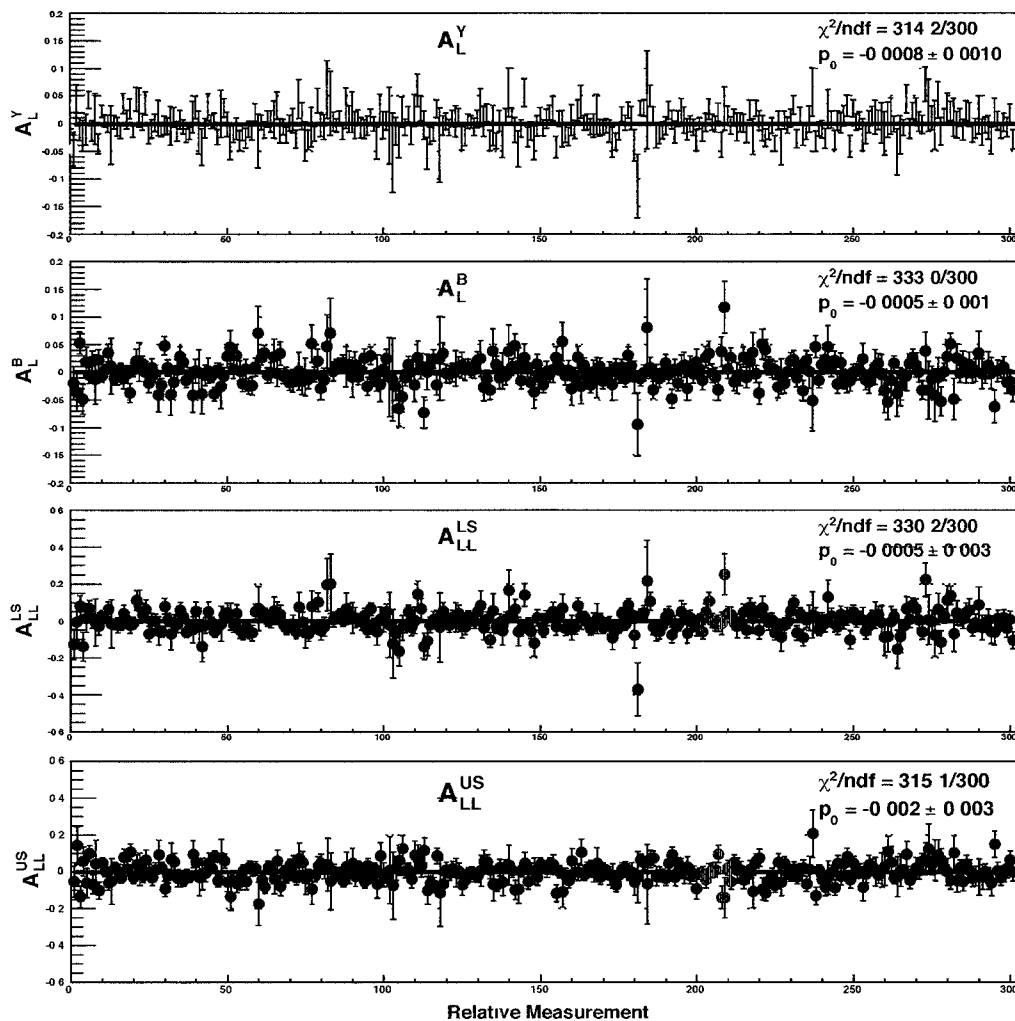
Figure 7 3 Longitudinal false asymmetries as a function of relative run number We show single spin asymmetries for the yellow and blue beams, A_L^Y and A_L^B respectively, and the like-sign and unlike-sign double spin asymmetries, A_{LL}^{LS} and A_{LL}^{US} A horizontal line fit is performed in each case, and the fit is consistent with zero within statistical fluctuations

$$A_{LL}^{LS} = \frac{1}{P_B P_Y} \cdot \frac{N^{++} - R_{LS}\, N^{--}}{N^{++} + R_{LS}\, N^{--}}$$

$$A_{LL}^{US} = \frac{1}{P_B P_Y} \cdot \frac{N^{+-} - R_{US}\, N^{-+}}{N^{+-} + R_{US}\, N^{-+}}$$

(7.14)

Relative lumonisities here are defined in Eq. 7.7, and the asymmetry results are also presented in Fig. 7.3. All asymmetries agree within 1σ of zero after a simple constant fit to each distribution as a function of relative run number.

7.4 Jet Momentum Corrections

To compare our results with theory, we need to connect the experimentally measured jet energy scale with the jet energy employed in theoretical calculations. Theoretical calculations are performed at the NLO parton level and do not account for experimental conditions arising from the accelerator, detectors, and triggers. We correct our data for these effects to make a valid comparison.

7.4.1 Pile-up Correction

Collecting data in a high-luminosity environment causes pile-up energy not associated with the hard scattering of interest to fall within our reconstructed jets. Our method of estimating this contamination is discussed in detail in Sec. 4.9. We embed reconstructed jets into ZB-triggered events, which require a bunch crossing but no other trigger conditions, and recalculate the jet energy to account for tracks and towers that fall within the jet cone. Despite the relatively high luminosities during 2006, this effect was measured to be relatively small, an average of ~ 50 MeV/c per jet. We subtract a flat 50 MeV/c from every jet's p_T

to account for this.

7.4.2 Detector and Trigger Effects Correction

Detector resolutions and inefficiencies distort our measured jet distributions from the true jet distributions. The combination of a steeply falling jet p_T spectrum and a $\sim 25\%$ jet resolution (see Fig. 3.4) means that on average we overestimate the p_T of our jets. Additionally, measured distributions at STAR are distorted because our triggers preferentially select jets with certain characteristics. For example, the High Tower trigger is most efficient for jets with a high energy leading particle, while for the same overall jet momentum, the Jet Patch trigger will fire on jets with a broader spatial distribution. Both the detector and trigger effects on jet distributions stem from the BEMC and are correlated. They are most easily calculated together.

To estimate the effect of the STAR detectors and triggers, we use Monte Carlo events generated with PYTHIA[45] passed through detector simulations created in GEANT[46]. We also employ a full emulation of the underlying logic of the HT, HTTP, and JP triggers. Particle jets (Pythia) and Detector jets (GEANT+trigger) are spatially associated using the jet thrust axis measured at both levels:

$$\Delta R = \sqrt{(\phi_{Det} - \phi_{Part})^2 + (\eta_{Det} - \eta_{Part})^2} \leq 0.3 \qquad (7.15)$$

Jets that pass this association test enter Fig. 7.4 and are used to calculate the mean Particle jet p_T value for a Detector jet p_T range. We investigated a range of association cut values around 0.3 and found little effect on the final results. We use Eqs. 7.16 and 7.17 to calculate the mean Particle jet p_T value and uncertainty

101
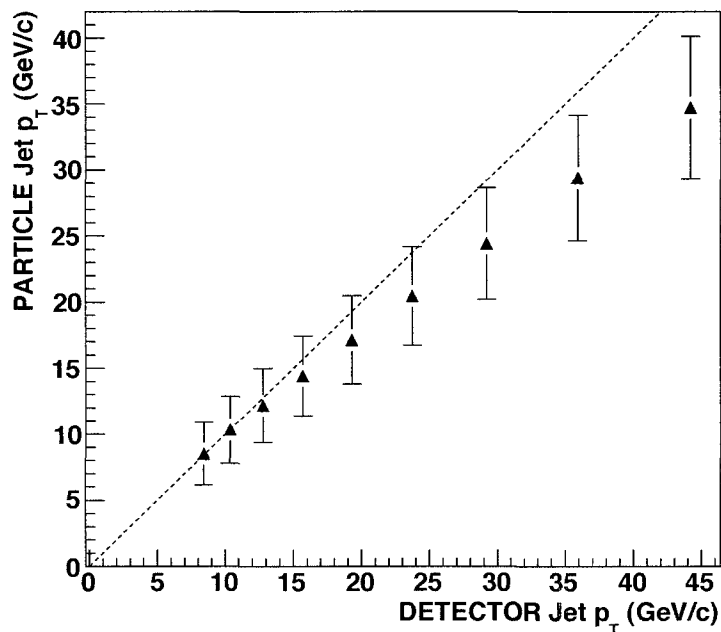
Figure 7.4: Mean Particle jet p_T for each of the Detector jet p_T bins. Uncertainty bars display the width of the distribution not the error. The dashed line is a reference slope=1 line to guide the eye.

for a single bin in Detector p_T. A complication arises from the weighting (w_{MC}) used to combine the different partonic p_T MC samples. To save computation time, MC is generated using 11 partonic p_T bins covering $3 < p_T < 65$ GeV/c. These sub-samples are later weighted by the partial cross sections and that sample's number of MC events to generate a smooth spectrum. The sub-sample specific weighting factors are labeled w_{MC}. Table 7.1 lists the final calculated Particle mean p_T values.

$$< p_T^{Part} >_{Dect.Bin} = \frac{\sum_{i=1}^{\#Jets} w_{MC,i} \cdot p_T^{Part}{}_i}{\sum_{i=1}^{\#Jets} w_{MC,i}} \qquad (7.16)$$

$$\delta < p_T^{Part} >_{Dect.Bin} = \frac{\sqrt{\sum_{i=1}^{\#Jets} w_{MC,i}^2 \cdot (p_{T_i} - < p_T^{Part} >)^2}}{\sum_{i=1}^{\#Jets} w_{MC,i}} \qquad (7.17)$$

7.4.3 Hadronic and Underlying Event Corrections

To compare our measured jets with NLO theoretical predictions, we correct our jet p_T values to account for hadronization and underlying event effects. Our method to estimate the corrections from these effects is discussed in detail in Sec. 5.3.5. Fig. 5.5 shows the p_T-shifts used to correct from Particle jet level (with Hadronization and Underlying Events effects included) to Parton jet level (without Hadronization and Underlying Events effects included). Shifted values are calculated bin-by-bin and are listed in Tab. 7.1. We propagate uncertainties on our jet distribution fits into uncertainties on our shift values. The uncertainties listed in the final column of Tab. 7.1 are the sum in quadrature of uncertainties from Particle to Detector and Had/Und. Event corrections.

7.5   Results

After all jet p_T corrections have been applied, Fig. 7.5 shows the final A_{LL} result as a function of p_T. Here, error bars are statistical uncertainty and grey bands represent the systematic uncertainty (discussed in length in the next chapter).

Detector p_T bin (GeV/c)	Particle p_T (GeV/c)	Had/UE Shifted p_T (GeV/c)
7.56 - 9.30	8.51 $\pm$ 0.27	7.43 $\pm$ 0.27
9.30 - 11.44	10.32 $\pm$ 0.18	9.10 $\pm$ 0.18
11.44 - 14.08	12.17 $\pm$ 0.15	11.03 $\pm$ 0.15
14.08 - 17.31	14.41 $\pm$ 0.11	13.68 $\pm$ 0.11
17.31 - 21.30	17.15 $\pm$ 0.08	16.99 $\pm$ 0.11
21.30 - 26.20	20.45 $\pm$ 0.05	20.60 $\pm$ 0.09
26.20 - 32.22	24.42 $\pm$ 0.05	24.55 $\pm$ 0.14
32.22 - 39.63	29.41 $\pm$ 0.10	29.50 $\pm$ 0.13
39.63 - 48.74	34.72 $\pm$ 0.15	34.88 $\pm$ 0.22

Table 7.1: Mean Particle jet p_T values (calculated with Eqs. 7.16 and 7.17) for each of the Detector jet p_T bins. Also listed are the shifted jet p_T values after the hadronization and underlying event correction. Uncertainties in the final column are the sum in quadrature from both Detector to Particle and Had/Und Event corrections.

There is an overall scale uncertainty of 8.3% from the uncertainty in the CNI polarization numbers which is not explicitly shown in the figure. Included in the figure are several theoretical predictions representative of the available models of gluon polarization. Tab. 7.2 lists the final results in detail.
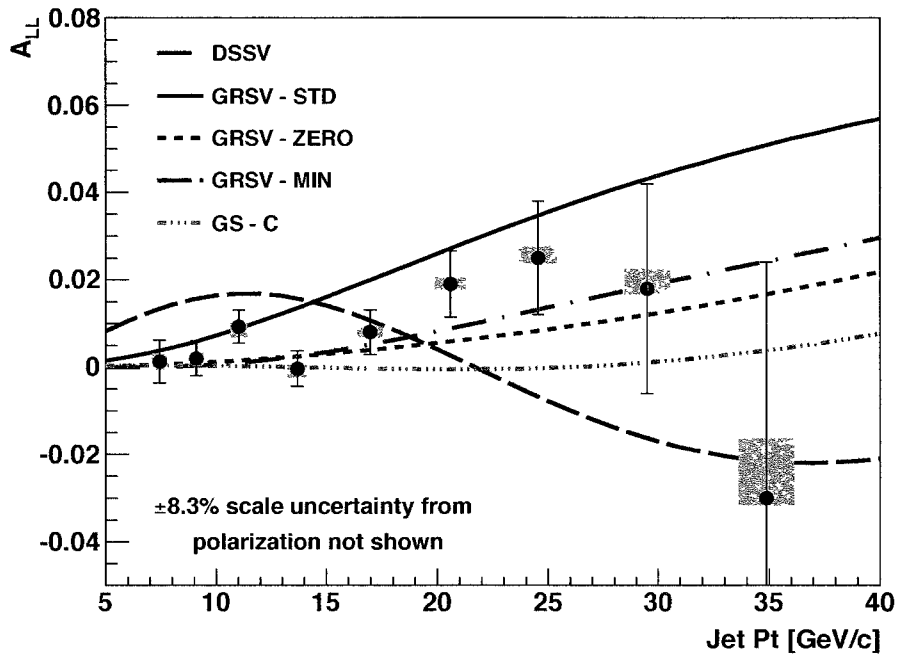
Figure 7.5: A_{LL} as a function of jet p_T. Error bars represent statistical uncertainty and grey bands represent systematic uncertainty. An 8.3% scale uncertainty from the absolute uncertainty on polarization measurements is not shown. Data is compared to several theoretical models of polarized proton structure.

Jet p_T (GeV/c)	A_{LL} ± stat + syst - syst ($\times 10^{-3}$)
7.43 ± 0.35	1.3 ± 4.9 + 1.3 - 1.5
9.10 ± 0.33	2.0 ± 4.0 + 1.2 - 1.2
11.03 ± 0.38	9.3 ± 3.8 + 1.0 - 2.4
13.68 ± 0.44	-0.30 ± 4.1 + 1.1 - 2.0
16.99 ± 0.56	8.0 ± 5.1 + 1.3 - 1.4
20.60 ± 0.69	19.0 ± 7.6 + 1.7 - 1.4
24.55 ± 0.85	25.0 ± 13.0 + 2.6 - 1.4
29.50 ± 1.04	18.0 ± 24.0 + 4.5 - 1.7
34.88 ± 1.24	-29.9 ± 53.7 +13.7 - 1.7

Table 7.2: Systematic and statistical uncertainty on A_{LL} and p_T for each bin.

CHAPTER 8

A_{LL} Systematic Uncertainties

Systematic uncertainties on the measured cross section numbers arise mainly from effects that cause a change in the jet yields On the other hand, systematic uncertainties on the measured A_{LL} numbers arise mainly from effects that cause a change in the *spin-dependent* jet yields Our measured A_{LL} numbers are only affected by an effect that acts on jet yields from one helicity configuration different than jet yields from another Therefore, the systematic uncertainties on A_{LL} are split in two uncertainties on the y-axis (A_{LL} values) and uncertainties on the x-axis (p_T point values) Effects or biases that create a spin dependent uncertainty are treated as y-axis uncertainty the trigger and reconstruction bias, the non-longitudinal beam component contamination the beam background contamination, and the uncertainty on relative luminosity calculations (Secs 8 1-8 4 below) Effects or biases that don't create a spin dependent uncertainty are treated as x-axis uncertainty the jet energy scale uncertainty, the Detector to Particle p_T shift uncertainty, and the hadronization/underlying event correction uncertainty (Sec 8 5 below)

8.1 Trigger and Reconstruction Bias

As detailed in Sec 7 4, we correct our measured jet p_T distributions to be as close as possible to the jet distributions presented by theory This includes corrections

107

for the jet resolution and detector inefficiencies as well as corrections for the biases introduced by our triggers. Differences that remain between corrected jet distributions and true jet distributions can be estimated using MC and are interpreted as a systematic uncertainty. This systematic uncertainty is the leading systematic uncertainty in our A_{LL} measurement.
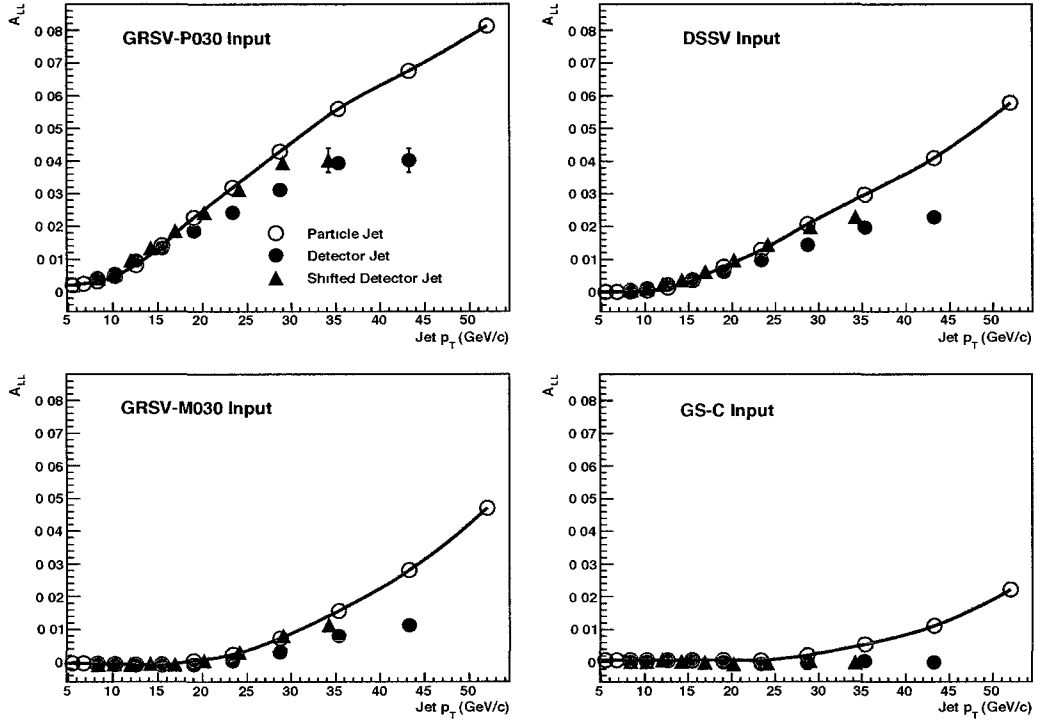
Figure 8.1: Particle, Detector, and Shifted Detector jet distributions using four representative polarized parton parameterizations.

The calculation of this trigger and reconstruction bias systematic uncertainty is further complicated by the fact that it depends on our assumptions of the relative sizes of the polarized structure functions. We don't know Nature's true polarized structure functions and theoretical guidance yields many potential models. What we do know is that the detectors and triggers at STAR bias us to
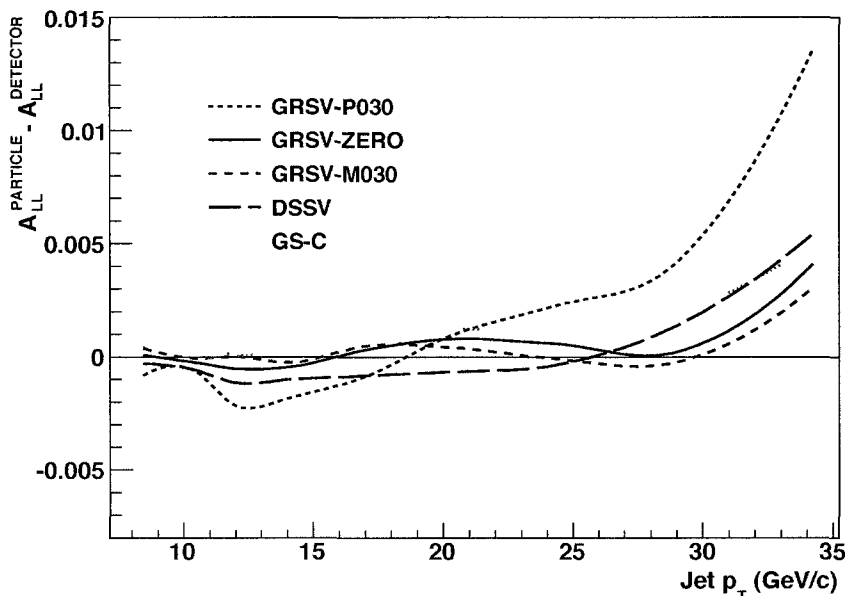
Figure 8 2 Particle A_{LL} - Shifted Detector A_{LL} vs p_T for several representative models The largest deviation (of all the models) at each p_T point is the residual trigger and reconstruction bias systematic uncertainty

particular jet characteristics due to our reliance on calorimetry in triggering and reconstruction We also know the characteristics of quark jets differ from gluon jets The combination of these two facts means we could be more sensitive to some partonic sub-processes than others

Fortunately, the unpolarized structure functions are well-determined, giving us the relative proportions of quark-quark, quark-gluon and gluon-gluon The polarized quark structure functions are also known to significantly better accuracy than the gluon To evaluate how uncertainties in the polarized gluon structure function propagate through to the trigger and reconstruction bias systematic uncertainty, we have included all available parameterizations of the proton polarized structure in the calculation Each theoretical parameterization is used to weight

109

our MC events based on x, Q^2, and partonic flavor characteristics of the event(see Sec. 3.2). Using this event weighting, we create A_{LL} predictions at the Particle and Detector jet levels. Fig. 8.1 shows A_{LL} for several polarized models analyzed at both the Particle and Detector jet levels.

The method of calculating the trigger and reconstruction bias is as follows: For a given set of polarized structure functions (eg DSSV), A_{LL} is evaluated at both the Detector level and the Particle level. The p_T positions of the Detector level jet points are then corrected ('Shifted') following the method outlined in Sec. 7.4. This correction quantifies, as best as we can, the affect our detectors and triggers have on the sample. The uncertainty due to this model is then calculated as a function of p_T as the residual difference between Particle and shifted Detector jet A_{LL}. This process is repeated for the set of models thought to represent a range of integrals not yet excluded by data. Values outside of $\pm 0.3\hbar$ (evaluated with the full integral $0 < x < 1$ at $Q^2 = 10$ GeV^2/c^2) have been effectively ruled out by DIS experiments; we include all models with gluon contributions that fall within this range. To be conservative, the maximum positive and negative uncertainty for a given p_T bin is taken from the model with the largest difference. Figure 8.2 gives the results of these calculations for a representative group of the analyzed models: GRSV ± 0.3, GRSV-ZERO, DSSV and GS-C.

8.2 Non-longitudinal Beam Component

During longitudinal data collection, beam polarization vectors at the STAR IR are not purely longitudinal. There are small non-zero vector components in the transverse and radial directions. These non-longitudinal vector components flip directions with the beam helicity flips and so have the potential to create double spin asymmetries that contaminate our A_{LL}. To measure the effect of the non-

longitudinal vector components on our asymmetries, we need to both characterize the full blue and yellow beam polarization vectors at STAR, and we need to measure the magnitude of the asymmetries produced by these components. This will give us a measure of how much the asymmetries arising from the non-longitudinal components may contribute to our measurement of A_{LL}.
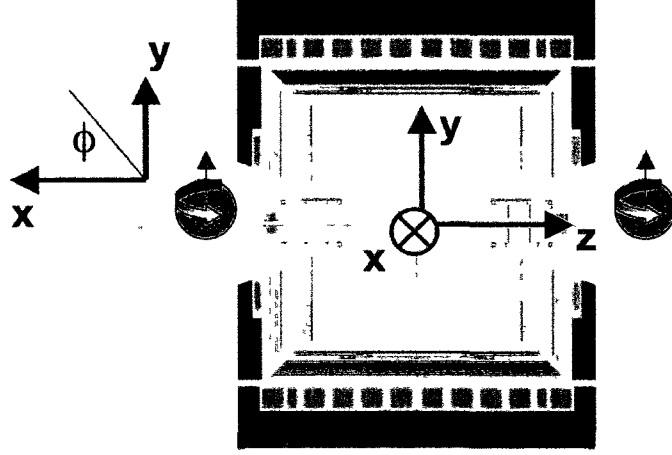
Figure 8.3: The STAR coordinate system with purely transverse beam collisions.

Given purely transverse collisions at STAR and the coordinate system defined in Fig. 8.3, the most general expression for the spin dependent yields N^τ (τ signifies the beam polarization states $++, +-, -+, or --$) is[56][57]:

$$
\begin{aligned}
N^\tau(\phi, \eta) = \mathcal{L}^\tau \cdot \sigma(\eta) \cdot [1 \ &\pm \ A_{y'}(\eta)P_B \cdot cos(\phi) \ \mp \ A_{y'}(-\eta)P_Y \cdot cos(\phi) \\
&\pm \frac{A_{y'y'} + A_{x'x'}}{2}(|\eta|)P_B P_Y \ \pm \ \frac{A_{y'y'} - A_{x'x'}}{2}(|\eta|)P_B P_Y \cdot cos(2\phi)
\end{aligned}
$$

(8.1)

Here the blue(yellow) beam points in the +(-)z direction, $\mathcal{L}^\tau$ is the spin dependent luminosity, σ is the unpolarized cross section, and A_i, $A_{i,i}$ are the relevant analyzing powers and double spin asymmetries. With purely transverse beams

and full azimuth detectors, Eq. 8.1 represents all terms allowed from symmetry arguments.

Many of the terms in Eq. 8.1 will cancel when we form a double spin ratio:

$$\frac{\sigma^{++} - \sigma^{+-}}{\sigma^{++} + \sigma^{+-}} = A_\Sigma(|\eta|)P_B P_Y + A_{TT}(|\eta|)P_B P_Y \cdot cos(2\phi) \qquad (8.2)$$

Here we've simplified the notation to match what is commonly seen in the literature using two definitions:

$$A_\Sigma = \frac{A_{x'x'} + A_{y'y'}}{2} , \quad A_{TT} = \frac{A_{x'x'} - A_{y'y'}}{2} \qquad (8.3)$$

Fortunately, during the 2006 RHIC Run we had a significant amount of transversely polarized proton collisions at STAR. This gave us a large transverse data sample to measure A_{TT} and A_Σ. The trigger and detector configurations were identical to those used in longitudinal results, and we required that all runs included from this data pass the same series of quality checks imposed on the longitudinal sample (discussed in Chap. 4). Figure 8.4 shows the measured A_Σ as a function of p_T for the transverse data. A_{TT} was also measured and agrees with zero as expected from the ϕ symmetry of STAR's detectors.

To determine the radial and transverse components of the polarization vector, we combine measurements taken using the STAR BBCs and using the CNI polarimeters. Locally at STAR, we can measure Up/Down and Left/Right asymmetries in the positive x_F direction for both the Blue and Yellow beams using the BBCs. In Sec. 2.3.1 I detailed the algorithm we use, in which raw L/R and U/D BBC asymmetries are found to be proportional to the beam polarization component perpendicular to that asymmetry. The L/R asymmetry is proportional to the vertical(transverse) beam polarization and the U/D asymmetry is
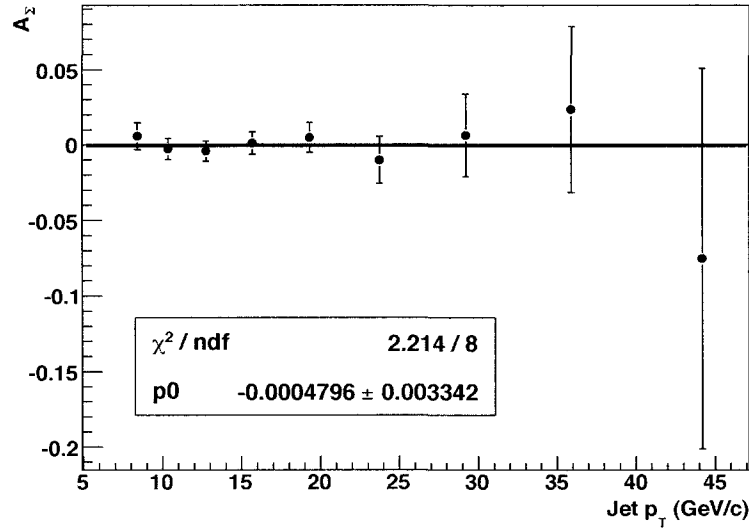
Figure 8.4: A_Σ as a function of p_T using 2006 transversely polarized proton collisions.

proportional to a horizontal(radial) beam polarization.

We calculate these asymmetries for both transverse and longitudinal data. Figure 8.5 directly shows these raw BBC asymmetries for both transverse and longitudinal data collections. Results are calculated run-by-run over the entire data collection window, though only a representative sample are shown for transverse (not the entire data sample). The longitudinal sample is further divided by a spin rotator adjustment. This was performed by collider experts to remove non-longitudinal components, and you can clearly see that both yellow and blue L/R asymmetries are closer to zero after the adjustment. The figure demonstrates the sensitivity of this method to beam direction. Further, it also shows the stability of the polarization vector as a function of time over the months of data collection. There is very little non-statistical variation outside of planned adjustments of the spin rotators. To estimate this systematic uncertainty we include data taken over
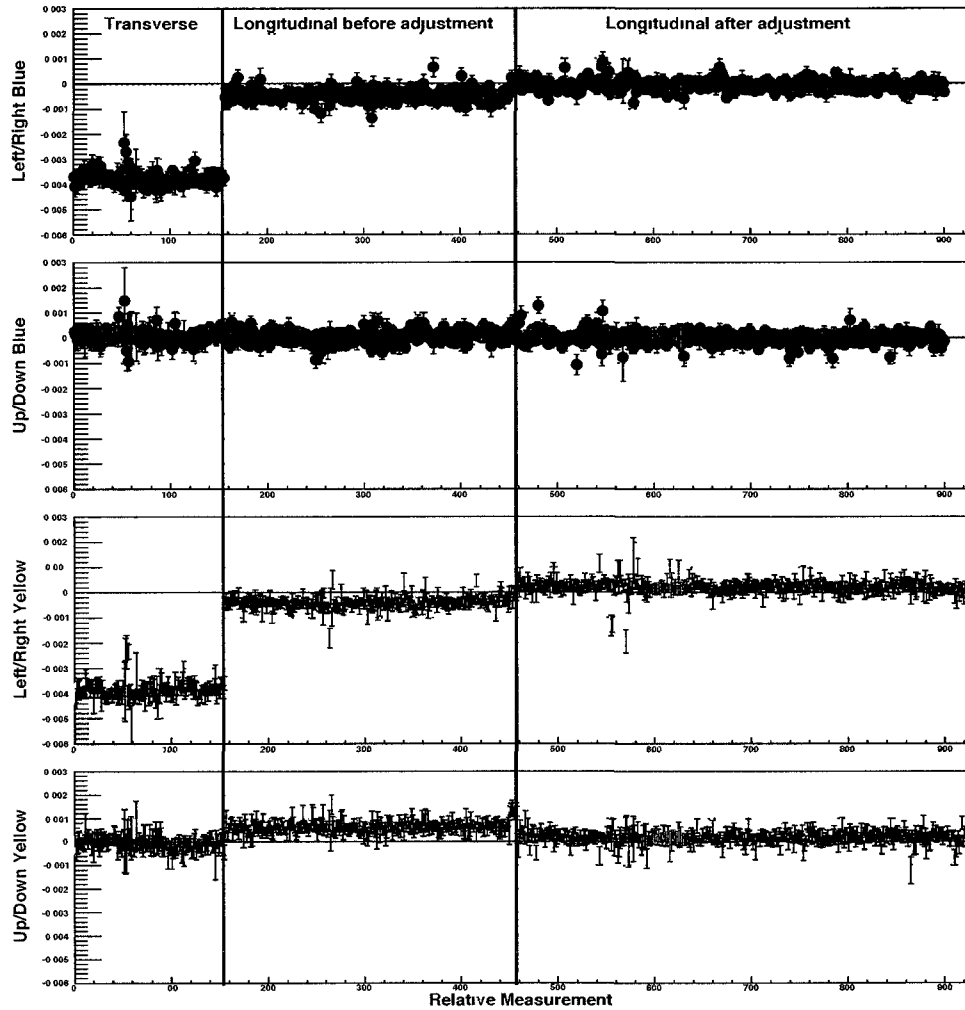
Figure 8 5 Left/right and up/down raw BBC asymmetries as a function of relative run number The data is divided into three regions pertaining to different collision types transverse, longitudinal before the spin rotators were adjusted, and longitudinal after the spin rotators were adjusted

several months to determine the polarization vector

The last piece needed to evaluate these components comes from CNI polarization measurements, which are taken with the beam direction transverse during

both longitudinal and transverse collisions at STAR. By comparing the CNI polarization numbers with our L/R asymmetry taken during transverse collisions, we normalize the magnitude of the polarization vector seen at STAR. We also measure the small non-longitudinal components when the collisions are longitudinal by taking the ratios of L/R (and U/D) to the CNI polarization measured. Between these three measurements we have enough information to fully characterize the vector and determine the blue(yellow) beam azimuthal, $\phi_B(\phi_Y)$, and polar, $\theta_B(\theta_Y)$, angles.

To determine our systematic uncertainty, we can rewrite $A_\Sigma \cdot P_B P_Y$ in Eq. 8.2 in terms of these polar and azimuthal beam angles. We find that during longitudinal running the contribution of A_Σ to A_{LL} is

$$\delta A_{LL}^{Non-Longitudinal} = |A_\Sigma \cdot tan\theta_B \cdot tan\theta_Y \cdot cos(\phi_Y - \phi_B)| \tag{8.4}$$

Conservatively assuming $cos(\phi_Y - \phi_B) = 1$, we estimate $|tan\theta_B \cdot tan\theta_Y \cdot cos(\phi_Y - \phi_B)| \sim 0.0102 \pm 0.0002$. Given A_Σ above, we calculate $\delta A_{LL}^{Non-Longitudinal}$ as a function of p_T as given in Table 8.1.

8.3 Beam Background Contamination

Particles not associated with the hard scattering of interest can deposit energy in the BEMC, trigger event storage, and reconstruct as background jets. These particles can come from beam halo particles or beam interactions with the upstream focusing magnets. As discussed in Sec. 4.7, we estimate the contribution of these jets by examining the difference in mono-jet and di-jet distributions as a function of jet neutral energy fraction (R_T). Background jets, due to our neutral energy trigger, will manifest as jets with mostly neutral energy (from the calorimeters)

$Jet\ p_T$ bin (GeV/c)	A_Σ ($\times 10^{-3}$)	δA_Σ ($\times 10^{-3}$)	$\delta A_{LL}^{Non-Longitudinal}$ ($\times 10^{-3}$)
7.56 - 9.30	5.67	8.84	0.09
9.30 - 11.44	-2.75	6.93	0.07
11.44 - 14.08	-4.17	6.67	0.07
14.08 - 17.31	0.99	7.55	0.08
17.31 - 21.30	4.86	9.99	0.10
21.30 - 26.20	-10.13	15.49	0.16
26.20 - 32.22	6.45	27.33	0.28
32.22 - 39.63	23.29	54.96	0.56
39.63 - 48.74	-75.23	125.97	1.28

Table 8.1: A_Σ, the statistical uncertainty on A_Σ, and the contribution to A_{LL} from A_Σ listed as a function of jet p_T.

and little tracking energy (from the TPC). Because these jets are not caused by a hard scattering, they also are usually contained in mono-jet events. It is very unlikely two background jets will be found in a single event. Seen in Fig. 8.6 are the distributions of mono- and di-jets for each p_T bin used in this analysis.

We determine the relative contamination of each of our p_T-bin data samples with the following method. First, we fit the ratio of the number of mono-jets/di-jets with an assumed functional form:

$$f(x) = a \cdot b + c \cdot x + a(1 - b)e^{-\alpha \cdot x} \qquad (8.5)$$

Here x is the relative charged jet energy fraction $(1 - R_T)$, and a, b, c, and α are fit parameters. The charged jet energy fraction was chosen in this formula instead of the neutral energy fraction simply for ease of fitting. Equation 8.5 is specifically designed to include a linear term $(a \cdot b + c \cdot x)$, representing the signal contribution, and an exponential term $(a(1 - b)e^{-\alpha \cdot x})$, representing the background contribution. Signal and background contributions are correlated, and the a, b, and c parameter placements in Eq. 8.5 reflect this. The α parameter was measured in each p_T bin and found to fluctuate only very slightly (within statistical variations). Therefore, it was set to a single value by determining the mean value over the whole p_T range (with each α normalized by the lower edge of particular p_T bin). Using the OR-sum trigger conditions, α is found to be 1.43 ± 0.03.

After fixing α we refit the ratio distributions, the results of which are shown in Fig. 8.7. We can now use these fits, along with the separate contributions from signal and background discussed above, to extract the fraction of signal jets under the background region (f_S) and the fraction of background jets under the signal region (f_B). To do this we use Eq. 8.6:
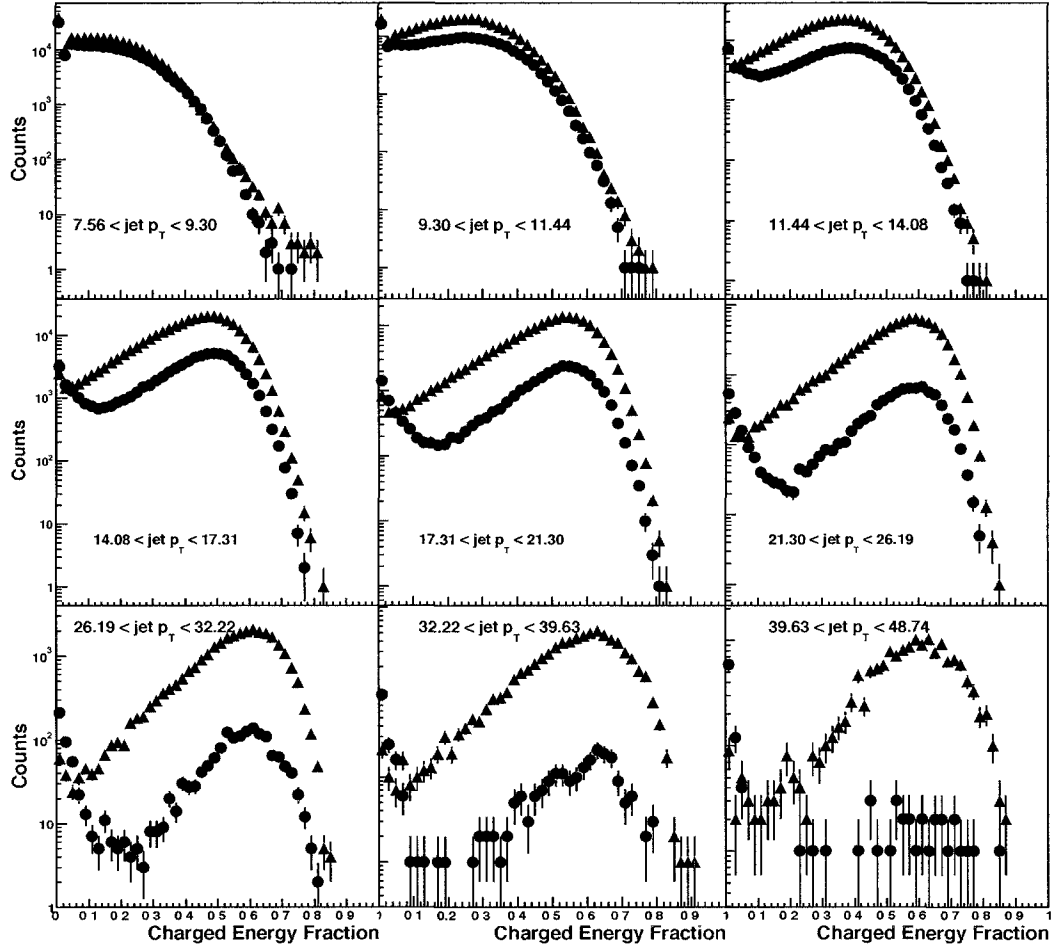
Figure 8.6: Mono-jet (blue) and Di-jet (black triangle) distributions for each p_T bin as a function of charged energy fraction.

$$f_S = \frac{\sum_i N^{mono-jets} \frac{ab+cx_i}{ab+cx_i+a(1-b)e^{-\alpha x_i}}}{\sum_i N_i^{mono-jets}}$$

(8.6)

$$f_B = \frac{\sum_i N^{mono-jets} \frac{a(1-b)e^{-\alpha x_i}}{ab+cx_i+a(1-b)e^{-\alpha x_i}}}{N_{TOT}}$$

118
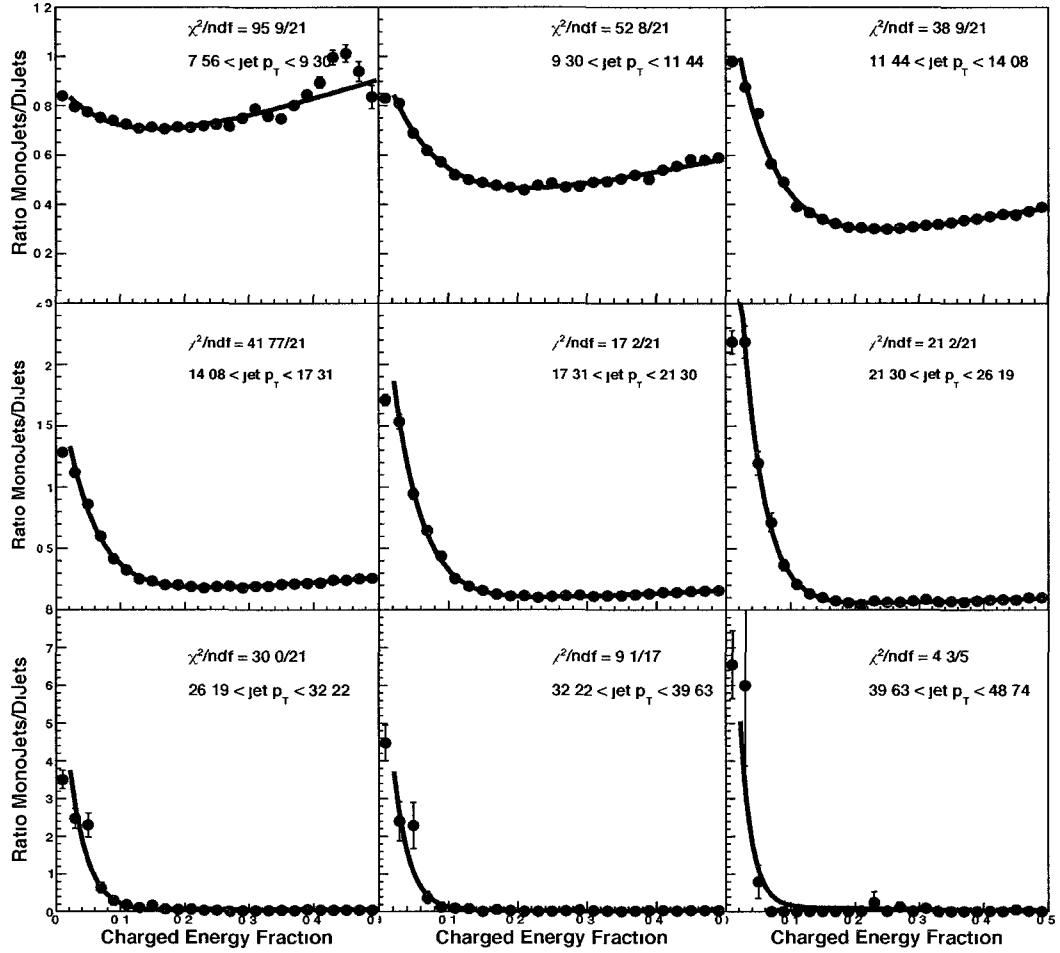
Figure 8.7: Mono-jet to di-jet ratios for all the p_T bins used in the A_{LL} analysis (note the changing y-axis scale for each row). Overlaying each distribution is the linear+exponential fit used to determine the relative contamination of background jets within that bin.

Here $x = 1 - R_T$ and each sum is taken over a different interval. The background region is defined to be $0.0 < x < 0.055$, where our spectra are dominated by background jets. The signal region, on the other hand, depends on the R_T cut value we choose. We know we want to cut out some data overrun with back-

ground, but it is not clear *a priori* what value of x to cut at. Therefore, we scan the different cut values (ranging from $x = 0.99 \rightarrow 0.7$), and the signal region is defined for each cut as the integral from the cut value up through $x = 1.0$.

f_B is needed to determine the amount of background contamination that seeps into our signal region even after we have chosen our cut; these jets will still cause a systematic bias we will evaluate below. f_S, on the other hand, is needed to determine the amount of signal contamination in our background region, where we'll be measuring the double spin asymmetry contribution from purely background jets, A_{LL}^{bkgd}. Once we have measured the signal and background fractions for a given R_T cut value, the systematic uncertainty is measured:

$$\delta A_{LL}^{bkgd} = f_B \cdot \frac{\Delta A_{LL}^{bkgd} - f_S \cdot \Delta A_{LL}^{sig}}{1 - f_S} \tag{8.7}$$

The background A_{LL}^{bkgd} is the measured A_{LL} for jets with $R_T > 0.95$ (our background region as defined above) and is shown in Fig. 8.8. To be conservative, ΔA_{LL}^{bkgd} is the larger of A_{LL}^{bkgd} or the statistical uncertainty on A_{LL}^{bkgd} (similarly for ΔA_{LL}^{sig}) in Eq. 8.7. Additionally, we inflate the uncertainty to be conservative by changing $'-'$ to $'+'$ in the numerator of Eq. 8.7 for our final estimation.

For each R_T cut value and p_T-bin, we calculate the statistical uncertainty, the beam-background systematic uncertainty, and the sum in quadrature of the two. The results are shown in Fig. 8.9. The final cut value is chosen from the minimimum of the quadrature sum. We find that there is a clear minimum in most p_T bins at $x = 0.08(R_T = 0.92)$. The resulting uncertainties after applying this cut value are listed in Tab. 8.2.

$Jet\ p_T$ (GeV/c)	δA_{LL}^{bkgd} ($\times 10^{-3}$)	$\sqrt{(\delta A_{LL}^{bkgd})^2 + (\delta A_{LL}^{stat})^2}$ ($\times 10^{-3}$)
7.43	1.517	5.204
9.10	0.766	4.210
11.03	0.492	4.027
13.68	0.343	4.452
16.99	0.357	5.707
20.60	0.448	8.570
24.55	0.752	14.896
29.50	0.792	29.887
34.88	0.501	67.852

Table 8.2: The systematic uncertainty due to the beam background contamination, δA_{LL}^{bkgd}, as a function of p_T. Also listed is the quadrature sum of δA_{LL}^{bkgd} and the statistical uncertainty.
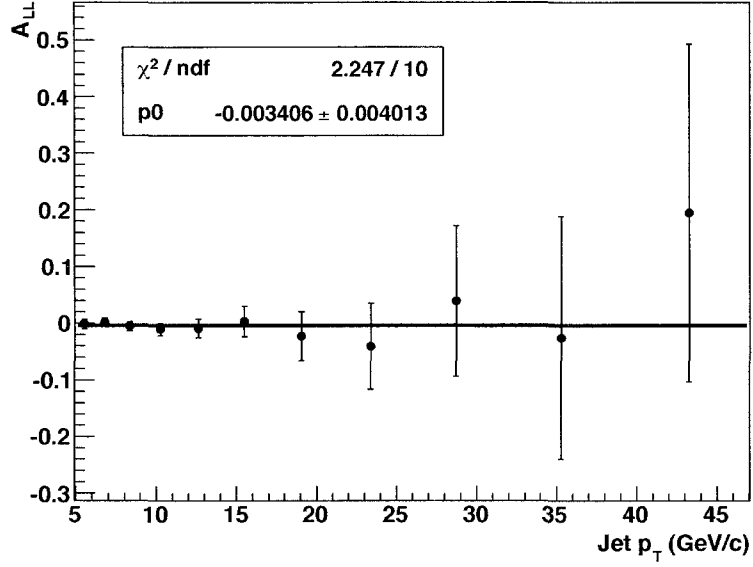
Figure 8.8: Jet A_{LL} as a function of p_T for jets with a very high neutral energy fraction $R_T > 0.95$.

8.4 Relative Luminosity Uncertainty

An uncertainty on relative luminosity, R_{LL}, translates into an uncertainty on measured A_{LL} via the simple relation:

$$\delta A_{LL} = \frac{1}{P_B P_Y} \cdot \frac{(N^{++} + N^{--}) - (R_{LL} \pm \delta R_{LL})(N^{+-} + N^{-+})}{(N^{++} + N^{--}) + (R_{LL} \pm \delta R_{LL})(N^{+-} + N^{-+})} \qquad (8.8)$$

We determine the systematic uncertainty on R_{LL} calculations by comparing calculated R_{LL} values using two independent detector systems: the BBCs and the ZDCs. Statistical precision of R_{LL} measurements with the BBCs is better than with the ZDCs because ZDCs measure neutral particles at very high rapidities, which are less likely to be produced in proton collisions (the ZDCs are primarily designed for luminosity measurements in heavy-ion collisions). R_{LL} is calculated
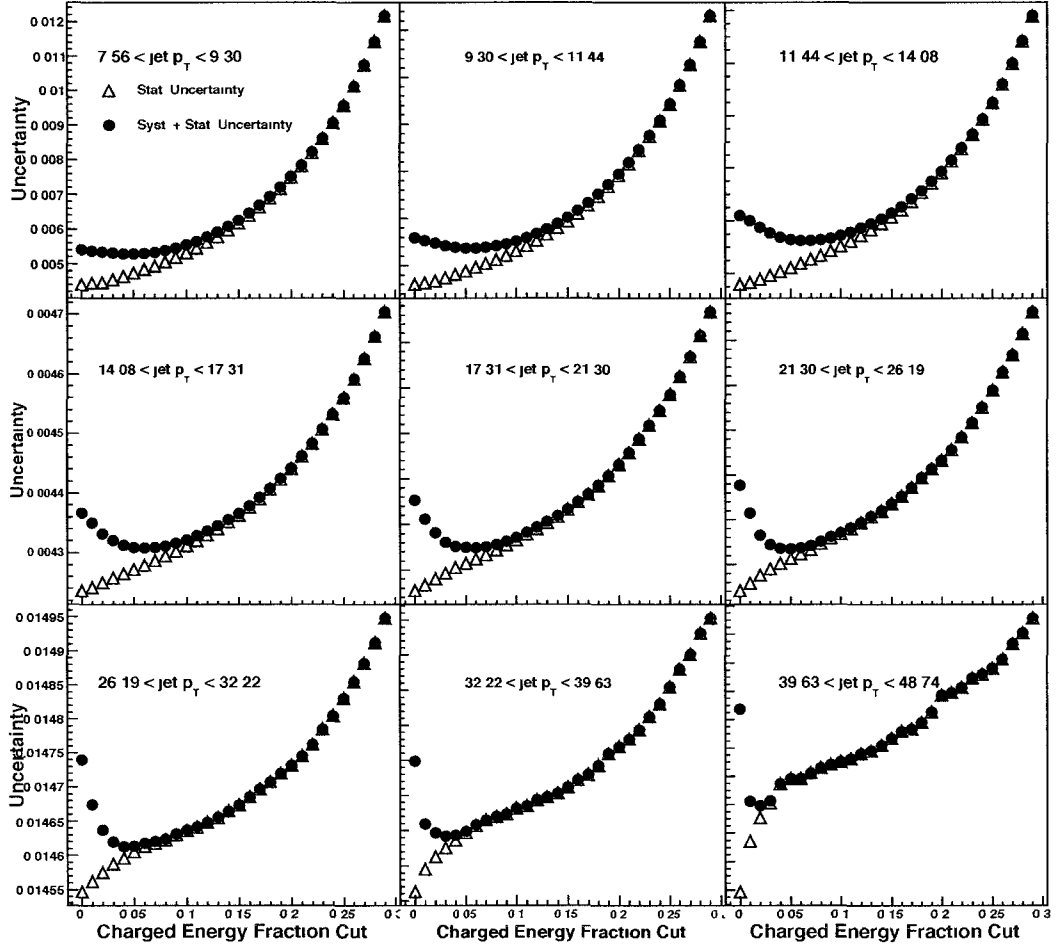
Figure 8.9: Statistical uncertainty and the quadrature sum (statistical + systematic) uncertainty as function of charged energy fraction cut. The systematic uncertainty included in this calculation is only due to the beam-gas background effect and is calculated in Eq. 8.7. Distributions are shown for each of the p_T bins used in the A_{LL} analysis. A cut value of $0.08(R_T = 0.92)$ was found to work reasonably well for each bin.

using both detectors for each run, and the average difference is found to be $\sim 9.4 \times 10^{-4}$. More details of relative luminosity analyses are presented in [58].

8.5 Jet p_T Uncertainty

Uncertainties on jet p_T values in Fig. 7.5 arise from several sources. The main uncertainty is our jet energy scale uncertainty, which is discussed in detail in Sec. 6.1. In Chap. 7 we outline a series of MC-based corrections we apply to jet p_T that account for detector resolution and efficiency effects. Uncertainties in our final jet p_T estimates remain, however, from underlying discrepancies that exist between our MC and data. Uncertainties on the EMC gain calibration, the EMC efficiency, the measured TPC track momentum, the track finding efficiency, and the hadronic response of the BEMC all fall into this category and are lumped together under the heading of jet energy scale uncertainty. In the cross section measurement, these uncertainties were treated as an uncertainty in the final cross section numbers. In the case of the A_{LL} measurement, defined as a ratio of cross sections, this uncertainty is instead treated as a x-axis uncertainty, an uncertainty where the p_T points are placed.

To calculate this uncertainty we use the BEMC energy and TPC momentum uncertainties from Sec. 6.1 (2.8% and 5.6% individually). In each p_T bin i, we find the fraction of the jet 4-momentum from the EMC and the fraction from the TPC, $R_{T,i}$ and $f_{TPC,i}$ respectively. The total uncertainty is then estimated for each bin:

$$\delta p_T^{JES,i} = \sqrt{(0.028 \cdot R_{T,i})^2 + (0.056 \cdot f_{TPC,i})^2} \tag{8.9}$$

Results are listed in Tab. 8.3

In addition to the uncertainty in the jet energy scale, p_T-corrections carry uncertainties from the Detector to Particle (Sec. 7.4.2) and hadronization/underlying event (Sec. 7.4.3) shifts. The Detector to Particle correction is estimated using a

finite MC sample and, therefore, has a 'statistical' uncertainty attached to it. The hadronization and underlying event correction relies on fits to jet distributions and, therefore, has an uncertainty due to the goodness of these fits. The uncertainty due to corrections to jet p_T (Detector to Particle + Had/Und. Event), the uncertainty from the jet energy scale uncertainty, and the sum in quadrature is listed in Tab. 8.3.

p_T Value (GeV/c)	δp_T^{JES} (GeV/c)	δp_T^{CORR} (GeV/c)	Total (GeV/c)
7.43	±0.23	± 0.27	± 0.35
9.10	±0.28	± 0.18	± 0.33
11.03	±0.35	± 0.15	± 0.38
13.68	±0.43	± 0.11	± 0.44
16.99	±0.55	± 0.11	± 0.56
20.60	±0.68	± 0.09	± 0.69
24.55	±0.83	± 0.14	± 0.84
29.50	±1.02	± 0.13	± 1.04
34.88	±1.22	± 0.22	± 1.24

Table 8.3: Uncertainties on jet p_T.

CHAPTER 9

Discussion

In Sec. 1.2 we discussed why many scientists believed there was a large gluon spin contribution to the proton. Measurements of the g_1 structure function (Eq. 1.5), which depends directly on the quark/anti-quark spin contribution, were much lower than expected by the naive parton model. When a full QCD treatment is performed, a term proportional to Δg (Eq. 1.7) contributes to g_1 at NLO. This term adds to g_1 in such a way that a large (positive) gluon spin contribution can cancel the quark spin contribution and reconcile the predictions of a sizable quark contribution with a small measured g_1. Many scientists believed the resolution of the spin crisis lay in a large gluon spin contribution.

RHIC proton-proton collisions provide the first leading-order access to Δg through the spin asymmetries A_{LL}. Comparison of the RHIC A_{LL} results, including STAR jet results[59][60] and Phenix π^0 results[61][62], to theoretical calculations rule out large positive or negative contributions to Δg over the RHIC kinematical window. In these publications we explicitly calculate confidence levels from the comparison of our data with various Δg parameterizations. We can now say more because we have first parameterizations from a global fit that includes RHIC A_{LL} data and DIS data (DSSV[20]). DSSV uses STAR jet results from 2005 data[60] and preliminary 2006 data[59] as well as PHENIX π^o results[62]. Figure 9.1 shows the results. DSSV finds Δg to be small, even compared to previous gluon models that predicted a moderate gluon polarization. They find

a zero crossing for Δg within the RHIC x-range (shaded band). However, their model uncertainty limits, even within the shaded band, still allow a functional form of Δg that is positive, negative, or contains a node. Furthermore, at lower x, uncertainties become much larger. The results of this dissertation offer a more precise and finalized jet A_{LL} measurement than the preliminary 2006 result and can utilized in future global fits.
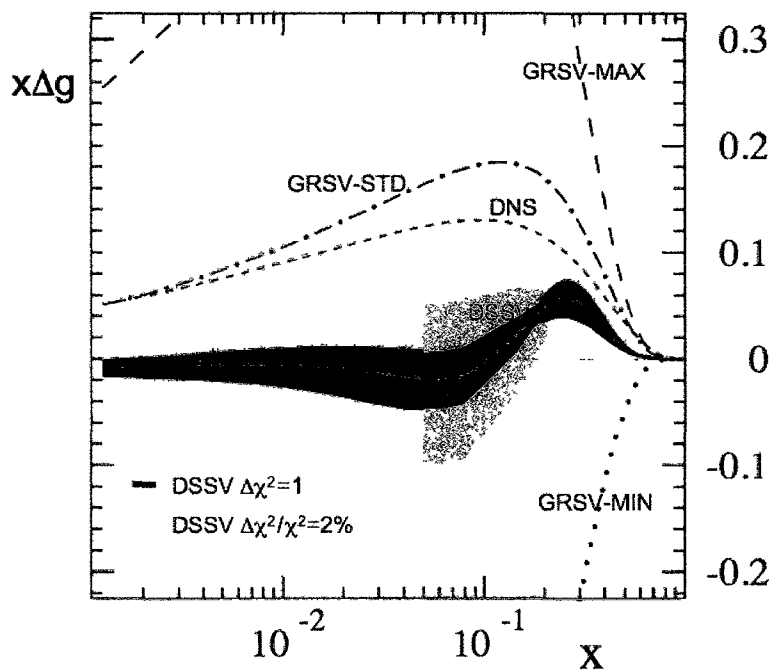
Figure 9.1: DSSV parameterization of $x\Delta g(x)$ vs. x evaluated at $Q^2 = 10$ GeV^2/c^2. Two estimates of their model uncertainty are presented in green and yellow. Additional models discussed throughout the text are shown for comparison. The approximate STAR kinematic x-range (0.05 → 0.2) is overlaid in the vertical shaded band.

No proposed physical model of proton structure has explained how gluon spins are significantly polarized[63]. Thus, it is not surprising that Δg, at least

the portion of the integral that is experimentally accessible, is small. If we now return to the angular momentum sum rule, we can see the larger picture of the proton's spin:

$$\frac{1}{2} = \int_0^1 dx\{\frac{1}{2}\Delta q(x, Q^2) + \Delta g(x, Q^2) + L_q(x, Q^2) + L_g(x, Q^2)\} \qquad (9.1)$$

Thanks to decades of DIS measurements, we now know g_1 much more precisely than the EMC collaboration's initial findings. The first moment of g_1, which to leading-order is just the quark (and anti-quark) spin contributions, is $33\pm3\%$[6][7] (see Eq. 1.8). The results of this dissertation, when combined with previously published STAR jet results and PHENIX π^o results, constrain Δg to be small within our x-range. Including what we know about the measured quark and gluon spin contributions with Eq. 9.1, we see that the majority of the proton spin must reside in some form of orbital angular momentum.

Unfortunately, there are no experiments currently devised to directly measure $L_{q,g}$ in Eq. 9.1. However, an indirect means of measuring the quark orbital angular momentum is possible through single-spin asymmetries with transversely polarized protons. We can learn about the transverse distribution of the proton and piece together the motion of quarks. This is a fairly new approach that is still a work in progress. Alternatively, Deeply Virtual Compton Scattering results ($\gamma^*p \rightarrow \gamma p$) can be related to the total quark angular momentum (spin + orbital) within the particular framework expressed by Ji[10]. Initial results using this method have been presented and give a model-dependent picture of the u and d quark total angular momentum contributions[64][65].

Further, Thomas and Myhrer[66] propose a resolution of the spin discrepancy with standard features of the non-perturbative nucleon structure. They construct

an alternative constituent model in which the proton is made up of valence quarks and a pion cloud. The model calculates a series of effects that reduce the fraction of spin carried by the valence quarks: the relativistic motion of the valence quarks, the one-gluon exchange interaction that accounts for hyperfine hadron mass splitting (N-Δ), and the pion mass cloud required by chiral symmetry. By including these three effects, they predict a reduced valence quark contribution of about $\sim 35\%$, which is very close to the experimental value. In their view there is not a significant spin crisis. Instead, these effects transfer quark spin to quark orbital angular momentum. Further exploration of the orbital angular momentum is clearly needed and is the next big piece in the proton spin puzzle. The upcoming 12 GeV upgrade at Jefferson National Lab will greatly improve experimentalists' ability to examine this contribution.

9.1 Comparison with Previous Cross Section Measurements

For completeness we include a comparison of our measured inclusive jet cross section to previous published results[13]. Figure 9.2 presents this comparison. Previous results agree with NLO theoretical calculations within systematic uncertainty limits, as do the results of this thesis. For the published results, hadronization and underlying event corrections were not applied but instead were included in the systematic uncertainties. This largely accounts for the difference between the two. Additionally, 2003 was the first year that the BEMC was commissioned and provided a much smaller data sample. The 2006 data set provides an 18-fold increase in integrated luminosity, as well as a factor of two increase in calorimeter coverage.
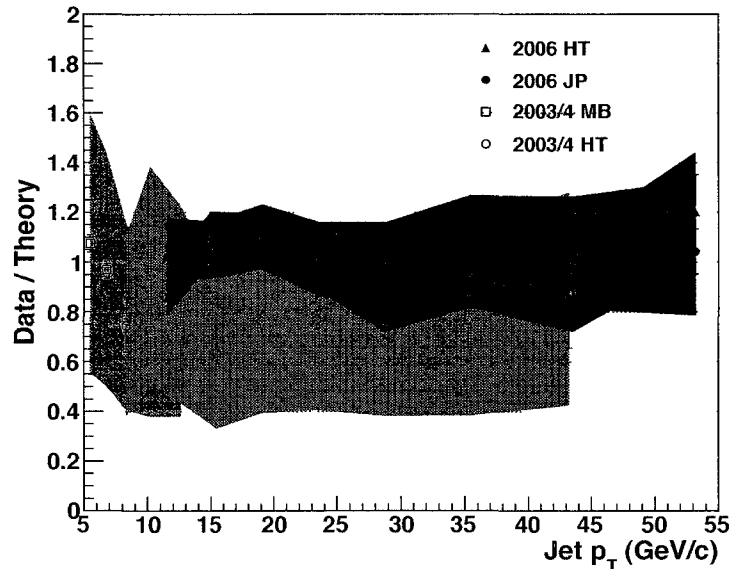
Figure 9.2: Inclusive jet cross section results from this thesis and from published results using 2003/04 RHIC data. Statistical uncertainties are shown as error bars and systematic uncertainties are shown as error bands: 2006 HT+JP(green), 2003/04 MB(red), and 2003/04 HT(blue).

9.2 Comparison with Additional A_{LL} Measurements

Figure 9.3 presents our measured A_{LL} results compared to previous jet results[60] and π^0 results from Phenix[61]. For the purpose of comparison, we assume that $p_T^{JET} \approx 2p_T^{\pi^0}$. This is motivated by STAR's π^0-jet correlation measurement that found neutral pions carry greater than half the transverse momentum of the associated jet[67]. We assume 50% here as a rough estimate. All three measurements agree well and provide consistent evidence of a relatively small measured A_{LL}.
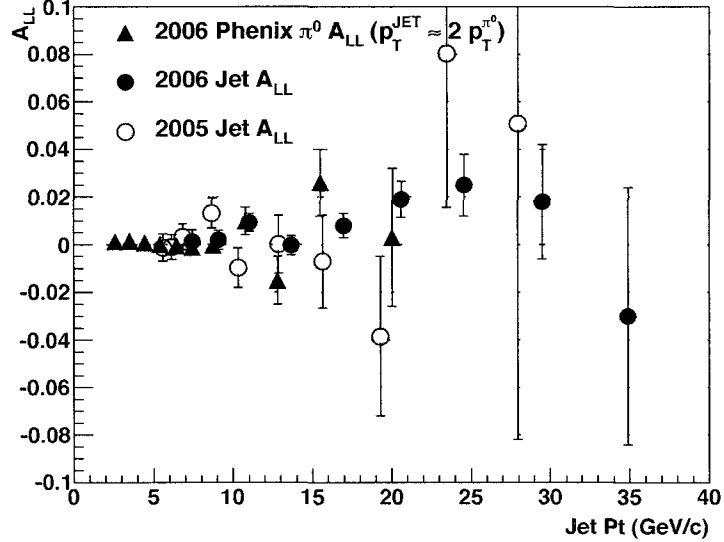
Figure 9.3: Inclusive jet A_{LL} results from this thesis (2006 RHIC data) and from 2005 RHIC data. Also included are inclusive π^0 A_{LL} results measured at the Phenix detector using 2006 RHIC data. π^0 results are plotted at approximate jet p_T, assuming the pion carries half the momentum of the jet.

9.3 Future Outlook

Additional polarized proton-proton data were collected during the 2008 and 2009 RHIC running periods. 2008 data, like the 2006 data, were taken at $\sqrt{s} = 200$ GeV center of mass energy. Unfortunately, the data suffers from low beam polarizations. Because the measured asymmetry ϵ relates to the analyzing power of the reaction A_{LL} via $\epsilon = P^2 A_{LL}$, a decrease in polarization P results in a quadratic decrease in figure of merit. During 2009, on the other hand, data were collected for the first time at $\sqrt{s} = 500$ GeV center of mass energy. For the same jet p_T bin, higher energy collisions probe a smaller x value. Therefore, 500 GeV inclusive jet data has the potential to further expand our x-window. Figure 9.4

shows projected sensitivity for data as a function of $x_T = 2p_T/\sqrt{s}$ for 200(red) and 500(blue) GeV inclusive jets. The luminosity and polarization estimates are admittedly optimistic, but the point is to show the approximate shift in accessible x_{gluon}. Theory curves are presented at both energies for comparison.
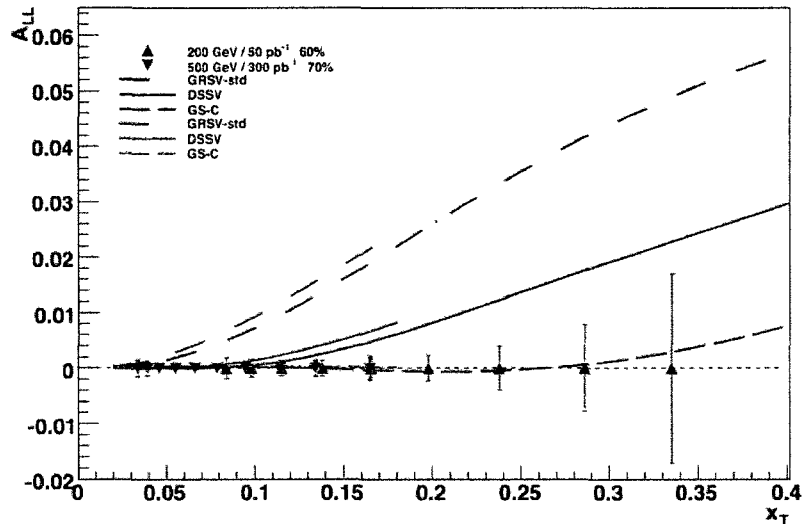
Figure 9.4: 200 and 500 GeV projections for the inclusive jet channel as a function of $x_T = 2p_T/\sqrt{s}$. GRSV-STD, GS-C, and DSSV theoretical predictions are also presented at the two energies for comparison.

Looking to the future, a polarized electron-nucleon collider is proposed[68]. An electron (or positron) beam of energy 5 to 10 GeV will collide with a nucleon beam of energy 25 to 250 GeV. Both beams will be polarized, and it is hoped that multiple collision energy scenarios are possible. With regard to the polarized nucleon spin structure, this facility has the capacity to vastly extend the kinematical reach of $g_1(x, Q^2)$ measurements. Projections show access to x-values as low as 3×10^{-4}, an unexplored phase space for polarization. With this extended reach, a global analyses of g_1 will yield a renewed precision for the polarized PDFs.

132

APPENDIX A

Acronyms

ADC   Analog to Digital Conversion

AGS   Alternating Gradient Synchrotron

BBC   Beam Beam Counter

BEMC   Barrel Electromagnetic Calorimeter

BNL   Brookhaven National Laboratory

C-AD   Collider-Accelerator Department

CNI   Coulomb Nuclear Interference

CTEQ   Coordinated Theoretical-Experimental Project on QCD

DAQ   Data Acquisition

DCA   Distance of Closest Approach

DIS   Deep Inelastic Scattering

DVCS   Deeply Virtual Compton Scattering

EEMC   Endcap Electromagnetic Calorimeter

EMC   European Muon Collaboration

GEANT   GEometry ANd Tracking

HT   High Tower

HTTP   High Tower + Trigger Patch

IR   Infrared

JP   Jet Patch

LO   Leading Order

MB   Minimum Bias

MC   Monte Carlo

MCA   Midpoint Cone Algorithm

MPI   Multiple Parton Interaction

NLO   Next to Leading Order

NNLO   Next to Next to Leading Order

OPPIS   Optically Pumped Polarized H^- Ion Source

PDF   Parton Distribution Function

PHENIX   Pioneering High Energy Nuclear Experiment

PMT   Photo Multiplier Tube

QCD   Quantum Chromodynamics

RHIC   Relativistic Heavy Ion Collider

SIDIS   Semi-Inclusive Deep Inelastic Scattering

STAR   Solenoidal Tracker at RHIC

TPC   Time Projection Chamber

ZDC   Zero Degree Calorimeter

APPENDIX B

The STAR Collaboration

M. M. Aggarwal[31], Z. Ahammed[48], A. V. Alakhverdyants[18], I. Alekseev [16],

B. D. Anderson[19], D. Arkhipkin[3], G. S. Averichev[18], J. Balewski[23], L. S. Barnby[2],

S. Baumgart[53], D. R. Beavis[3], R. Bellwied[51], M. J. Betancourt[23], R. R. Betts[8],

A. Bhasin[17], A. K. Bhati[31], H. Bichsel[50], J. Bielcik[10], J. Bielcikova[10], B. Biritz[6],

L. C. Bland[3], B. E. Bonner[37], J. Bouchet[19], E. Braidot[28], A. V. Brandin[26],

A. Bridgeman[1], E. Bruna[53], S. Bueltmann[30], I. Bunzarov[18], T. P. Burton[3],

X. Z. Cai[41], H. Caines[53], M. Calderón de la Barca Sánchez[5], O. Catu[53],

D. Cebra[5], R. Cendejas[6], M. C. Cervantes[43], Z. Chajecki[29], P. Chaloupka[10],

S. Chattopadhyay[48], H. F. Chen[39], J. H. Chen[41], J. Y. Chen[52], J. Cheng[45],

M. Cherney[9], A. Chikanian[53], K. E. Choi[35], W. Christie[3], P. Chung[10],

R. F. Clarke[43], M. J. M. Codrington[43], R. Corliss[23], J. G. Cramer[50],

H. J. Crawford[4], D. Das[5], S. Dash[13], A. Davila Leyva[44], L. C. De Silva[51],

R. R. Debbe[3], T. G. Dedovich[18], A. A. Derevschikov[33], R. Derradi de Souza[7],

L. Didenko[3], P. Djawotho[43], S. M. Dogra[17], X. Dong[22], J. L. Drachenberg[43],

J. E. Draper[5], J. C. Dunlop[3], M. R. Dutta Mazumdar[48], L. G. Efimov[18],

E. Elhalhuli[2], M. Elnimr[51], J. Engelage[4], G. Eppley[37], B. Erazmus[42],

M. Estienne[42], L. Eun[32], O. Evdokimov[8], P. Fachini[3], R. Fatemi[20], J. Fedorisin[18],

R. G. Fersch[20], P. Filip[18], E. Finch[53], V. Fine[3], Y. Fisyak[3], C. A. Gagliardi[43],

D. R. Gangadharan[6], M. S. Ganti[48], E. J. Garcia-Solis[8], A. Geromitsos[42],

F. Geurts[37], V. Ghazikhanian[6], P. Ghosh[48], Y. N. Gorbunov[9], A. Gordon[3],

O. Grebenyuk[22], D. Grosnick[47], S. M. Guertin[6], A. Gupta[17], N. Gupta[17],

W. Guryn[3], B. Haag[5], A. Hamed[43], L-X. Han[41], J. W. Harris[53],

J. P. Hays-Wehle[23], M. Heinz[53], S. Heppelmann[32], A. Hirsch[34], E. Hjort[22],

A. M. Hoffman[23], G. W. Hoffmann[44], D. J. Hofman[8], B. Huang[39], H. Z. Huang[6],

T. J. Humanic[29], L. Huo[43], G. Igo[6], P. Jacobs[22], W. W. Jacobs[15], C. Jena[13],

F. Jin[41], C. L. Jones[23], P. G. Jones[2], J. Joseph[19], E. G. Judd[4], S. Kabana[42],

K. Kajimoto[44], K. Kang[45], J. Kapitan[10], K. Kauder[8], D. Keane[19],

A. Kechechyan[18], D. Kettler[50], D. P. Kikola[22], J. Kiryluk[22], A. Kisiel[49],

S. R. Klein[22], A. G. Knospe[53], A. Kocoloski[23], D. D. Koetke[47], T. Kollegger[12],

J. Konzer[34], I. Koralt[30], L. Koroleva[16], W. Korsch[20], L. Kotchenda[26],

V. Kouchpil[10], P. Kravtsov[26], K. Krueger[1], M. Krus[10], L. Kumar[19], P. Kurnadi[6],

M. A. C. Lamont[3], J. M. Landgraf[3], S. LaPointe[51], J. Lauret[3], A. Lebedev[3],

R. Lednicky[18], C-H. Lee[35], J. H. Lee[3], W. Leight[23], M. J. LeVine[3], C. Li[39],

L. Li[44], N. Li[52], W. Li[41], X. Li[40], X. Li[34], Y. Li[45], Z. M. Li[52], G. Lin[53],

S. J. Lindenbaum[27], M. A. Lisa[29], F. Liu[52], H. Liu[5], J. Liu[37], T. Ljubicic[3],

W. J. Llope[37], R. S. Longacre[3], W. A. Love[3], Y. Lu[39], X. Luo[39], G. L. Ma[41],

Y. G. Ma[41], D. P. Mahapatra[13], R. Majka[53], O. I. Mall[5], L. K. Mangotra[17],

R. Manweiler[47], S. Margetis[19], C. Markert[44], H. Masui[22], H. S. Matis[22],

Yu. A. Matulenko[33], D. McDonald[37], T. S. McShane[9], A. Meschanin[33],

R. Milner[23], N. G. Minaev[33], S. Mioduszewski[43], A. Mischke[28], M. K. Mitrovski[12],

B. Mohanty[48], M. M. Mondal[48], B. Morozov[16], D. A. Morozov[33], M. G. Munhoz[7],

B. K. Nandi[14], C. Nattrass[53], T. K. Nayak[48], J. M. Nelson[2], P. K. Netrakanti[34],

M. J. Ng[4], L. V. Nogach[33], S. B. Nurushev[33], G. Odyniec[22], A. Ogawa[3],

V. Okorokov[26], E. W. Oldag[44], D. Olson[22], M. Pachr[10], B. S. Page[15], S. K. Pal[48],

Y. Pandit[19], Y. Panebratsev[18], T. Pawlak[49], T. Peitzmann[28], V. Perevoztchikov[3],

C. Perkins[4], W. Peryt[49], S. C. Phatak[13], P. Pile[3], M. Planinic[54],

M. A. Ploskon[22], J. Pluta[49], D. Plyku[30], N. Poljak[54], A. M. Poskanzer[22],

136

B V K S Potukuchi[17], C B Powell[22], D Pindle[50], C Pruneau[51],

N K Pruthi[31], P R Pujahari[14], J Putschke[53], R Raniwala[36], S Raniwala[36],

R L Ray[44], R Redwine[23], R Reed[5], H G Ritter[22], J B Roberts[37],

O V Rogachevskiy[18], J L Romero[5], A Rose[22], C Roy[42], L Ruan[3], R Sahoo[42],

S Sakai[6], I Sakrejda[22], T Sakuma[23], S Salur[5], J Sandweiss[53], E Sangaline[5],

J Schambach[44], R P Scharenberg[34], N Schmitz[24], T R Schuster[12], J Seele[23],

J Seger[9], I Selyuzhenkov[15], P Seyboth[24], E Shahaliev[18], M Shao[39],

M Sharma[51], S S Shi[52], E P Sichtermann[22], F Simon[23], R N Singaraju[48],

M J Skoby[34], N Smirnov[53], P Sorensen[3], J Sowinski[15], H M Spinka[1],

B Srivastava[34], T D S Stanislaus[47], D Staszak[6], J R Stevens[15], R Stock[12],

M Strikhanov[26], B Stringfellow[34] A A P Suaide[7], M C Suarez[8],

N L Subba[19], M Sumbera[10], X M Sun[22], Y Sun[39], Z Sun[21], B Surrow[23],

D N Svirida[16], T J M Symons[22], A Szanto de Toledo[7], J Takahashi[7],

A H Tang[3], Z Tang[39], L H Tarini[51], T Tarnowsky[25], D Thein[44],

J H Thomas[22], J Tian[41], A R Timmins[51], S Timoshenko[26], D Tlusty[10],

M Tokarev[18], T A Trainor[50], V N Tram[22], S Trentalange[6], R E Tribble[43],

O D Tsai[6], J Ulery[34], T Ullrich[3], D G Underwood[1], G Van Buren[3],

M van Leeuwen[28], G van Nieuwenhuizen[23], J A Vanfossen, Jr [19], R Varma[14],

G M S Vasconcelos[7], A N Vasiliev[33], F Videbaek[3], Y P Viyogi[48], S Vokal[18],

S A Voloshin[51], M Wada[44], M Walker[23], F Wang[34], G Wang[6], H Wang[25],

J S Wang[21], Q Wang[34], X L Wang[39], Y Wang[45] G Webb[20], J C Webb[3],

G D Westfall[25], C Whitten Jr [6], H Wieman[22], S W Wissink[15], R Witt[46],

Y F Wu[52], W Xie[34], N Xu[22], Q H Xu[40], W Xu[6], Y Xu[39], Z Xu[3],

L Xue[41], Y Yang[21], P Yepes[37], K Yip[3], I-K Yoo[35], Q Yue[45], M Zawisza[49],

H Zbroszczyk[49], W Zhan[21], J B Zhang[52], S Zhang[41], W M Zhang[19],

X P Zhang[22], Y Zhang[22], Z P Zhang[39], J Zhao[41], C Zhong[41] J Zhou[37],

W Zhou[40], X Zhu[45], Y H Zhu[41], R Zoulkarneev[18], Y Zoulkarneeva[18]

(STAR Collaboration)

[1] *Argonne National Laboratory, Argonne, Illinois 60439, USA*

[2] *University of Birmingham Birmingham, United Kingdom*

[3] *Brookhaven National Laboratory. Upton. New York 11973, USA*

[4] *University of California, Berkeley. California 94720, USA*

[5] *University of California. Davis, California 95616, USA*

[6] *University of California, Los Angeles, California 90095, USA*

[7] *Universidade de Campinas, Sao Paulo, Brazil*

[8] *University of Illinois at Chicago, Chicago, Illinois 60607, USA*

[9] *Creighton University, Omaha, Nebraska 68178, USA*

[10] *Czech Technical University in Prague. FNSPE. Prague, 115 19, Czech Republic*

[11] *Nuclear Physics Institute AS CR, 250 68 Řež/Prague, Czech Republic*

[12] *University of Frankfurt, Frankfurt, Germany*

[13] *Institute of Physics, Bhubaneswar 751005. India*

[14] *Indian Institute of Technology, Mumbai, India*

[15] *Indiana University, Bloomington. Indiana 47408, USA*

[16] *Alikhanov Institute for Theoretical and Experimental Physics, Moscow. Russia*

[17] *University of Jammu. Jammu 180001, India*

[18] *Joint Institute for Nuclear Research, Dubna, 141 980, Russia*

[19] *Kent State University. Kent. Ohio 44242 USA*

[20] *University of Kentucky, Lexington. Kentucky, 40506-0055, USA*

[21] *Institute of Modern Physics. Lanzhou, China*

[22] *Lawrence Berkeley National Laboratory. Berkeley, California 94720. USA*

[23] *Massachusetts Institute of Technology. Cambridge, MA 02139-4307. USA*

[24] *Max-Planck-Institut fur Physik. Munich, Germany*

[25] *Michigan State University, East Lansing, Michigan 48824. USA*

[26] *Moscow Engineering Physics Institute, Moscow Russia*

138

[27] *City College of New York, New York City, New York 10031, USA*

[28] *NIKHEF and Utrecht University, Amsterdam, The Netherlands*

[29] *Ohio State University. Columbus, Ohio 43210. USA*

[30] *Old Dominion University, Norfolk, VA. 23529, USA*

[31] *Panjab University, Chandigarh 160014, India*

[32] *Pennsylvania State University. University Park, Pennsylvania 16802 USA*

[33] *Institute of High Energy Physics Protvino Russia*

[34] *Purdue University, West Lafayette, Indiana 47907. USA*

[35] *Pusan National University. Pusan. Republic of Korea*

[36] *University of Rajasthan, Jaipur 302004. India*

[37] *Rice University, Houston Texas 77251, USA*

[38] *Universidade de Sao Paulo Sao Paulo, Brazil*

[39] *University of Science & Technology of China, Hefei 230026, China*

[40] *Shandong University, Jinan, Shandong 250100, China*

[41] *Shanghai Institute of Applied Physics, Shanghai 201800, China*

[42] *SUBATECH, Nantes. France*

[43] *Texas A&M University, College Station, Texas 77843, USA*

[44] *University of Texas, Austin. Texas 78712. USA*

[45] *Tsinghua University. Beijing 100084, China*

[46] *United States Naval Academy, Annapolis MD 21402, USA*

[47] *Valparaiso University Valparaiso, Indiana 46383, USA*

[48] *Variable Energy Cyclotron Centre, Kolkata 700064, India*

[49] *Warsaw University of Technology, Warsaw Poland*

[50] *University of Washington, Seattle. Washington 98195, USA*

[51] *Wayne State University Detroit, Michigan 48201, USA*

[52] *Institute of Particle Physics. CCNU (HZNU), Wuhan 430079. China*

[53] *Yale University, New Haven Connecticut 06520, USA*

[54] *University of Zagreb, Zagreb, HR-10002, Croatia*

REFERENCES

[1] C. Amsler et al. Review of Particle Physics. *Phys. Lett.* B667:1, 2008 and 2009 partial update for the 2010 edition.

[2] G. Altarelli, et al. Asymptotic Freedom in Parton Language. *Nucl. Phys.* B126: 298, 1977.

[3] J. Ashman, et al. A Measurement of the Spin Asymmetry and Determination of the Structure Function g(1) in Deep Inelastic Muon-Proton Scattering. *Phys. Lett.* B206:364, 1988.

[4] E. Leader and M. Anselmino. A Crisis in the Parton Model: Where, Oh Where is the Proton's Spin? *Z. Phys.* C41:239. 1988.

[5] S.E. Kuhn, et al. Spin Structure of the Nucleon - Status and Recent Results. *Prog. Part. Nucl. Phys.* 63:1, 2009.

[6] A. Airapetian, et al. Precise Determination of the spin structure function g(1) of the proton, deuteron and neutron. *Phys. Rev.* D75:012007, 2007.

[7] V. Yu, et al. The Deuteron Spin-dependent Structure Function g1(d) and its First Moment. *Phys. Lett.* B647:8, 2007.

[8] M. Hirai, et al. Determination of the polarized parton distribution functions and their uncertainties. *Phys. Rev.* D69:054012. 2004.

[9] S.V. Bashinsky and R.L. Jaffe. Quark and Gluon Orbital Angular Momentum and Spin in Hard Processes. *Nucl. Phys.* B536:303, 1998.

[10] X. Ji. Gauge Invariant decomposition of nucleon spin and its spin - off. *Phys. Rev. Lett.* 78:610, 1997.

[11] G. Bunce, et al. Prospects for Spin Physics at RHIC. *Ann. Rev. Nucl. Part. Sci.* 50:525, 2000.

[12] B Jäger, et al. Single-inclusive jet production in polarized pp collisions at $O(\alpha_s^3)$. *Phys. Rev.* D70:034010, 2004.

[13] B.I. Abelev et al. Longitudinal double-spin asymmetry and cross section for inclusive jet production in polarized proton collisions at $\sqrt{s} = 200$ *GeV*. *Phys. Rev. Lett.* 97:252001, 2006.

[14] S.J. Brodsky, et al. Perturbative QCD constraints on the shape of polarized quark and gluon distributions. *Nucl. Phys.* B441:197, 1995.

[15] E. Leader, et al. Impact of CLAS and COMPASS data on Polarized Parton Densities and Higher Twist. *Phys. Rev.* D75:074027, 2007.

[16] M. Gluck, et al. Models for the Polarized Parton Distributions of the Nucleon. *Phys. Rev.* D63:094005, 2001.

[17] T. Gehrmann and W.J. Stirling. Polarized Parton Distributions in the Nucleon. *Phys. Rev.* D53:6100, 1996.

[18] D. de Florian, et al. Sea quarks and gluon polarization in the nucleon at NLO accuracy. *Phys. Rev.* D71:094018, 2005.

[19] J. Blümlein, et al. QCD Analysis of Polarized Deep Inelastic Scattering Data and Parton Distributions. *Nucl. Phys.* B636:225, 2002.

[20] D. de Florian, et al. Global Analysis of Helicity Parton Densities and their Uncertainties. *Phys. Rev. Lett.* 101:072001, 2008.

[21] M. Hirai, et al. Determination of polarized parton distribution functions with recent data on polarization asymmetries. *Phys. Rev.* D74:014015, 2006.

[22] I. Alekseev, et al. Polarized proton collider at RHIC. *Nucl. Instrum. & Meth.* A499:392, 2003.

[23] S. R. Mane, Yu M. Shatunov, and K. Yokoya. Siberian snakes in high-energy accelerators. *J. Phys.* G31:R151-R209, 2005.

[24] H. Huang, et al. A p-Carbon CNI polarimeter for RHIC. *Contributed to IEEE Particle Accelerator Conference (PAC 99), New York, 2009.*

[25] H. Huang, et al. Commissioning of RHIC p carbon CNI polarimeter. *Nucl. Phys.* A721:356, 2003.

[26] O. Jinnouchi et al. Measurement of the analyzing power of proton-carbon elastic scattering in the CNI region at RHIC. *arxiv:nucl-ex/0412053.*

[27] H. Okada, et al. Measurement of the analyzing power A_N in pp elastic scattering in the CNI region with a polarized atomic hydrogen gas jet target. *Phys. Lett.* B638:450, 2006.

[28] I.G. Alekseev, et al. Measurements of single and double spin asymmetry in pp elastic scattering in the CNI region with a polarized atomic hydrogen gas jet target. *Phys. Rev.* D79:094014, 2009.

[29] CNI Polarimeter Group Homepage. *http://www4.rcf.bnl.gov/~cnipol.*

142

[30] W.R Lozowski and J.D. Hudson. Inproved carbon micro-ribbon targets and stripper foils for the IUCF cooler ring. *Nucl. Instrum. & Meth.* A334:173, 1993.

[31] L.C. Bland. STAR Results from Polarized Proton Collisions at RHIC. *arxiv:hep-ex/0403012*, 2004.

[32] J. Adams et al. Transverse-Momentum and Collision-Energy Dependence of High-p_T Hadron Suppression in Au+Au Collisions at Ultrarelativistic Energies. *Phys. Rev. Lett.* 91:172302, 2003.

[33] J. Kiryluk. Local polarimetry for proton beams with the STAR beam beam counters. *arxiv:hep-ex/0501072*, 2005.

[34] C.A. Whitten. The beam-beam counter: A local polarimeter at STAR. *AIP Conf. Proc.* 980:390, 2008.

[35] H. Crawford, et al. The STAR Scaler Board, A 10 MHz 24-bit VME Memory Module. *To be published.*

[36] M. Anderson, et al. The STAR Time Projection Chamber: A Unique Tool for Studying High Multiplicity Events at RHIC. *Nucl. Instrum. & Meth.* A499:659, 2003.

[37] M. Beddo, et al. The STAR Barrel Electromagnetic Calorimeter. *Nucl. Instrum. & Meth.* A499:725, 2003.

[38] C.E. Allgower, et al. The STAR endcap electromagnetic calorimeter. *Nucl. Instrum. & Meth.* A499:740, 2003.

[39] M. Betancourt, et al. 2006 BEMC Tower Calibration Report. *Internal STAR document. http://www.star.bnl.gov/HyperNews-star/get/emc2/3279.html*

[40] T. M. Cormier, et al. STAR Barrel Electromagnetic Calorimeter Absolute Calibration Using "Minimum Ionizing Particles" from Collisions at RHIC. *STAR Note 436*, 2001.

[41] F.S. Biesɛr, et al. The STAR trigger. *Nucl. Instrum. & Meth.* A499:766, 2003.

[42] J.M. Landgraf, et al. An Overview of the STAR DAQ system. *Nucl. Instrum. & Meth.* A499:762, 2003.

[43] G.C. Blazey, et al. Run II Jet Physics. *arxiv:hep-ex/0005012*, 2000.

[44] G.P. Salam and G. Soyez. A practical Seedless Infrared-Safe cone jet algorithm. *Journal of High Energy Physics* 0705:086, 2007.

[45] T. Stostrand et al. High-energy-physics event generation with PYTHIA 6.1. *Comput. Phys. Common.* 135:238, 2001.

[46] GEANT 3.21, CERN program library.

[47] http://durpdg.dur.ac.uk/hepdata/pdf.html

[48] Michael Miller. Measurement of Jets and Jet Quenching at RHIC. *PhD thesis*, Yale University, 2004.

[49] J. Pumplin, et al. New generation of parton distributions with uncertainties from global QCD analysis. *J. High Energy Phys.* 0207:012, 2002.

[50] F. Aversa, et al. Jet Inclusive Production to $\mathcal{O}_\alpha^3$: Comparison with Data. *Phys. Rev. Lett.* 65:410, 1990.

[51] D. Cronin-Hennessy, et al. Luminosity monitoring and measurement at CDF. *Nucl. Instrum. & Meth.* A443:37, 2000.

[52] T. Aaltonen, et al. Measurement of the Inclusive Jet Cross Section at the Fermilab Tevatron p anti-p Collider Using a Cone-Based Jet Algorithm. *Phys. Rev.* D78:052006, 2008.

[53] D. Acosta, et al. Study of jet shapes in inclusive jet production in ppbar collisions at $\sqrt{s} = 1.96\,TeV$. *Phys. Rev.* D71, 112002, 2005.

[54] Lafferty, G. D. and Wyatt, T. R. Where to stick your data points: The treatment of measurements within wide bins. *Nucl. Instrum. & Meth.* A355:541, 1995.

[55] J. Adams, et al. Measurements of transverse energy distributions in Au+Au collisions at $\sqrt{s_{NN}} = 200$ GeV. *Phys. Rev.* C70:054907, 2004.

[56] F. Rathmann, et al. Complete angular distribution measurements of pp spin correlation parameters A_{xx}, A_{yy}, and A_{xz} and analyzing power A_y at 197.4 MeV. *Phys. Rev.* C58:658, 1998.

[57] J. Balewski, for the STAR Collaboration. Midrapidity Spin Asymmetries at STAR. *AIP Conf. Proc.* 675:418, 2003.

[58] J. Kiryluk, for the STAR collaboration. Relative luminosity measurement in STAR and implications for spin asymmetry determinations. *AIP conf. Proc.* 675:424, 2003.

[59] D Staszak, for the Collaboration Inclusive Jet A_{LL} Measurements at STAR *Lake Louise Winter Institute Proc*, 2008 (Preprint hep-ex 0805 3004) M Sarsour, for the Collaboration *APS DNP meeting, Newport News, Virginia* October, 2007

[60] B I Abelev, et al Longitudinal Double-Spin Asymmetry for Inclusive Jet Production in $p + p$ Collisions at $\sqrt{s} = 200$ *GeV Phys Rev Lett* 100 232003, 2008

[61] A Adare, et al Gluon-Spin Contribution to the Proton Spin from the Double-Helicity Asymmetry in Inclusive π^0 Production in Polarized $p + p$ Collisions at $\sqrt{s} = 200$ *GeV Phys Rev Lett* 103 012003, 2009

[62] A Adare, et al Inclusive cross section and double helicity asymmetry for π^o production in $p + p$ collisions at $\sqrt{s} = 200$ GeV Implications for the polarized gluon distribution in the proton *Phys Rev* D76 051106, 2007

[63] A W Thomas The Spin of the Proton *Prog Part Nucl Phys* 61 219, 2008

[64] M Mazouz, et al Deeply Virtual Compton Scattering off the Neutron *Phys Rev Lett* 99 242501, 2007

[65] F Ellinghaus, et al Can the total angular momentum of u-quarks in the nucleon be accessed at HERMES? *Eur Phys J* C46 729, 2006

[66] F Myhrei and A W Thomas Resolution of the Proton Spin Problem *Phys Lett* B663 302, 2008

[67] B I Abelev, et al Longitudinal double-spin asymmetry and cross section for inclusive neutral pion production at midrapidity in polarized proton collisions at $\sqrt{s} = 200$ *GeV Phys Rev* D80 111108, 2009

[68] A Deshpande, et al Study of the fundamental structure of matter with an electron-ion collider *Ann Rev Nucl Part Sci* 55 165, 2005